# High-power and high-aspect-ratio optical coatings by atomic layer deposition

**A DISSERTATION**
**SUBMITTED TO THE FACULTY OF THE GRADUATE SCHOOL**
**OF THE UNIVERSITY OF MINNESOTA**
**BY**

**Nicholas Theodore Gabriel**

**IN PARTIAL FULFILLMENT OF THE REQUIREMENTS**
**FOR THE DEGREE OF**
**Doctor Of Philosophy**

**February, 2011**

# Acknowledgements

Chris Lyons of 3M truly embodies the word "mentor" and I am grateful to him for volunteering his time.

My fellow graduate students have been there for countless discussions, some for over five years, always ready with helpful suggestions. In particular, Anand Gawarikar, BJ Potter, Brad Tiffany, Jan Makowski, Kyle Olson, Luke Taylor, Martin Soh, Merlin Mah, Michael Sutton, Phil Armstrong, Ryan Shea, Sangho S. Kim, Wing Shan Chan, Woo Bin Song, and Yuyan Wang are all gratefully acknowledged.

Ronald Belt with Honeywell International offered much encouragement and helpful career advice along the way.

Parts of this work were carried out in the UMN Nanofabrication Center (NFC) which receives partial support from NSF through the NNIN program. The NFC process staff and maintenance team have been instrumental in enabling the coating deposition and fabrication presented in this work. Particularly enduring help from Mark Fisher, Kevin Roberts, Tony Whipple, and Gary Olin is specially acknowledged.

Parts of this work were also carried out in the UMN Characterization Facility, which receives partial support from NSF through the MRSEC program. Scanning probe microscopy measurements were performed by Greg Haugstad, and Maria Torija provided helpful assistance with x-ray measurements.

Radek Uberna of Lockheed Martin supplied the capillary tube samples presented in the section on atomic layer deposition in channels.

Funding support is acknowledged from several sources: the 3M Graduate Fellowship Program; the Joint Technology Office (JTO) and the United States Air Force Office of Scientific Research (USAFOSR) for funding support under Multidisciplinary University Research Initiative (MURI); the Office of Naval Research (ONR); the JTO and Anasys

Instruments.

Thank you to my committee members for volunteering their time to serve on my committee and to review this dissertation.

My research adviser Joey Talghader has a unique ability see new opportunities, a key to my success in graduate school. I thank him for his guidance and for sharing his knowledge and insight with me.

# Dedication

To Jim and Pam Gabriel for nurturing their young scientist and creating so many opportunities for me. And to Kate for taking over the job.

ABSTRACT

In high-power applications, optical coatings must meet rigorous thermomechanical and damage threshold standards in addition to performing the desired optical function, which includes filters, beam splitters, anti-reflection coatings, and high-reflectivity mirrors. We investigate several aspects of high-power coatings and the particular suitability of atomic layer deposition (ALD) to meet many of the design goals. After reviewing the origin of thermal expansion in solids, techniques for its measurement in thin films, and the unique characteristics of ALD, we look at the ability to predict a coating's thermal deformation. Coatings using ALD alumina and hafnia are demonstrated to have very consistent refractive indices, growth rates, thermal expansion coefficients, and biaxial moduli, which together enable *a priori* design of "thermally invariant" mirrors that maintain high reflectivity without changing shape with temperature.

We have also characterized the undesired crystallization of ALD hafnia that can lead to roughness at thicknesses relevant to optical coatings. A nanolaminate strategy is explored, where ultrathin layers of alumina—less than 1 nanometer thick—are inserted periodically to disrupt the growth of hafnia crystallites. The hafnia-rich nanolaminates, near 100 nanometers in total thickness, are found to be amorphous and smooth down to very low concentrations of alumina and have a predictable decrease in refractive index with increasing alumina concentration. The thermal conductivity of ALD alumina and hafnia along with a series of nanolaminates is characterized in detail, focusing on the effect of interfaces in the nanolaminate films. The room-temperature thermal conductivity of the partially-crystalline pure hafnia film is 1.7 W/(m K), whereas all nanolaminates fall in the range of 1 to 1.2 W/(m K). Cryogenic measurements to 30 K show that this 30–40% reduction is likely due to the amorphous nature of the nanolaminates rather than the effect of interface resistance, and the thermal conductivity closely follows that expected for fully-disordered hafnia.

A unique feature of ALD is its ability to conformally coat very high-aspect-ratio structures, like nanoscale holes and trenches. We investigate this at the mixed length scale of many common optical systems, with at least one dimension on the order of centimeters, another as low as several micrometers, and with nanoscale thickness precision. An example is coating the inside of a hollow glass capillary waveguide. We find that

ALD alumina considerably outperforms hafnia under such conditions and quantify the difference using a large-area wedge structure with cross-section varying from about 20 micrometers to over a millimeter. The alumina process hardly notices the constrained geometry, whereas hafnia shows variation in thickness and refractive index consistent with non-ideal ALD growth mechanisms. Both coatings remain quite repeatable, with the resonance of a Fabry-Perot filter behaving as predicted except at the deepest regions of the wedge.

# Contents

# List of Tables

# List of Figures

# Chapter 1

# Introduction

This dissertation crosses a variety of disciplines and all them have an impressive history, so effort is made in the first few chapters to review previous work in the relevant areas before presenting the novel work that was performed. The starting point is a review of the physics of thermal expansion to build a foundation for the subsequent review of thin film deformation, which results from mismatch in thermal expansion behavior. These concepts play an important role in the experimental work on the thermal bending of multilayer mirrors. Thermal expansion theory also includes the concepts of a Debye temperature and a Debye approximation for the density of phonon states, which come up again in the analysis of thermal conductivity results.

Atomic layer deposition (ALD) is the core coating technology applied throughout, so it is the final review chapter before diving into the experimental work. Optical coatings have not been the main focus of the bulk of the ALD literature to date, so examples in optics are highlighted.

The new experimental and analytical work is separated into three unique chapters, connected by their applicability to optical systems and their particular need for the unique properties of ALD. The control of thermal deformation in multilayer mirrors requires a multitude of coating properties to be consistent over time. Depositing nanometer-scale films *inside* relatively large high-aspect ratio structures needs a process that is neither limited by line-of-sight nor particularly sensitive to vapor flux. And, in the final chapter, forming nanolaminates where one of the repeating layers is less than one nanometer thick is a job that ALD was meant to do. A brief list of all of these

chapters follows.

- Chapter 2 is a fairly detailed look at the physical origin of thermal expansion in solids.
- Chapter 3 reviews techniques for the measurement of thin film thermal expansion.
- In Chapter 4, atomic layer deposition is described in general, highlighting growth characteristics and limitations, along with the specific alumina and hafnia processes relevant to this thesis and some optical applications.
- Chapter 5 covers new work on controlling thermal deformation in thin optics, relying on the extreme precision and repeatability of atomic layer deposition.
- Chapter 6 is experimental work on atomic layer deposition inside channels on a length scale relevant for optical coatings.
- Chapter 7 contains work on crystallinity, surface roughness, refractive index, and thermal conductivity of hafnia-based nanolaminate films.
- Acronyms are defined inline as they are used but some important acronyms are also defined in Appendix A for convenience.
- Information about the thermomechanical and optical models employed are in Appendices B and C.
- Details on the differential $3\omega$ technique for measuring thermal conductivity including uncertainty analysis are in Appendix D.

# Chapter 2

# Thermal Expansion in Solids

## 2.1 Overview

In this chapter we study the underlying mechanisms of thermal expansion in solids, limiting the discussion to crystals to take advantage of periodicity and symmetry where useful.

Thermal expansion is an anharmonic effect, requiring at least 3rd-order displacement terms in expressions of potential energy in addition to dominant 2nd-order harmonic terms. A background on the harmonic approximation is given as it pertains to phonons and why it does not yield any predicted thermal expansion.

Grüneisen parameters play a central role in theoretical considerations of thermal expansion, allowing it to be conveniently expressed in proportion to heat capacity. This relationship has been shown to be approximately constant for many materials at low and high temperatures, yielding a relatively compact model of thermal expansion. In other cases there is significant temperature dependence of the Grüneisen parameter. The origin and utility of these parameters, their temperature dependence, and behavior in high- and low-temperature limits are central topics of the chapter.

The Debye model and associated Debye temperature are also discussed. This temperature varies widely by material and has important consequences for thermal expansion behavior. Above the Debye temperature the situation tends to be simpler as helpful approximations can be made and justified. But below the Debye temperature, additional mechanisms must be considered as they can lead to considerable variation in

the Grüneisen parameters (and thus thermal expansion behavior).

Discussion of techniques for measurement of thermal expansion of bulk solids and actual measured data are in general outside the scope of this chapter. However, techniques for modeling and measuring thin film thermal expansion are reviewed in Ch. 3. It is also noted that advances in measurement capability during the 20th century and the corresponding data led to observations that demanded additional theoretical explanations, so it was an important driving force behind the developments presented below and the two are often presented in tandem in the literature.

## 2.2 Lattice vibrations

Thermal expansion finds its way into a myriad of problems in engineering and physics, from the design of a bridge with "expansion joints" to withstand seasonal temperature change, to detailed studies of lattice parameters for use in semiconductor applications [2]. Despite its significance, it may be somewhat surprising that the very commonly applied harmonic approximation of lattice vibrations would predict exactly zero thermal expansion. This apparent failure of the harmonic model is quite sensible under further scrutiny, so we begin with a brief review of its assumptions before moving on to discussion of the anharmonic behavior that leads to thermal expansion.

### 2.2.1 Harmonic approximation

Details of harmonic behavior in crystals are found in any discussion of solid state physics, e.g. textbooks by Ashcroft and Mermin [3] or Kittel [4]. In this section we primarily follow the development of Ashcroft and Mermin but in one-dimension to retain an intuitive picture of the behavior.

Modeling a static lattice is a useful framework, especially for the development of equilibrium electronic properties, but it has many shortcomings in predicting basic properties. Ashcroft and Mermin devote their brief Chapter 21 to these shortcomings. Noteworthy among them are heat and sound conduction in insulators, the non-electronic contribution to heat capacity, temperature dependent electrical conductivity, Raman scattering of light, and the existence of thermal expansion. Here we are of course interested in the final concept, and since its existence relies on lattice vibrations we

must first describe those vibrations.

The harmonic approximation starts from an assumption that the displacement of ions from their mean location is small, but this assumption is also shared with the anharmonic analysis to be discussed later. It is really a question of "how small?" and the distinction is a subtle one with significant implications. In general, assuming small displacements is useful because it is valid enough for almost all practical situations in solids and basically makes the analysis possible. To define the harmonic approximation more specifically we consider the potential in the lattice. An isolated two-particle system separated by distance $x$ has potential usually represented by

$$\phi(x) = -\frac{A}{x^6} + \frac{B}{x^{1\,2}}, \tag{2.1}$$

where $A$ and $B$ are positive constants. The power 12 is somewhat arbitrary, a convention chosen to represent the strongly repulsive potential at very short distances where nuclear repulsion and Pauli exclusion dominate. It simply must be a power larger than 6 such that it overpowers the attractive potential in that region. This attractive-repulsive interaction yields a value of $x$ at which the potential has a minimum, and this is the equilibrium bond length for the two particles. A sketch of this potential is shown in Fig. 2.1.

Eq. 2.1 only represents two atoms but we are interested in an entire crystal. For a static, monatomic linear chain with set of lattice positions $\{R\} = \{0, \pm a, \pm 2a, \ldots\}$, the total static potential $U_{\text{st}}$ is a sum of each interaction between each atom and all the others, which we signify as atoms at $R$ and $R'$:

$$U_{\text{st}} = \sum_{R,R'} \phi(R - R'). \tag{2.2}$$

Of course it is quite likely that for a given atom at $R$, the value of $\phi$ is only of appreciable magnitude for $R'$ nearby and this expression for static potential can be simplified considerably. Also, the potential $\phi$ need not be the Lennard-Jones relation in Eq. (2.1) for relation Eq. (2.2) to hold; that was mentioned simply to give a convenient picture of the form of each interaction.

The atoms are vibrating, so their position $R$ or $R'$ really only represents an average location and $U_{\text{st}}$ only partially describes the system potential. We must introduce a

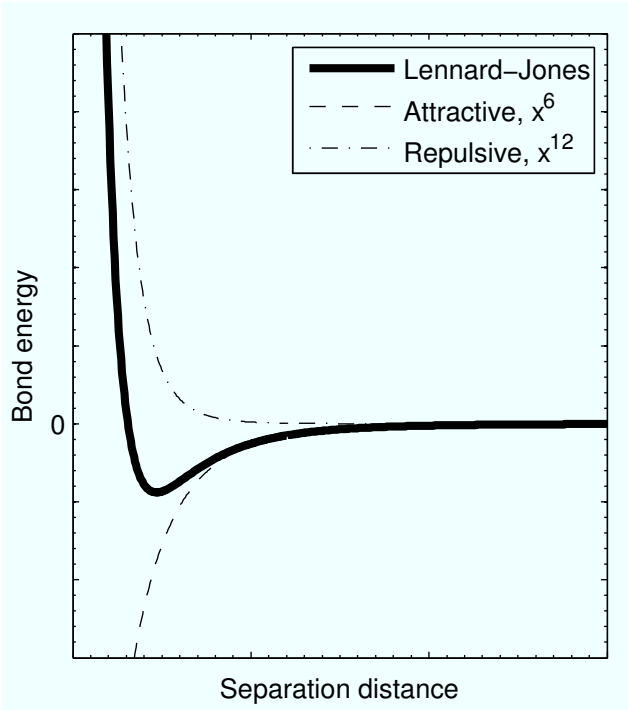


Figure 2.1: A example sketch of the Lennard-Jones potential for a two-particle system as defined in Eq. 2.1.

displacement term for each atom $u(R)$ relative to its mean position, and Eq. (2.2) becomes

$$U = \sum_{R,\,R'} \phi(R - R' + u(R) - u(R')). \tag{2.3}$$

This tells us that each individual two-atom interaction contributes to the overall potential based on their instantaneous distance from one another, $x = R - R' + u(R) - u(R')$, which is a combination of their average fixed distance from each other, $R - R'$, and the difference in displacement from equilibrium, $u(R) - u(R')$.

At this point we apply the assumption that the displacements are small in a Taylor series expansion of each $\phi(x)$ term in Eq. (2.3) about $x = R - R'$, yielding

$$U = U_{\text{st}} + 0 + U_{\text{harm}} + O(u^3), \tag{2.4}$$

where $U_{\text{st}}$ is as given in Eq. (2.2), the linear term is zero because $\partial\phi/\partial x = 0$ at a minimum point (i.e. any $x = R - R'$), and $U_{\text{harm}}$ is the harmonic (quadratic in

displacement) contribution to the potential given by

$$U_{\text{harm}} = \frac{1}{2} \sum_{R,\, R'} \frac{\partial^2}{\partial\, x^2}\, \phi(R - R') \left(u(R) - u(R')\right)^2 . \tag{2.5}$$

This equation may be further simplified and often is by choosing only those pairs of atoms $R, R'$ that are close to one another, e.g. nearest neighbors only.

The potential $U$ as defined in Eq. (2.4) is a basic statement of the harmonic approximation: we keep only the static term and the first non-zero term, which is second-order in displacement. Doing so means the restoring force on displaced atoms, $F = -\partial U/\partial x$, is the negative curvature of the Lennard-Jones potential at its minimum (the "spring constant") times the relative displacement. In 1D, one can rather easily imagine a parabola representing the potential associated with this sort of displacement for a given atom, where the force is proportional to displacement and always back towards its mean position $x = R$. This is a statement of Hooke's law, $F = -C\, u_{R,R'}$ where $C$ is the spring constant, yielding lattice vibrations that can be described entirely by their wavevector $k$ and frequency $\omega_b(k)$.

As mentioned earlier, in a purely harmonic crystal there would be no thermal expansion, and this formulation gives an intuitive explanation as to why. The mean position $R$ of each ion remains fixed. The vibrational amplitude may change with temperature but that does not impact the frequency because the spring constant is independent of displacement in this model. This requires us to look beyond the usual harmonic approximation of lattice vibrations.

### 2.2.2 Anharmonic behavior

Starting from the total potential in Eq. (2.4), we must include at least the terms 3rd-order in $u$. Keeping in mind that we are maintaining an assumption of small oscillations we could stop there, but that would yield a very oddly shaped potential with no minimum, the reasoning for which can be found by picturing the asymmetric divergence of any cubic function to $\pm\infty$. Thus to be rigorous the 4th-order terms should also be included. The reasoning behind this is shown graphically in Fig. 2.2. The 3rd- and

4th-order terms of the expansion are, from the same Taylor expansion as before,

$$U_{\text{anh}} = \frac{1}{6}\sum_{R,R'} \frac{\partial^3}{\partial x^3}\,\phi(R-R')\left(u(R)-u(R')\right)^3 + \\ \frac{1}{4}\frac{\partial^4}{\partial x^4}\,\phi(R-R')\left(u(R)-u(R')\right)^4 + O(u^5),$$

and we rewrite Eq. (2.4) as

$$U = U_{\text{st}} + 0 + U_{\text{harm}} + U_{\text{anh}}. \tag{2.6}$$

Including anharmonic terms in lattice potential changes the picture of phonon behavior. Now if we re-calculate the restoring force $F = -\partial U/\partial x$ from Eq. (2.6), we get two additional terms in addition to the harmonic term: $F = Cu + C_1u^2 + C_2u^3$. Plugging this into the equations of motion, $F = m\ddot{u}$, yields frequencies that depend on displacement amplitude. In effect this is a temperature dependence of phonon frequency that has significant thermal expansion consequences.

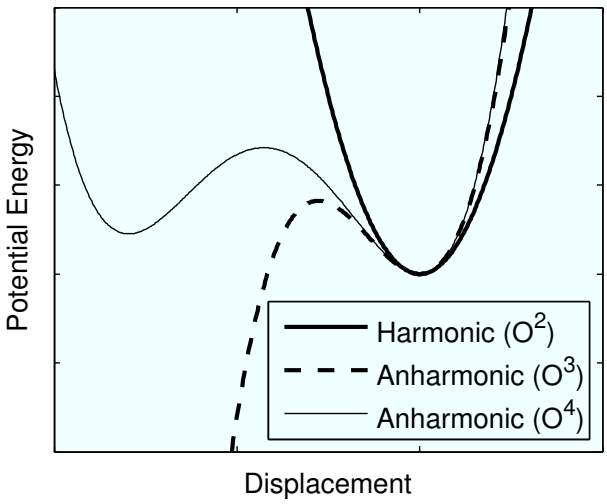


Figure 2.2: A simplified depiction of the shape of potential energy associated with displacement of an atom from equilibrium in three relevant approximations. The parabolic curve depicts a purely harmonic relation, the diverging curve represents an anharmonic model that only includes terms up to 3rd-order showing the unrealistic behavior, and the "W-shaped" curve includes a 4th-order term.

In 3D this is much less intuitive, but the situation is the same. An anharmonic

potential yields phonons with frequency that depends on temperature [5]. This is crucial to our thermal expansion discussion.

### 2.2.3 Phonon dispersion and Debye temperature

In the previous sections we mostly skipped over the concept of phonon dispersion, which is variation in frequency with wavevector $k$. There are many ways to consider this phenomenon, but one in particular plays a key role in the thermal expansion discussion. The Debye model for phonons assumes a low value of $k$, basically limiting lattice vibrations to the macroscopic scale, which allows the acoustic phonon dispersion relation to be reasonably approximated as a linear sound velocity, $v_s = \omega/k$ [4]. This considerably reduces the complexity of the phonon density of states to

$$D(\omega) = \frac{\omega^2}{2\pi^2 v_s^3}. \tag{2.7}$$

$D(\omega)$ is a number of phonon states per unit frequency per unit volume, so $D(\omega)d\omega$ is the number of states contained within $d\omega$ in a unit volume. The Debye cutoff frequency puts a ceiling on phonon frequency at

$$\omega_D = v_s \left(6\pi^2 n\right)^{1/3}, \tag{2.8}$$

where $n$ is the number of primitive unit cells per unit volume, or basically the atomic or molecular number density of a material. The Debye temperature $\theta_D$ is related to that cutoff frequency by the Planck and Boltzmann constants:

$$\theta_D = \hbar\omega_D/k_B. \tag{2.9}$$

Above this temperature all phonon states are already excited and the situation is more-or-less classical as described by Dulong and Petit, where each atom simply contributes $3k_B$ of vibrational energy. Primarily for this reason, $\theta_D$ serves as a key reference point for both theoretical and experimental thermal expansion analysis.[1]

The Debye model can be generalized to allow each acoustic phonon mode to have a distinct sound velocity and thus a unique density of states, cutoff frequency, and

[1] The Debye density of states and Debye temperature are also quite prominent in other solid-state thermal properties, including thermal conductivity, as discussed in Ch. 7.

Debye temperature. A three-dimensional solid has three acoustic phonon modes; one longitudinal mode and two transverse modes.[2] Fig. 2.3 brings these concepts together to give a graphical sense of the Debye approximation in terms of density of states and dispersion.

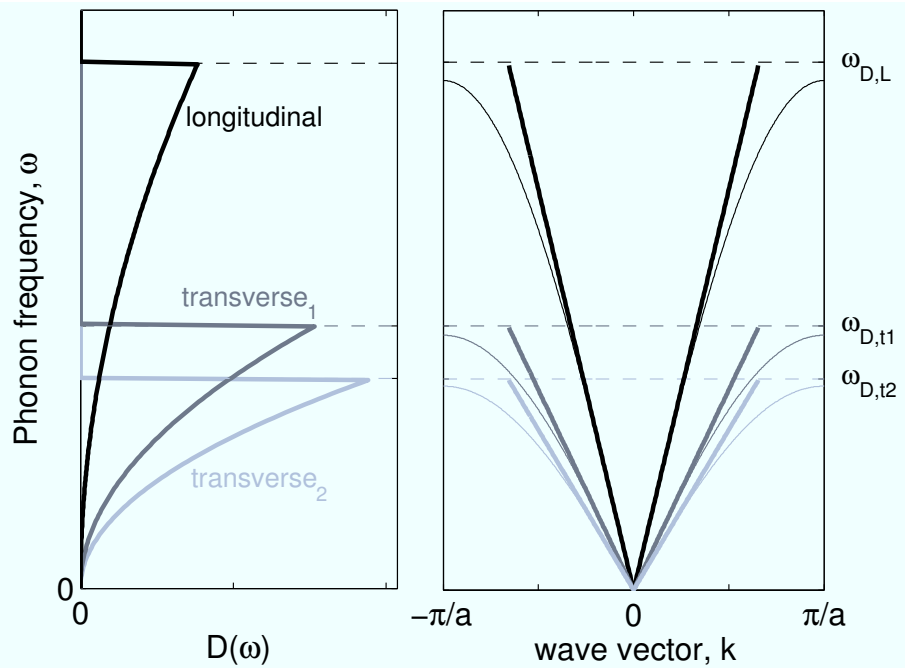


Figure 2.3: A sketch of the Debye density of states, $D(\omega)$, as described by Eqs. 2.7 and 2.8 for the three acoustic phonon modes, and example dispersion relations ($\omega$ vs. $k$) for those modes with and without Debye approximation. The Debye density of states on the left axes is a simple quadratic function of frequency up to each cutoff, $\omega_D$. On the right axes, the full dispersion relations (thinner solid lines) have nearly linear group velocity near $k = 0$ (sound velocity) and zero group velocity (standing waves) at the zone boundaries; in the Debye approximation (thicker solid lines) the group velocity is assumed to be linear up to the cutoff frequency, basically ignoring the presence of standing waves.

The concept of group velocity is important for understanding the dispersion relation, $\omega(k)$, and the consequences of the Debye approximation on $\omega(k)$. Group velocity is the slope of the dispersion relationship, or $d\omega(k)/dk$. Typical acoustic phonon modes

[2] Depending on the material, there also can be optical phonon modes present at higher frequencies that we ignore throughout this dissertation, so named because the vibrational frequencies generally correspond to those of infrared radiation. More info in [3] or [4].

have a nearly linear group velocity for long-range phonons equivalent to the sound velocity through the material, and zero group velocity for the shortest-range phonons that represent standing waves between lattice points. The Debye approximation neglects the shortest-range phonons, instead assuming a constant sound velocity throughout as described above. This essentially means the Debye model is most accurate at lower temperatures, or in cases where we are most interested in propagating phonons (Ch. 7).

## 2.3 Thermal expansion and heat capacity

The coefficient of thermal expansion $\alpha$ of a crystal at temperature $T$, pressure $P$, and having volume $V$ is

$$\alpha(T) = \frac{1}{3V}\left(\frac{\partial V}{\partial T}\right)_P \tag{2.10}$$

for the case of constant-pressure. This is how one would experimentally measure $\alpha$, by observing volume change with temperature. The origins of temperature dependence of $\alpha$ will be discussed later. The factor of 1/3 is present for geometric reasons, namely that this $\alpha$ is the expansion along one direction; volume expansion $\beta = 3\alpha$ in isotropic materials.

Equivalently, $\alpha$ can be defined as a change in pressure with constant volume, or

$$\alpha(T) = \frac{1}{3B}\left(\frac{\partial P}{\partial T}\right)_V, \tag{2.11}$$

where $B$ is the bulk modulus of the solid that links pressure to volume at constant temperature by $B = -V(\partial P/\partial V)_T$. This form is more convenient for theoretical considerations, because the pressure $P$ is what contains the total internal potential of the crystal that was defined harmonically in Eq. (2.4) and anharmonically in Eq. (2.6) above. All of the fuss about the proper expression of potential was because this sort of calculation of thermal expansion involves both the volume and temperature derivatives of the potential. As one might ascertain from the complexity of $U$, it is quite difficult to use it to directly calculate $\alpha$. Instead, the derivation evolves from the well-established phenomenon of phonons and their resulting heat capacity. This only requires one to calculate the volume derivative of phonon frequency, a strictly anharmonic effect as established in § 2.2.2.

### 2.3.1 Heat capacity

Heat capacity is a fairly straightforward phenomenon and has been well-described. It is a change in energy with temperature:

$$C_{_V}(T) = \left(\frac{\partial U}{\partial T}\right)_V \tag{2.12}$$

There are two distinct varieties of heat capacity; that at constant volume which we present here as $C_{_V}$, and $C_{_P}$ at constant pressure. The latter is what is measured experimentally but the former is easier to work with theoretically. They are related by $C_{_P} - C_{_V} = 9\,\alpha^2 BVT$, as noted in Ch. 5 of Kittel [4], with symbols as defined elsewhere in this chapter. Alternatively, specific heat may be used instead which includes normalization by volume:

$$c_{_V}(T) = \frac{1}{V}\left(\frac{\partial U}{\partial T}\right)_V = \frac{C_{_V}(T)}{V}.$$

The result is equivalent, with a simple substitution required later on in Eqs. (2.16) and (2.17).

The contribution from electrons plays a role in some materials, especially metals, but the contribution of lattice vibrations to heat capacity is crucial in all materials. Quantum harmonic theory gives us phonons to describe lattice vibrations as a function of wavevector $\vec{k}$, with the energy of each branch $b$ given by $E_b(\vec{k}) = \hbar\,\omega_b(\vec{k})$ and the number of phonons at each energy described by Bose-Einstein statistics:

$$n_b(\vec{k},T) = \frac{1}{\exp\!\left(\frac{\hbar\,\omega_b(\vec{k})}{k_B T}\right) - 1} \tag{2.13}$$

From there it is a counting game, summing the energies weighted by the temperature derivative of the number of phonons at each energy over all phonon branches[3] and wavevectors. This is heat capacity:

$$C_{_V}(T) = \sum_{\vec{k}b} \hbar\,\omega_b(\vec{k})\frac{\partial}{\partial T}\,n_b(\vec{k},T). \tag{2.14}$$

[3] In 3 dimensions a given material has a number of phonon modes or branches equal to $3p$, where $p$ is the number of atoms in the basis. Each atom in the primitive cell contributes an additional set of vibrations in the 3 orthogonal directions.

The temperature derivative is placed there to emphasize that the number of phonons at each energy is what explicitly changes with temperature, not the phonon energy dispersion relation itself. This is a soluble quantity, especially in the various temperature limits where the derivative of $n_b(\vec{k},T)$ simplifies considerably. The temperature derivative is calculated from Eq. 2.13 to be

$$\frac{\partial n_b(\vec{k},T)}{\partial T} = \frac{\hbar\,\omega_b(\vec{k})}{k_B\,T^2}\frac{\exp\left(\frac{\hbar\,\omega_b(\vec{k})}{k_B T}\right)}{\left(\exp\left(\frac{\hbar\,\omega_b(\vec{k})}{k_B T}\right)-1\right)^2}. \tag{2.15}$$

### 2.3.2 Grüneisen parameters

Thermal expansion is related to heat capacity by a Grüneisen parameter, $\gamma$, that allows the coefficient of thermal expansion (CTE) to be calculated directly from the constant-volume heat capacity $C_{_V}$ and the directly measurable bulk modulus $B$. Starting with a top-down approach seems appropriate, to motivate the introduction of this parameter. The relation is given by

$$\alpha(T) = \frac{\gamma(T)\,C_{_V}(T)}{3BV}. \tag{2.16}$$

Comparing to Eq. (2.11), we can see that we have defined $\gamma(T)$ as

$$\gamma(T) = \frac{V}{C_{_V}}\left(\frac{\partial P}{\partial T}\right)_V \tag{2.17}$$

Note that this is where some authors use different conventions. For example, Ashcroft and Mermin use specific heat rather than heat capacity and adopt the convention that specific heat is per unit volume, so Eq. (2.16) becomes $\alpha = \gamma c_{_V}/3B$. The original 1926 publication by Grüneisen himself is written in German, foreign to this author, but his equations indicate he uses heat capacity, including a volume term in the definition of the $\gamma$ parameter [6]. In any case the Grüneisen parameter must be dimensionless.

#### Mode Grüneisen parameters

The relationship in Eq. (2.16) looks deceptively simple; $\gamma$ is actually a sum of the set of mode Grüneisen parameters, $\gamma_{\vec{k}b}$, which relate to a specific phonon mode with frequency $\omega_b(\vec{k})$. Each of these $\gamma_{\vec{k}b}$ describe the change in $\omega_b(\vec{k})$ with volume, and they must be

normalized to remain dimensionless. Specifically, they are:

$$\gamma_{\vec{k}b} = -\frac{V}{\omega_b(\vec{k})}\frac{\partial\omega_b(\vec{k})}{\partial V}. \tag{2.18}$$

This is often written as partial derivatives of the natural logarithm of each quantity, since both $V$ and $\omega_b$ are always positive and the derivative of a natural logarithm includes the normalizing term, e.g. $\partial \ln V = \partial V/V$. This is precisely where the anharmonic terms are necessary, as without them frequency does not depend on volume and all mode Grüneisen parameters would be zero. That yields zero for the overall Grüneisen parameter and zero thermal expansion.

An additional wrinkle is that the sum over all phonon modes and $\vec{k}$ values to get $\gamma$ also includes the heat capacity of that phonon mode, $C_{Vb}(\vec{k},T)$, as a weighting factor:

$$\gamma(T) = \frac{\sum\limits_{\vec{k}b}\gamma_{\vec{k}b}C_{Vb}(\vec{k},T)}{\sum\limits_{\vec{k}b}C_{Vb}(\vec{k},T)} \tag{2.19}$$

In other words, the phonon modes with the highest heat capacity contribute most strongly to the Grüneisen parameter and to thermal expansion. Each $C_{Vb}(\vec{k},T)$ is just a term in the sum given in Eq. (2.14), the total heat capacity due to phonons.

To recap, the discussion above started with quantities that are accurately defined elsewhere in solid state physics, namely phonon heat capacity and dispersion, and used them to quantitatively describe thermal expansion, a distinctly anharmonic effect. The magic happens in the mode Grüneisen parameters as defined by Eq. (2.18), where phonon frequency has a volume dependence. This basically avoids much of the unpleasantness of dealing with anharmonic terms in the lattice potential while still allowing the equilibrium lattice positions to shift with changes in temperature.

### 2.3.3 Temperature dependence

With the framework above in place to describe the linear CTE, one of the first questions that arises is the temperature dependence of thermal expansion behavior, i.e. $\alpha(T)$. Eq. (2.16) says that if the overall Grüneisen parameter were constant, the linear CTE would have temperature dependence similar to constant-volume specific heat[4] . This

[4] In most materials the bulk modulus $B$ only has weak temperature dependence (as noted by, e.g., [7]), so the only significant contribution comes from $c_V(T)$.

approaches a constant, nearly classical value at large temperatures and approaches $T = 0\,\mathrm{K}$ as $T^3$ [4]. In between the temperature dependence is quite complicated but smooth.

However, the Grüneisen parameter is actually $\gamma(T)$, having its own temperature dependence. The Debye temperature discussed in § 2.2.3 above is used as a reference point. Above the Debye temperature one can no longer reasonably approximate the phonon dispersion relationship as linear (constant sound velocity), but solids behave more classically as all phonon modes are excited. Here the Grüneisen parameter as defined in Eq. (2.19) approaches a constant value commonly referred to as $\gamma_\infty$, typically on the order of 1–3 but there are many exceptions [8].

Below the Debye temperature is where most discussion on expansion of solids seems to focus, since in this region the Grüneisen parameter (and heat capacity) varies considerably. Again in many solids it tends to a constant value at small temperatures, different from $\gamma_\infty$ and referred to as $\gamma_0$. Below roughly $\Theta_D/10$ is where much interesting behavior occurs (both in heat capacity and the Grüneisen parameters) and was a primary advance of researchers through the 1950s and 1960s after Grüneisen's original work. Like heat capacity, thermal expansion goes to zero as T $\rightarrow$ 0 K. Temperature-dependent thermal expansion data on very many materials is available in Grüneisen's original work [6], and several comprehensive reviews since that time containing progressively more low-temperature data [8, 9].

### 2.3.4 Anisotropy

Most of the discussion here has focused on isotropic materials, but more generally the linear expansion coefficient is a second-rank tensor, $\overleftrightarrow{\alpha_{ij}}$. Collins and White [8] define it as the temperature derivative of elastic strain $\overleftrightarrow{\eta_{ij}}$, with the stress tensor $\overleftrightarrow{\sigma_{ij}}$ held constant:

$$\overleftrightarrow{\alpha_{ij}}(T) = \left(\frac{\partial \overleftrightarrow{\eta_{ij}}}{\partial T}\right)_{\overleftrightarrow{\sigma_{ij}}} \tag{2.20}$$

But like many physical tensors, these are symmetric, i.e. $\alpha_{ij} = \alpha_{j\,i}$, so we can signify it as $\tilde{\alpha_i}$ using Voigt notation where $i = 1, 2, \ldots, 6$ such that

$$\tilde{\alpha_i} = (\alpha_1, \alpha_2, \alpha_3, \alpha_4, \alpha_5, \alpha_6) = (\alpha_{11}, \alpha_{22}, \alpha_{33}, \alpha_{23}, \alpha_{13}, \alpha_{12}).$$

These 6 coefficients correspond to the 3 orthogonal directions of expansion along with the unique combinations of cross-coupling between those 3 directions.

Anisotropy manifests itself in the mode Grüneisen parameters, where in its definition in Eq. (2.18) we implied isotropy by finding the volume derivative of phonon frequency using the parameter $V$. More generally, it is a relationship between phonon frequency and the strain tensor (in Voigt notation) given by

$$\tilde{\gamma}_{i,\vec{k}b} = -\frac{1}{\omega_b(\vec{k})}\frac{\partial\,\omega_b(\vec{k})}{\partial\,\tilde{\eta}_i}. \tag{2.21}$$

As before, these mode Grüneisen parameters are summed, weighted by each mode heat capacity, to get an overall Grüneisen tensor:

$$\tilde{\gamma}_i(T) = \frac{\sum\limits_{\vec{k}b} \gamma_{i,\vec{k}b}\, C_{_{V}b}(\vec{k},T)}{\sum\limits_{\vec{k}b} C_{_{V}b}(\vec{k},T)} \tag{2.22}$$

This tensor is analogous to the isotropic overall Grüneisen parameter defined in Eq. (2.19).

As one can see, the situation becomes tedious fairly quickly, but it is an entirely solvable problem. The relationship between the CTE tensor and overall Grüneisen tensor relies on the compliance of the crystal, in general a fourth-rank tensor $\overleftrightarrow{\tilde{s}_{ij\,kl}}$. But again with symmetry it can be written as $\tilde{s}_{ij}$, relating the simplified stress and strain tensors $\tilde{\sigma}_i$ and $\tilde{\eta}_i$. The anisotropic CTE is:

$$\tilde{\alpha}_i(T) = \frac{C_{_{V}}(T)}{V}\sum_{j=1}^{6} s_{ij}\;\gamma_j(T) \tag{2.23}$$

Nothing here is fundamentally different than as described in § 2.3.2; it is simply more general allowing for the Grüneisen parameter and expansion coefficient to have a different value along each direction.

## 2.4 Selected examples

Thermal expansion in solids has been studied for over a century and an impressive amount of data have been reported, covering the spectrum of known material types. As

more materials were studied in new ways and at progressively lower temperatures, the theoretical basis of the field has grown. Accordingly there have been many reviews of progress on the topic that nicely summarize what is known. Examples are Grüneisen's 1926 entry [6], Collins and White in 1964 focusing on the influx of new data below $\Theta_D/10$ [8], and Barron et al. in 1980 [9], who seem to mostly "close the book" on solid-state thermal expansion in light of much data below $\Theta_D/100$ and the amazing theoretical progress that has been made. More recently than that, it seems that much of the discussion is centered on understanding the underlying mechanisms of negative thermal expansion, discussed separately below.

### 2.4.1 Metals

In metals, the role of electrons in thermal expansion must be included. The electron contribution can be estimated rather easily from a free-electron gas model using the general definition of $\alpha$ in Eq. (2.11), substituting the pressure of the electron gas for $P$. It turns out to only be significant relative to lattice vibrations in the vicinity of absolute zero [3] where the phonons are more-or-less "frozen". This is similar to the role of electrons in specific heat, also noticeable only at very low temperature.

### 2.4.2 Negative thermal expansion

There exist many materials that exhibit a *decrease* in atomic spacing upon heating over a certain temperature range. This is termed negative thermal expansion (NTE) due to the change in sign of the linear coefficient $\alpha$. Many decades ago this was mostly confined to some glasses and semiconductors below 200 K and certain metals at $T \ll 100\,\mathrm{K}$ [8]. A relatively recent review by Barrera et al. reveals the study of this class of materials has greatly expanded the portfolio of NTE compounds and it remains an active area of research [10].

#### Zirconium tungstate

Zirconium tungstate, $ZrW_2O_8$, is a particularly interesting material, since it shows isotropic NTE behavior over its entire stable range, from 0.3 to 1050 K [11]. Due to those unique qualities, since the discovery of its NTE properties in 1968 [12] this material

has become somewhat of a "poster child" for negative thermal expansion and has been studied extensively, both theoretically and experimentally, e.g. [5, 7, 13]. It has even been deposited in thin film form, where it has been micromachined to produce NTE micro-optical structures [14] and studied from a materials science perspective [15].

One theoretical study of $ZrW_2O_8$ by Wang and Greeber resulted in the extraction of mode Grüneisen parameters [13] from the assortment of available experimental data, essentially in a search for the phonon modes associated with the volume contraction over temperature. They find that a particular mode at 4.96 meV (57.6 K) corresponds to the dominant negative mode Grüneisen parameter, and it correlates very well with Raman spectroscopy data. Interestingly they propose a direct measurement to confirm their analysis by writing Eq. (2.18) not as a volume derivative of phonon frequency but as its pressure derivative multiplied by bulk modulus, both directly measurable. More recently, Drymiotis et al. studied the elastic constants of $ZrW_2O_8$ in detail and found it to be a relatively "normal" oxide from a harmonic perspective, which primarily involves constant-temperature behavior. Where the material really stands out are in the anharmonic properties that appear upon change in temperature, namely its strongly negative Grüneisen parameter and an unprecedented amount of bulk modulus variation with temperature [7].

## 2.5 Summary

We have described some of the underlying physics of solid-state thermal expansion. It has evolved from the study of phonons and heat capacity, related to the latter by a reasonably simple Grüneisen parameter. The temperature dependence was discussed relative to the Debye temperature as is the established convention both experimentally and in theoretical derivations. The Debye temperature can be well above or below room temperature depending on the material. The thermal expansion coefficient is mostly constant above a material's Debye temperature reflecting the classical behavior of heat capacity. Thermal expansion behavior is complicated in the intermediate temperature range where both heat capacity and the Grüneisen parameter vary considerably with temperature. Thermal expansion vanishes as temperature approaches zero, mirroring the quantum behavior of heat capacity.

# Chapter 3

# Thin film thermal expansion

## 3.1 Overview

Accurate measurement of the coefficient of thermal expansion (CTE) of thin films and the modeling of thermal deformation are crucial components of this dissertation, and they can be quite difficult to properly perform. An in-depth review of the most common methods will be very helpful to understand the advantages and limitations of various techniques before experimental results are presented in Ch. 5. Basic information about the effect of thermal expansion in thin films is covered in §3.2 before moving on to study the particular techniques in §3.3 and 3.4. A brief discussion of non-ideal characteristics that can occur in real films concludes the chapter in §3.5.

## 3.2 Background

The key result of thermal expansion in thin films is that temperature variations essentially cause a change in film stress which manifests as thermal deformation. This is an important consideration in thin-film processing due to the large temperature extremes that can be encountered, but perhaps more important is its effect on the end-use of thin film technologies. Changes in film stress with temperature are induced by mismatch in CTE between the film(s) and substrate, possibly leading to problems ranging from undesirable performance variation to structural failure.

All techniques and variations discussed here rely on some degree of modeling or

fitting, and as such certain assumptions and approximations must be made. All techniques also rely on other material parameters to extract CTE, namely elastic modulus and Poisson ratio.

### 3.2.1 Techniques

There are two prevailing categories of thin film CTE measurement. One set relates curvature measurements to CTE [1, 14, 16–23] and the other involves measurement of variations in film thickness with temperature [24–28].

The latter category is slightly more straightforward and will be described first in §3.3. In all observed cases the technique of x-ray reflectivity (XRR) [24] is used to measure the thickness variations *in-situ* in response to heating [25–28]. XRR is preferred since very fine resolution on the order of angstroms is needed, but the sample need not be crystalline like it would for x-ray diffraction (XRD). The film CTE is related to the change in thickness with temperature, although not as directly as one might assume [27, 28].

A class of techniques more commonly encountered in the literature relies on a relation between curvature measurements and CTE [1, 14, 16–23], and these will be covered in §3.4. The simplest case is a uniform film on a much thicker substrate, where the CTE mismatch between the two materials induces a strain that is proportional to temperature. The strain manifests itself as a change in substrate curvature, which can be measured. The use of at least three different models [16–18] is possible depending on the number of layers and allowable assumptions, and several measurement geometries [14, 19–23]. The two most likely explanations for the prevalence of this technique are its direct relationship to film stress issues, and the fact that measurements can be done with a wide-variety of equipment. The latter has the side-effect of complicating the comparison of results, since the validity of inherent assumptions varies with experiment design [1].

### 3.2.2 Sample preparation

CTE measurement can be performed on a variety of films, with no unique fabrication steps needed. In most cases the only requirement is a film on a substrate, with restrictions on film thickness that depend on the measurement technique. In the case of techniques based on curvature measurements, micromachined structures can be used as well, offering a larger variety of film-substrate geometries for analysis [14, 22]. Multiple thin film layers can even be used, although it complicates the analysis.

## 3.3 Thickness-based measurements

In bulk materials, measurement of CTE is relatively trivial in the simplest case. Heat is applied and the dimensional change is measured directly. Precision can be somewhat more difficult to attain, but the basic idea is there. In thin films, the interfacial constraints inherent to a film-substrate system do not allow this type of direct measurement [27]; detachment from the substrate would be required. This is impractical in thin films due to the small thickness dimension. The idea of direct measurement remains attractive however, and thickness-based CTE measurement techniques are loosely based on the same concept.

The practical thickness-based techniques that continue to be used are based on the ability to measure thickness very precisely [24–28]. Materials exhibit a change in thickness with temperature that can be measured over some temperature range, and the results are modeled to determine out-of-plane CTE [27, 28].

The three important considerations in this section are the method(s) used to measure thickness, resolution limitations, and the significance of out-of-plane CTE.

### 3.3.1 Measurement technique

X-ray reflectivity (XRR) is by far the most commonly used technique for CTE measurements that do not use curvature-based methods.[1] Of particular importance here is the extremely precise thickness resolution of XRR. The achievable resolution depends on several system parameters [24], but generally is roughly 1Å. The thickness resolution

[1] The reader is referred to Chason and Mayer [24] for an in-depth review of XRR.

quoted by Suzuki et al. for their XRR CTE measurements is 1.5 Å [26]; Wu and Liou obtain 0.6–1.4 Å resolution [27]; Bhattacharya et al. observe a resolution of 1.0 Å [25].

The resolution of XRR is put to good use in thin film CTE measurements. This is best illustrated with an example. The nano-clustering silica (NCS) film studied in [26] has fairly typical properties. The film CTE they obtain is approximately 12 ppm/K, meaning that a temperature change of 1 K induces a strain of $12 \times 10^{-6}$ (in an unconstrained film; see §3.3.3). In their 150 nm film, thermal expansion does not induce a great deal of thickness change over a practical temperature range. Even over a substantial temperature range of 225 K, the film thickness only changes by a total of about 7 Å. This film is very typical, both in thickness and CTE. In other XRR CTE studies on different films, by Bhattacharya et al. [25] and Wu and Liou [27], the total thickness variation measured was 8 Å and 5 Å, respectively. It is desirable to measure several intermediate points besides the endpoints, so it is clear that the thickness resolution of XRR was well-utilized in all of these cases.

### 3.3.2 Limitations

The change in thickness with temperature is proportional to film CTE, initial thickness, and temperature range, among other factors (see §3.3.3). If the combination of the three is not large enough to cause thickness to change by a few Å during measurement, then XRR cannot be used to obtain the CTE. To deal with a low CTE, the film can be made thicker so that the absolute change in thickness is larger. But if the film is too thick, greater than several hundred nanometers or so, the thickness is no longer measurable by commercially available XRR equipment [24]. The temperature range should not be too large because CTE is mildly temperature dependent [20]. We have seen that even for a film that is thick by XRR standards (1500 Å), measured over a large temperature range (220 K), and has a CTE that is not particularly small ($\sim$ 12 ppm/K), the CTE can just barely be resolved with XRR. Low film CTE is a serious limitation.

The combination of the two constraints imposed by XRR, i.e. minimum resolution and maximum thickness, creates a problem that cannot be "designed out", contrary to the flexibility offered by curvature-based measurements, as we will see. At least partially as a result of this constraint, the measurement of thickness versus temperature to obtain CTE has been restricted mainly to niche applications with high-CTE films [25–28].

### 3.3.3 Out-of-plane CTE

Perhaps a more pressing issue with the use of thickness measurements to determine CTE is that this technique yields out-of-plane CTE, and it does not even do that directly according to analysis by Wu and Liou [27] and Mukherjee et al. [28]. Consideration of three-dimensional stress-strain relationships indicate that the change in thickness with temperature is not the exact CTE, due to the constraints at the substrate interface and the coupling of strain among axes described by the Poisson ratio. Equation (3.1) is a quantitative statement of these ideas [27].

$$\alpha_{vertical} = \frac{\Delta t}{t \Delta T} - \frac{2\nu_{31}}{\nu_{12}} \left( \alpha_{lateral} - \alpha_s \right) \tag{3.1}$$

In this equation, $\Delta t$ is the measured film thickness change; $t$ is average film thickness; $\Delta T$ is temperature range; $\alpha$ is CTE, where *lateral* and *vertical* subscripts refer to the film and $s$ refers to the substrate; $\nu_{31}$ is vertical-lateral Poisson ratio; $\nu_{12}$ refers to in-plane (biaxial) Poisson ratio.

Using this model, Wu and Liou end up with a measured strain ($\Delta t/t$) of about 40 ppm/K that is converted to vertical CTE of about 20 ppm/K by Eq. (3.1). They make several assumptions to arrive at this result, most notably they assume the two Poisson ratios are 0.35 and they assume $\alpha_{lateral} = \alpha_{vertical}$. The analysis applied by Suzuki et al.[26] follows that presented by Wu and Liou. A different model is applied by Bhattacharya et al. [25], who cite their previous work [28]. They are studying fairly unusual polymer films that are viscoelastic, among other things, necessitating a re-derivation of the strain relationships with a different set of underlying assumptions than those used to derive Eq. (3.1).

After applying the appropriate model, and using both explicit and implicit assumptions, we are still left with out-of-plane CTE. (This is also referred to as normal CTE since it is in the direction normal to the substrate.) This may or may not be the same as in-plane CTE, depending on whether or not the material properties are isotropic. In the above studies these two were assumed equal, since there is no way of measuring in-plane CTE using the techniques described in this section. In-plane CTE is what affects stress variation in thin films, so it would be more useful in many applications to obtain that value more directly.

There are three major conclusions that can be drawn at this point about the thickness technique. It is clear that measuring thickness change is not a direct measurement of thin film CTE due to substrate confinement. It is unclear what the appropriate method is to model the constraining effects of the substrate, although at least two have been suggested [27, 28]. In addition, the result of these measurements is CTE normal to the substrate, which is not highly applicable in many practical situations unless it is assumed equal to in-plane CTE.

## 3.4 Curvature-based measurements

Curvature-based techniques have become somewhat of the de-facto standard in CTE measurement, indicated by their relative dominance in the literature. A small, representative subset is reviewed here [14, 19–23]. The term "standard" is quite loose, because not only are there several measurement techniques, various models an assumptions can be used to extract the film CTE from the data.

### 3.4.1 Modeling thermal deformation

The relevant output of any of the curvature measurement techniques is radius of curvature versus temperature. The radius is obtained by a simple mathematical fit to what is actually measured: a profile of height as it changes with position along the material. That radius of curvature, $R$, gives a common starting point for subsequent discussion of modeling, regardless of the particular measurement technique used. Note that here have already made our first assumption, since "radius" implies linear deformation that yields perfectly circular or spherical curvature. Non-linear deformation generally requires complicated numerical analysis, so efforts are usually made to maintain the validity of the linear assumption during measurement. Often for analytical convenience, the inverse of radius of curvature is used, simply called curvature, and usually represented by $\rho$, where $\rho = 1/R$. (Some authors instead use $\rho$ to mean radius of curvature, which can be confusing, but a quick check of the units will clear up this confusion.)

CTE modeling from curvature data comes in two main varieties, the first being for two-layer systems [16, 17], and the latter applicable in a more general multi-layer case [18]. Obviously a bilayer system is used whenever possible, and an equation from

1909 that is specifically for the thin film case is frequently used, known as the Stoney approximation [16]. This simplest case is a uniform, very thin film on a much thicker uniform substrate. The specific film-substrate system it was applied to in 1909 were films of nickel electrodeposited on steel.

The Stoney analysis, which is a heavy approximation, dominates in the thin film world because its assumptions tend to be fairly valid in the thin film on a substrate case. There are two major assumptions that differentiate it from Timoshenko's 1925 bimetal equation for the same bilayer system [17]: that film thickness is much less than substrate thickness, and the elastic modulus of the film is not substantially larger than the substrate modulus [19].

The Stoney equation relates the radius of curvature at a given temperature to stress, as shown in Eq. (3.2):

$$\sigma_f = \frac{t_s^2}{6t_f}\left(\frac{E_s}{1-\nu_s}\right)\left(\frac{1}{R}-\frac{1}{R_0}\right) \tag{3.2}$$

Before discussing the meaning of all the terms in Eq. (3.2), we rewrite it to eliminate an extraneous term, $R_0$, which is the initial curvature of the substrate, without the film. In thermal curvature measurements we obtain several values of radius of curvature, $R$, at several different temperatures. By subtraction of Eq. (3.2) from itself with two separate values of $R$ (at two different temperatures), it should be clear that we can eliminate the $R_0$. This gives the change in film stress, $\Delta\sigma_f$, rather than absolute film stress, and can be written:

$$\begin{aligned}\Delta\sigma_f &= \frac{t_s^2}{6t_f}\left(\frac{E_s}{1-\nu_s}\right)\left(\frac{1}{R_2}-\frac{1}{R_1}\right)\\ &= \frac{t_s^2}{6t_f}\left(\frac{E_s}{1-\nu_s}\right)\Delta\rho\end{aligned} \tag{3.3}$$

Here subscripts are $f$ for film and $s$ for substrate; $\Delta\sigma_f$ is the change in film stress; $t$ is thickness; $E$ is elastic modulus; $\nu$ is Poisson ratio; $R_1$ and $R_2$ are the radius of curvature at initial and final temperature; $\Delta\rho$ alternatively represents that curvature in inverse units. For small deflections, curvature can be converted to edge deflection $\delta$ for a beam of a given length using the geometrical relation $\delta = \rho L^2/8$. This is also valid for a square plate with edge length $L$ or a disk with diameter $L$.

Armed with Eq. (3.3) we are in the realm of well-known stress-strain theory, and if the experiment is designed properly it maintains the condition of elastic deformation, i.e.

the film is not plastically deformed by the temperature cycling. That means $\sigma_f = \varepsilon E_f$, where $\varepsilon$ is the strain. More specifically, in a two-dimensional system, the elastic modulus $E_f$ is replaced by $E_f/(1-\nu_f)$, referred to as the biaxial modulus. The strain in this case is induced by a change in temperature so it is thermal strain, which is the mismatch in substrate and film CTE, $\Delta\alpha = \alpha_s - \alpha_f$, multiplied by the temperature change, $\Delta T$. The result is Eq. (3.4) for film CTE:

$$\alpha_s - \alpha_f = \frac{\Delta\rho}{\Delta T}\frac{1-\nu_f}{E_f}\frac{E_s}{1-\nu_s}\frac{t_s^2}{6t_f} \tag{3.4}$$

Variables in Eq. (3.4) are as described for Eq. (3.3), with additional terms mentioned immediately above.

Calculating CTE from measurements of curvature is conceptually straight-forward once the Stoney approximation is applied to get film stress. Difficulty does come in when determining the value of $E_f$ and $\nu_f$, and to a lesser extent $E_s$, $\nu_s$, $t_f$, $t_s$, and $\alpha_s$. The film and substrate thickness are relatively easy to measure. Using a well-characterized substrate material can make assumptions of $E_s$, $\nu_s$, and $\alpha_s$ very accurate, and single-crystal silicon offers such a substrate. The biaxial modulus, $E_s/(1-\nu_s)$, of single-crystal silicon is invariant for all directions in the (100) plane and equal to 180.5 GPa [29], and the single-crystal silicon CTE versus temperature was accurately measured and reviewed by Okada and Tokumaru [2]. That leaves the film biaxial modulus, $E_f/(1-\nu_f)$, unknown, and this will be discussed shortly.

More importantly, we must first consider the assumptions made when using the Stoney equation. After all, it does little good to measure the other parameters and plug them into Eq. (3.4) if the derivation is invalid. The assumptions made by Stoney are revisited with the help of the analysis of Freund et al. [1]. They examine Stoney's age-old analysis in the context of its increasing use to measure film stress in systems closer to nanoscale as commonly studied today, and this is briefly reviewed here to summarize some relevant points. Table 3.1 lists the six main assumptions of Stoney.

This is quite a restrictive list that is clearly impossible to achieve exactly. What is done in practice is to get close enough so that the assumptions result in insignificant error. Freund et al. analyze two cases. In the first case, they remove assumption 2, essentially arriving at the result similar to Timoshenko's, which is given below as Eq. (3.5). In the second case, they examine assumption 6, small deformation. That result is

Table 3.1: Main assumptions of Stoney approximation, as given by Freund et al. [1].

| | |
|---|---|
| 1 | Film and substrate thickness is small compared to lateral dimensions. |
| 2 | Film thickness much less than substrate thickness. |
| 3 | Substrate is homogeneous, isotropic, and linearly elastic; film is isotropic. |
| 4 | Edge effects are insignificant; all physical quantities are invariant laterally. |
| 5 | All stress in the thickness direction is insignificant. |
| 6 | Strains and rotations are infinitesimally small. |

not a closed-form equation, but an informative discussion and more rigorous definition of when assumption 6 is valid. This is quite useful, since it provides a quantitative metric for verifying that particular assumption based on simple ratios of film and substrate biaxial moduli and thicknesses. We stop with that for brevity, noting that that Ref. [1] is an excellent resource for proper experiment design and data analysis.

Timoshenko's bimetal equation was mentioned above as a useful analysis when the film is not much thinner than the substrate. The assumptions in Table 3.1 still apply except for assumption 2. This form proves useful in the CTE testing that uses microsystems, since the "substrate" is also a thin film of some sort. Examples with micro-mirrors [14] and micro-cantilever beams [22] will be subsequently discussed. Eq. (3.5) is the bimetal equation [17]:

$$\alpha_s - \alpha_f = \frac{\Delta\rho}{\Delta T} \frac{(t_s + t_f)\left[3(1+m)^2 + (1+mn)\left(m^2 + \frac{1}{mn}\right)\right]}{6\,(1+m^2)} \tag{3.5}$$

where

$$m = \frac{t_f}{t_s}$$

and

$$n = \frac{E_f}{1-\nu_f} \frac{1-\nu_s}{E_s}.$$

The parameters here are the same as for the Stoney-based CTE equation.

Jansen et al. [19], include a "derivation" of Eq. (3.4) from Eq. (3.5), where the term "derivation" is used loosely since Stoney's analysis preceded Timoshenko's by about a decade. This provides a more rigorous look at assumption 2 in Table 3.1. Starting with Eq. (3.5), first it is assumed that film thickness is much less than substrate thickness, i.e. $m \ll 1$, so all $m^2$ terms are neglected. From there, assuming that $m(4n + 1) \ll 1$ results in Eq. (3.4). That condition ensures that the film biaxial modulus is not exorbitantly larger than the substrate modulus, which would essentially multiply its effective thickness.

Multilayer modeling is an extension of the bilayer case, adding much additional mathematical complexity. Due to the complexity, and since CTE measurements can be accomplished in most cases with a film-substrate or analogous bilayer systems, discussion of the multilayer case is covered in Appendix B, along with Stoney-like approximations for multilayers. Briefly, it is indeed very possible to extract a single film's CTE in an otherwise known system with an arbitrary number of layers if the application requires it, and Vasudevan and Johnson present a nice model allowing this [18], although it was not their primary intent. The main caveat is the number of parameters that must be known to extract CTE increases with each additional film layer in the system, as should be expected. Alternative multilayer formulations exist as well, and two more are mentioned here. Feng and Liu presented a model in the form of sum terms [30] rather than the matrix determinant formulation from Vasudevan and Johnson. Hseuh parameterized the multilayer system to reduce the number of unknowns in an interesting approach [31]. All of these subsequently apply their model to various special cases that greatly simplify the calculations when applicable.

### 3.4.2 Thermal curvature measurement techniques

Curvature-based CTE measurement techniques either use wafer curvature or microstructures, with each of those having several variations [14, 19–23, 26]. Equipment requirements are a heating stage, enclosure, and a curvature measurement device, which is predominantly laser based. In general, techniques are either interferometric [14, 22] or they observe deflection of the laser beam caused by changing curvature [19–21, 26].

Wafer curvature measurements are the most basic of the group. The change in wafer

curvature with temperature can be mapped to a change in film stress with temperature, which can then be used to extract CTE based on film parameters, as described in §3.4.1. Commercial film stress measurement tools for the microelectronics industry are widely available, and some enable thermal cycling. Those variations equipped with temperature control have been applied to measure CTE, e.g. [20, 26]. Others have designed "homemade" setups that basically accomplish the same function, perhaps with less automation, e.g. [23].

Similar to the wafer curvature techniques, some researchers have cut strips of film-substrate layers and measured those instead of the whole wafer [14, 19, 21]. Often only a single line along the wafer is measured anyway, making this a likely extension.

The same basic idea can be applied to microstructures, which allow greater control of the thickness ratio between film and "substrate". This ratio can be near unity or less than one, generally meaning that curvature change is much more dramatic over a small temperature range. Examples are use of micro-mirrors [14] and micro-cantilevers [22]. These can be measured in a variety of ways, although in both of these cases interferometry was used to measure curvature.

### 3.4.3 Elastic modulus

Part of the technique in all of these cases must be measurement of film elastic modulus, since it is present in all curvature models used to extract thin film CTE. Nanoindentation[2] is commonly used to estimate this value [14, 26]. Another alternative is to simply assume a bulk value, although this is not a good idea since bulk and thin film mechanical properties are almost never the same. Somewhat better is applying literature results of measurements of other similar films, but finding a match is more rare. Since nanoindentation is time consuming and assumption from bulk is not ideal, researchers have demonstrated another technique, often referred to as the "double-substrate method" [19, 21, 23].

The double-substrate method is an attempt to eliminate the need to separately measure the film biaxial modulus, a considerable barrier to obtaining CTE results. Like it sounds, the method consists of measuring the curvature versus temperature of two

[2] Oliver and Pharr wrote a fairly recent review of nanoindentation that is a good primer on the capabilities of the technique [32].

systems, consisting of the same film deposited on two (or more) different substrates. Referring to Eq. (3.4), it is apparent that in doing this experiment we have added an additional equation without adding an additional unknown to the system, as long as all substrate parameters are known. We can then simultaneously solve for film CTE and biaxial modulus. This is indeed done, e.g. [19, 21]. This was extended by Zhao et al. [23], to additionally allow calculation of Poisson ratio in isotropic films. Their technique involved careful choice of the two substrates, namely one with known isotropic properties (silicon) and the other with known anisotropic properties (single-crystal quartz).

There is a subtle problem with the double-substrate technique, however, and significant errors can result. Thurn and Hughey [20] have described the problem in detail and presented a solution. The problem stems from the temperature-dependence of the film and substrate CTE. This produces significant errors and artificial dependencies in both the CTE and biaxial modulus results for the film. The reader is referred to Thurn and Hughey's analysis for more details and a solution to the problem. A main conclusion is that the results obtained with the conventional double-substrate technique are valid only for the exact temperature range of the experiment, not any subset of that range, since they are an average. The details of the solution they present are somewhat complex and will not be included here, except to say it seems quite robust and even allows the temperature-dependant CTE of the film to be determined experimentally.

### 3.4.4 Comparison of curvature techniques

As we have seen, there are a variety of curvature measurement techniques that have been applied to measure film CTE. The best technique and model among the curvature techniques depends on the degree of accuracy required, the equipment readily available, and the desired end-use of the results.

Accuracy is primarily determined by proper design of the test, unless an improper model is chosen. When modeling, the Stoney approximation is the easiest to apply and understand, but it makes the greatest number of assumptions. If the film thickness is a significant fraction of total thickness then Timoshenko's bimetal model should be used instead, i.e. equation Eq. (3.5) instead of Eq. (3.4). Equation (3.5) may as well be used to verify all bilayer CTE measurements since it involves no additional parameters and insignificant additional calculation effort now that we are over a half-century into the

computer age. If the other assumptions of Eq. (3.5) can not be met, non-linear analysis, usually with finite-element modeling, is required, unless the test design is altered.

Proper design of the test can include many factors. A major one is selection of the substrate thickness to affect the magnitude of curvature change over the temperature range of the test. Equations (3.4) and (3.5) indicate that the magnitude of this curvature change does not only depend on temperature, it depends on the ratio of thickness of film and substrate, and other less crucial parameters. The curvature change should be large enough to be measurable by whatever equipment is used, and small enough to not violate any of the assumptions used in deriving the stress-curvature relationships, especially that strains and rotations are infinitesimally small.

The equipment consideration is fairly straightforward. If one has access to a commercial wafer curvature measurement tool, the obvious solution is to deposit a film on a wafer and test it that way. If instead one has an interferometric microscope and access to microfabrication facilities, perhaps micro-cantilevers or micro-mirrors would be best. End-use considerations are similar, e.g. if one intends to produce thermal bimorphs with micro-cantilevers, one should include micro-cantilevers in CTE tests.

## 3.5 Non-idealities

There are many additional issues to be aware of when performing CTE testing. The details are beyond the scope of this dissertation as many non-idealities each encompass an entire field of research. However, a very brief overview of a few important effects is included here.

The assumptions made in modeling must be verified, of course, and these were discussed previously. Beyond that, some of the major issues can be designed out with a proper measurement process. These issues include hysteresis and dependence of CTE on ambient. Hysteresis occurs because the film changes in some way during heating, although the change need not be irreversible [25]. Films grown or deposited at low temperature often show irreversible changes because the CTE testing effectively anneals the film. Hysteresis should be checked by always testing CTE during temperature cycling, where measurements are performed both while heating and cooling. When this is done, it is readily apparent if the conditions of purely elastic deformation were

maintained throughout the test. Dependence on ambient can be checked by changing the atmosphere and re-testing, either in vacuum or an inert gas like nitrogen. Some films are much more susceptible to these effects than others; dielectrics that are evaporated or grown with plasma-enhanced chemical vapor deposition (PECVD) tend to cause some trouble.

Both of these effects will give inaccurate CTE results if not checked experimentally or otherwise ruled out. Among the cited works, Jansen et al. [19], present a good discussion of hysteresis and changing ambient, but by no means are they the only researchers to investigate these effects. Another good example is work by Thurn, co-author of Ref. [20], who has extensively studied stress hysteresis in PECVD films and published several articles on the subject.

## 3.6 Summary

A review of thin film coefficient of thermal expansion measurements was presented. The two broad categories encountered are based on thickness changes or curvature changes with temperature.

The thickness-based techniques presented here all rely on some form of XRR to measure thickness change in response to temperature variation. After removing the effect of substrate confinement, out-of-plane CTE is the result. One main limitation of the XRR technique is the difficulty measuring low CTE values, since the thickness change becomes too small to measure even with a thickness resolution of about 1 Å. This effect can only be mitigated by increasing the temperature range, which is often not practical. Additionally, the results of the thickness versus temperature measurement do not directly yield CTE. Significant assumptions are made when substrate confinement is removed. A final concern is the limited applicability of out-of-plane CTE values to real-world thin film problems.

In the curvature-based techniques, models are used to extract film CTE from the radius of curvature versus temperature data. The basic idea is the application of what can be considered a three step process from basic mechanical principles, namely stress-strain relationships. The curvature data are converted to film stress, then to strain, which is then mapped to a coefficient of thermal expansion value. The model inputs

are thickness and biaxial modulus of film and substrate plus substrate CTE, or in the case of the double-substrate technique the second substrate CTE takes the place of film biaxial modulus.

It is clear that measuring thin film CTE must be done with great care. Although several intuitive approximations do exist and are often used, verification of the assumptions should be performed before reporting quantitative results. The first question to ask about any report of thin film CTE is, "how did they determine the film modulus?", since the answer will vary widely and affects the reliability of results.

# Chapter 4

# Atomic Layer Deposition

## 4.1 Overview

Atomic layer deposition (ALD) is a thin film growth technique with very unique capabilities that are applied in the context of optical coatings throughout this dissertation. In this chapter we briefly review the history of ALD and discuss the general concept and characteristics in §4.2, including the growth rate per ALD cycle and the concept of a monolayer (§4.2.4); information on specific processes for alumina, hafnia, and silica follows in §4.3. In optical coating applications, ALD remains in niche roles and some examples are included in §4.4.

## 4.2 Background

### 4.2.1 General process

Atomic layer deposition (ALD) is a chemical vapor deposition (CVD) process for the precise formation of thin films. The distinguishing feature of ALD relative to other CVD processes is the isolation of the chemical precursor materials from one another so that they never react directly. They are introduced sequentially in a cyclical process where the first precursor reacts with the surface of the substrate(s) and is then completely purged from the chamber along with any volatile reaction products before the second precursor is introduced. The second precursor reacts with the surface(s) that were chemically modified by the first, forming what can be approximated as a molecular

monolayer. The excess reactant and products are again completely purged, and this cycle is repeated to deposit a film of the desired thickness.

In 2005, Puurunen wrote a review of ALD and a case study of one of the most highly studied ALD film processes, the reaction of trimethylaluminum (TMA) with water to form alumina [33]. In the very detailed review, she also presents a more thorough history of ALD in general than is typically encountered in the literature, particularly the contributions of Soviet scientists to the field. Briefly, the history of ALD goes back to at least the 1960s in the Soviet Union, where it was referred to as "molecular layering" (when translated from Russian). The more commonly recognized birth of ALD was with Suntola and colleagues in the 1970s, who initially referred to the technique as atomic layer epitaxy (ALE) and used it, for example, to grow films of ZnS, GaP, and $SnO_2$ with more stoichiometric precision than could be attained by evaporation or sputtering [34].

### 4.2.2 Advantages

Trading off with the smaller maximum deposition rates than found in other CVD techniques or physical deposition methods like evaporation or sputtering, there are several unique and significant advantages to the ALD approach. The complete purging of precursors between steps leads to self-limiting growth behavior that greatly reduces sensitivity to vapor flow across the chamber and thus leads to high uniformity, even in high-aspect-ratio nanoscale trenches or holes [35–41]. The cyclical nature of the process combined with this self-limiting characteristic means that thickness can be controlled with great precision and accuracy,[1] typically on the scale of 0.1 nm [33]. And since the precursors never interact directly, highly reactive chemicals can be used, which translates into much lower minimum deposition temperatures than in CVD.

It cannot be overstated, however, that ALD differs from CVD essentially only by definition, and non-ideal ALD characteristics lead to CVD growth behavior. Incomplete purging of precursors between steps is by no means easy to achieve, especially because purge time should be minimized to maximize deposition rates.[2] Elers et al. discuss the

[1] ALD is precise meaning relative thickness can be adjusted on the order of 0.1 nm, and accurate in that deposition rates are very consistent so that absolute thickness can be predicted as well.

[2] This point is especially important to stress if developing a new process or in conversations with those unfamiliar with ALD; it is not perfect and requires considerable process optimization.

non-ideal ALD growth behaviors in detail as they relate to chamber and process design [42].

### 4.2.3 Temperature

The temperature at which ALD growth can occur is limited on the low end by the activation energy of the surface reactions (usually relatively low) or the ability to properly purge the precursors. Insufficient reaction energy leads to adsorption or condensation of unreacted precursors, which results in impurities like C or H in the film. Improper purging disrupts the self-termination of reactions that sets ALD apart from CVD, and tends to be more significant if one or more of the precursors are solid at room temperature and pressure rather than liquid.

The upper temperature limit is usually based on the thermal stability of the precursors, where above a certain temperature they can decompose into simpler compounds, again leading to more impurities in the film and disrupting the self-limiting mechanism.

Together, these lower and upper limits define an "ALD growth window" that can vary widely based on specific precursors employed but generally stretches to lower temperatures than available in CVD due to high precursor reactivity.

### 4.2.4 Growth rates

ALD growth rates are expressed on a per-cycle basis due to the alternating nature of an ALD process. One might expect each cycle to give one monolayer of film, but this is not the case. The ligands[3] of the metal-organic precursor can be quite large relative to the metal ion itself, and during an ALD half cycle the ligands of metal ions that have already chemisorbed will obscure adjacent reaction sites. This partial blocking of reaction sites due to the size of molecules is referred to as steric hindrance and ALD growth models have shown this to be a primary cause of the sub-monolayer growth rates, which have been consistently observed to be 15–30% of a monolayer per cycle [33]. This is in the vicinity of 0.1 nm/cycle for oxides. It is analogous to an unfriendly game of musical chairs where players stick their arms out to block adjacent chairs when they sit down.

[3] A ligand in this context is an organic molecule that is bound to the metal ion in a metal-organic compound; for example, in trimethylaluminum, the three ligands are the methyl groups.

To convert these growth rates per cycle to a time basis for comparison to other deposition techniques, the time per cycle is needed. This consists of pulse and purge times for each precursor, and each of these depend on several factors. Overall, the size and shape of the deposition chamber and pumping speed play a large role, particularly for purging, and there are general guidelines for good design [42]. But precursor chemistry also plays a large role and no two processes are equal.

Pulse times are chosen based on the vapor exposure needed at the surface to saturate an individual reaction, where exposure specifically means the product of partial pressure of precursor at the surface and time at that pressure. The partial pressure is essentially the vapor pressure of each precursor, so that is a large consideration in precursor selection and in the choice of each precursor reservoir temperature. The standard technique is to start with a precursor having a reasonable vapor pressure and increase the pulse time until saturation is observed.

Purge times depend a great deal on chamber temperature, since the closer a precursor vapor is to condensation on a surface the more difficult it is to purge. But the purge time also significantly depends on the molecular properties of each precursor in a less intuitive way. For example, at a given temperature below about 200°C, water is 2–3 times more difficult to purge than alkylamide-based precursors of hafnium or zirconium [36]. One could hypothesize this is due to the polar nature of a water molecule, allowing it to form stronger bonds with surfaces that require more energy to break. To give a sense of the amount of variation with temperature, for those same precursors in a particular reactor design, purge times of $< 5$ s at 250°C needed to be increased at 100°C to 120 s for the alkylamide and 300 s for water.

Despite the large number of factors, in reality most ALD systems are designed for optimal precursor delivery and purging, the precursors chosen for ALD have similarly high vapor pressure, and unless temperature is quite low the purging time does not differ much among precursors. Thus the minimum achievable cycle time for typical ALD processes seems to fall within a range of about 2–20 s/cycle. Combined with typical growth near 0.1 nm/cycle, a general range of maximum deposition rates is 0.3–3 nm/min. There are of course exceptions, but this is a useful benchmark.

## 4.3 Specific processes

We are particularly interested in alumina, hafnia, and silica due to their optical properties, and will focus on each of them specifically in this section. Precursors and ALD growth characteristics are discussed along with film properties and applications.

### 4.3.1 Alumina ($Al_2O_3$)

Aluminum oxide has fairly broad appeal as a dielectric thin film due to its combination of electrical, mechanical, and optical properties. It has been formed by ALD using a variety of precursors over the years, with $Al(CH_3)_3$ (TMA) and $AlCl_3$ being the most common metal-containing precursors [33]. A variety of oxidants have been reported as well, including ozone, hydrogen peroxide, and others, but water is the most common, most likely due to its safety and low cost combined with the very adequate reactivity with TMA. The presence of chlorine in $AlCl_3$ reduced its popularity by the late 1990s, as has been the case with other halide-based ALD precursors [33].

As mentioned above (§4.2), Puurunen wrote an extensive review of the TMA and water ALD process to form alumina [33]. This process is conceptually quite simple and has been applied for roughly two decades [43]. A schematic view of the steps is depicted in Fig. 4.1. TMA reacts with an OH-terminated surface during the first half cycle with the hydrogen and some of the methyl groups forming volatile methane products that are purged, leaving behind Al bonded to O. In the second half cycle, the water reacts with the remaining methyl groups to form more methane while leaving behind another OH-terminated surface, this time with an additional partial monolayer of $Al_2O_3$. The next cycle proceeds identically. The steric hindrance in this case results from the methyl groups that remain bonded to the aluminum after the first half cycle. The growth rate per cycle is near 0.1 nm/cycle, with slight inverse temperature dependence that is likely due to a decreasing concentration of OH groups on the surface [33]. Cycle time varies based on reactor design as noted above, but cycle time used for experiments presented throughout this dissertation is 10 s/cycle, giving a growth rate of 0.6 nm/min.

TMA itself is a highly volatile liquid at room temperature and is extremely reactive. It is pyrophoric and it also reacts so strongly with water that the water vapor in air poses an additional concern. This reactivity allows the ALD process to form alumina films

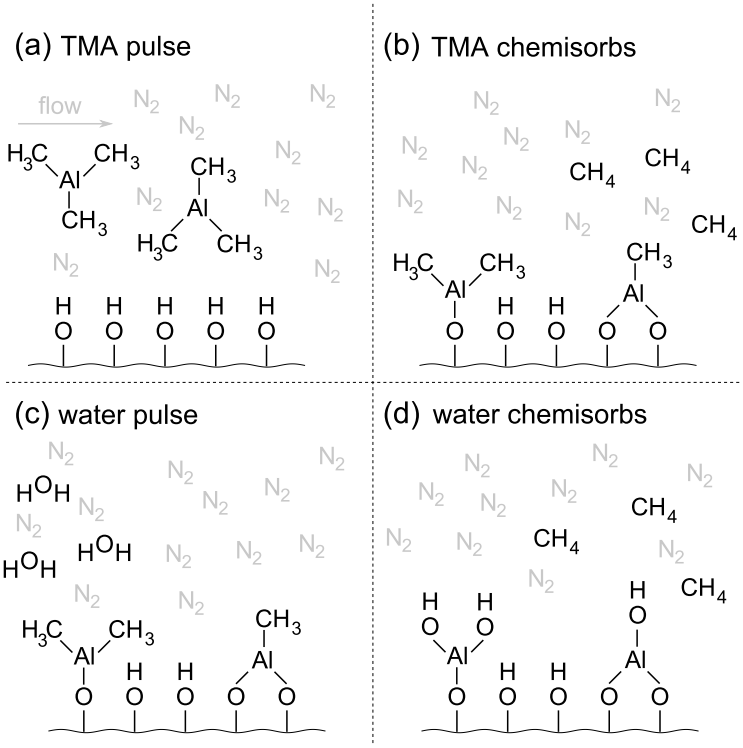


Figure 4.1: A simplified view of one ALD cycle of the TMA/water process, with continuous left-to-right flow of nitrogen carrier gas; (a) TMA is introduced to an OH-terminated surface; (b) TMA reacts with the surface and releases methane, with steric hindrance causing partial coverage; (c) water is introduced after purging; (d) water reacts with the methyl ligands to release more methane, forming a partial monolayer of $Al_2O_3$ with OH termination. (Not shown are excess TMA or water that are purged along with the methane reaction products.)

down to low temperatures, as low as 100°C in early work [43] and more recently down to 50°C, although these very low temperature films have 10–20 at.% hydrogen content [44] and proper purging between steps takes significantly more time. The thermal decomposition of TMA limits "true" ALD processes to $\leq$ 300°C [33, 45], although various earlier reports did produce adequate films at higher temperatures [43, 46].

The ALD alumina films are amorphous, even when deposited at higher temperatures (e.g. 370°C) on various types of substrates [46]. This characteristic has been used to disrupt crystallite growth in other ALD films by forming nanolaminate structures using alumina [47, 48].

ALD alumina is an excellent encapsulant in a variety of applications. Porous silica nanorods having a low refractive index are very susceptible to ambient moisture, with large changes in refractive index and film stress that were eliminated in multilayer optical coatings by finishing with a 100 nm layer of ALD alumina [49]. Encapsulation layers of similar thickness but at much lower deposition temperatures (80°C rather than 250°C) were demonstrated to protect organic light-emitting diodes (OLEDs) from aging using nanolaminates of alumina and zirconia [50]. The nanolaminates were employed because pure alumina layers at that temperature on those organic substrates were found to have localized defects that reduced their effectiveness. Very recently, Carcia et al. have pushed the limits further, characterizing moisture permeation in ultra-thin ALD alumina films grown on polymers at 50°, 75°, and 100°C, finding that 10 nm films are sufficient to prevent permeation at all three growth temperatures, down to at least as thin as 7.5 nm at 100°C [44]. This was despite a large amount of hydrogen impurity in the ALD films, measured to be 10–20 at.%.

ALD alumina has also found its way into the energy business. Two recent examples are use as an additional passivation layer in a monocrystalline Si photovoltaic cell [51], and to increase the cycle life of nanoparticle-based electrodes in lithium-ion batteries [52]. In the solar cell application, 15 nm of alumina was added to help suppress surface recombination, yielding an increase in overall conversion efficiency from $\sim 17\%$ to $\sim 20\%$. In the lithium-ion battery application, extremely thin alumina layers—only two ALD cycles—were applied to $LiCoO_2$ nanoparticle electrodes, more than doubling the charge-discharge life of the batteries. The effect was suspected to be due to the prevention of parasitic side reactions, passivating the nanoparticles while still allowing diffusion of lithium ions, and the ability of ALD to conformally coat complex structures was key to the success.

The mechanical properties of alumina are also advantageous in some applications, and the precision and high-aspect-ratio capability of ALD also find use there. To increase the wear-resistance of microelectromechanical systems (MEMS), 10 nm ALD films have been grown at 170°C on all surfaces of devices after etch release [53]. Some minor non-ideal growth was observed inside some structures due to inadequate purging time, indicating the need for process optimization in such cases. Others have demonstrated a reduction in creep of Au/Si bilayer beams during high-temperature dwells in beams

that were coated after etch release with 40 nm of ALD alumina [54].

In later chapters the TMA/water process is applied to form alumina films at 225–250°C. It was chosen for its utility as a moderately low refractive index optical coating, amorphous nature, and generally excellent film properties.

### 4.3.2 Hafnia ($HfO_2$)

The development of ALD hafnia processes was driven by the need for high-dielectric-constant films, or high-$\kappa$ dielectrics, for use as the gate dielectric in complementary metal oxide semiconductor (CMOS) devices. The gate dielectric must be ultra-thin to achieve the high switching speeds employed in high-performance transistors, and the legacy silicon oxynitride layer would have needed to be 1 nm thick by 2009 and was projected to be 0.75 nm by 2012 [55]. The use of high-$\kappa$ materials instead of silicon oxynitride allows enough physical thickness, at least a few nanometers, to maintain an equivalent electrical thickness while avoiding significant current leakage by tunneling. This problem was foreseen for quite some time and hafnia in general (along with many other materials) was initially studied for this purpose based on sputtering or CVD, with the use of ALD becoming a more prominent idea around the turn of the century. The ALD work was referred to as atomic layer CVD (ALCVD) in a popular 2001 review by Wilk et al [56], another one of the many names used over the decades. Since then and after much development effort that is still ongoing (e.g. [36, 55, 57–66]), ALD-hafnia-based gate dielectrics have become the process of choice for high-performance CMOS [55, 63].

As with other ALD processes, the earliest hafnia work involved halide precursors, specifically $HfCl_4$ [67, 68]. This chloride precursor is very thermally stable, but the incorporation of Cl into the film and possible etching during growth has led to more focus on the alkylamide class of precursors [33, 36, 60]. These are of the form tetrakis($L$)hafnium where $L$ includes dimethylamido [36, 60, 65], diethylamido [36, 58], or ethylmethylamido [36, 65], referred to respectively as TDMAH, TDEAH, and TEMAH. These alkylamides have lower but acceptable thermal decomposition temperatures, falling between 90–150°C for a 1 hour dwell or 350–450°C for a 5 s dwell like that encountered during a purge step in the ALD process [36]. Thermal decomposition in this case means increased C, H, and N content in the film.

The ALD process used to form hafnia films in experiments throughout this work is TDMAH and water. TDMAH is a solid at room temperature. It was held at 75°C because it melts at 30°C, and by 75°C it is a liquid with a vapor pressure of 1 Torr [36]. The growth window is limited to temperatures less than 350°C by thermal decomposition, where N and C impurity levels increase substantially and growth no longer saturates [36, 60]. The low end is less clear, with increasing impurity levels, especially carbon, starting somewhere between 205 and the low-impurity "sweet spot" at 250°C [60], but film deposition is possible down to about 50°C as long as purge times are increased accordingly [36].

Unlike alumina, ALD hafnia films tend to be partially crystalline with monoclinic phase. The degree of crystallinity depends on deposition temperature and film thickness. The crystallinity has been studied by several authors on many film and temperature combinations, and their results are summarized in Table 4.1, focusing on TDMAH and water processes only, although the others are similar [65]. We see that all films up to at least 33 nm are x-ray amorphous, regardless of temperature, and thicker films—near 100 nm—must be deposited at very low temperatures to remain amorphous (albeit with more impurities as noted above). The ability of transmission electron microscopy (TEM) to see crystallites of smaller size than XRD gives slightly different results, indicating that some crystallites form in 250°C films by the time they reach about 10 nm thickness instead of $> 33$ nm. This fits the nucleation model proposed by Hausmann and Gordon [47], where crystallite nucleation events occur randomly with probability increasing with temperature, and crystallite growth from each nucleation site proceeds during subsequent cycles, increasing the film crystallinity with thickness. Crystallinity is correlated to roughness due to the slightly increased crystallite growth rate, and both properties are highly relevant to optical coating applications, where the films will be much thicker than those used for gate dielectric layers. This point will be returned to in Ch. 7 with measurements of crystallinity, roughness, and thermal conductivity of ALD hafnia films at optical thicknesses.

Table 4.1: Summary of previous studies of crystallinity in dimethylamide-based ALD hafnia films at the given deposition temperature $T$ having various thickness $t$. These researchers estimated crystallinity by x-ray diffraction (XRD), scanning probe microscopy (SPM), and/or transmission electron microscopy (TEM).

| T (°C) | t (nm) | Crystallinity | Technique(s) | Ref. |
|---|---|---|---|---|
| 50 | 100 | amorphous | XRD | [47] |
| 100 | 100 | $\sim$ 0–4% monoclinic | XRD and SPM | [47] |
| 150 | 100 | $\sim$ 2–10% monoclinic | XRD and SPM | [47] |
| 200 | 100 | $\sim$ 10–20% monoclinic | XRD and SPM | [47] |
| 250 | 5.6 | amorphous | TEM | [64] |
| 250 | 11.8 | 5–10% crystalline | TEM | [64] |
| 250 | 20.0 | 20–30% crystalline | TEM | [64] |
| 250 | 20–30 | amorphous | XRD | [60] |
| 250 | 100 | $\sim$ 65% monoclinic | XRD | [47] |
| 275 | 33.5 | amorphous | XRD | [65] |
| 275 | 76 | partially monoclinic | XRD | [65] |
| 300 | 100 | 100% monoclinic | XRD | [47] |

The growth mechanism of hafnia using TDMAH and water shown in Fig. 4.2 is reasonably intuitive and agrees fairly well with mass measurements using a quartz crystal microbalance (QCM) [36, 69]. The starting surface is terminated with OH, either naturally from reaction of surfaces with water vapor in ambient air or from the previous ALD cycle. Each TDMAH molecule ($Hf[NMe_2]_4$ where "Me" is $-CH_3$) reacts with two OH sites, with the two H combining with two of the four $NMe_2$ ligands to form two volatile dimethylamines ($HNMe_2$) while the Hf ion bonds to both newly exposed O ions. Now the surface contains new $HfO_2$ sites with each Hf atom having two remaining $NMe_2$ ligands. Excess TDMAH and products are purged. The pulse of water molecules reacts with the $NMe_2$ ligands on the surface to form more dimethylamines, leaving behind OH in their place. Excess water and products are purged, and the condition of the surface is

now identical to the beginning of the cycle but with an additional partial monolayer of $HfO_2$. As mentioned in the general description above, steric hindrance occurs to reduce the growth per cycle to less than one monolayer. In this specific case, the two $NMe_2$ ligands on each chemisorbed Hf atom are blocking TDMAH from reaching adjacent OH sites. The growth rate per cycle is 0.09 nm/cycle [36], about 20% of a 0.5 nm $HfO_2$ monolayer.

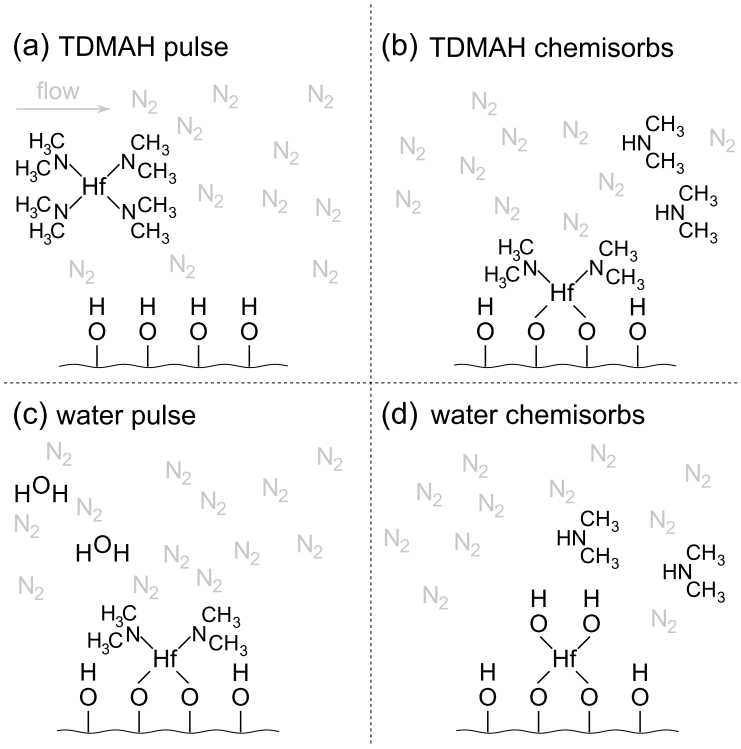


Figure 4.2: A simplified view of one ALD cycle of the TDMAH/water process, with continuous left-to-right flow of nitrogen carrier gas; (a) TDMAH is introduced to an OH-terminated surface; (b) TDMAH reacts with the surface and releases dimethylamines, with steric hindrance by dimethylamide ligands causing partial coverage; (c) water is introduced after purging; (d) water reacts with the dimethylamide ligands to release more dimethylamine, forming a partial monolayer of $HfO_2$ with OH termination. (Not shown are excess TDMAH or water that are purged along with reaction products.)

The proposed growth mechanism predicts a mass gain during the first half cycle of one Hf atom and two $NMe_2$ ligands minus the loss of two H ions, and it predicts a mass loss during the second half cycle of two $NMe_2$ ligands minus the gain of two OH groups.

The net gain/loss ratio is then (Hf + 2$NMe_2$ - 2H)/(2$NMe_2$ - 2OH), evaluating to 4.9 from molecular weights, agreeing reasonably well with the $\sim$ 5.7 ratio observed in a QCM measurement.[4]

### 4.3.3 Silica ($SiO_2$)

The practical growth of silicon dioxide films by ALD has proven difficult to achieve. Early work was again with water and halide precursors, specifically the chloride, $SiCl_4$. Through most of the 1990s the processes required temperatures $> 300°C$ and vapor exposures $> 10^3$ Torr s as noted by Klaus et al. in 1997 [70], which would translate to tens of minutes per cycle at typical pressures. These drawbacks were mitigated by introducing a pyridine ($C_5H_5N$) catalyst to the process, which yielded growth at room temperature with exposures closer to 1 Torr s or about 60 s per cycle, with a cycle yielding 0.2 nm. This was a considerable advance, but still about 3 times slower than ALD processes for other materials (§4.2.4).

The most promising techniques to date originated from a "rapid vapor deposition" process reported in 2002 [35] involving the precursors TMA and tris(*tert*-butoxy)silanol ([$(Bu^tO)_3SiOH$] or TBS, where "$Bu^t$" is a $-C_4H_9$ *tert*-butyl group and *tert* refers to its arrangement). This approach yielded films that did have a self-limited growth characteristic similar to standard ALD processes but each cycle of TMA followed by TBS produced up to 32 monolayers rather than the usual fraction of 1 monolayer. Each 12 nm of silica was achieved in a cycle lasting 30 s or less ($\geq$24 nm/min), which is not only much faster than the catalyzed growth reported by Klaus et al. ($\sim$0.2 nm/min) but is also much faster than all other oxide ALD growth processes (around 0.6 nm/min). A mechanism was proposed whereby the Al in TMA served as a catalyst for a polymerization reaction of the TBS, eventually saturating when access to the catalyst was sufficiently reduced by polymer thickness and cross-linking. The complex set of reactions involved yields a saturated growth rate per cycle versus temperature that forms a very narrow window from 225–250°C where 12 nm/cycle can be achieved. Growth was still found to saturate in an ALD-like fashion between 200° and 300°C, but the growth

[4] The TDMAH/water QCM measurement is shown in Fig. 6-1 on p. 103 of Hausmann's PhD thesis[69], where the mass gain/loss ratio is between about 5.3 and 6.1. The agreement is much better for the very chemically similar process of $ZrO_2$ grown by TDMAZr, with 3.28 predicted and 3.3 measured [36].

per cycle was very sensitive to temperature, dropping as low as 6 nm/cycle within that range.

The TBS process was not specific to an Al catalyst, and similar films were later grown using Zr- [71] and Hf-based [62] catalysts. An interesting application of the TMA/TBS process was its use to seal the surface of a porous low-$\kappa$ dielectric film with silica to prevent subsequent penetration of the pores by an ALD diffusion barrier coating of tungsten nitride [38]. The silica process was optimized to avoid conformal coating in that case so that it would not penetrate the pores, and the fast polymerization-based mechanism was key in sealing the surface.

An important evolution was reported near the end of 2008 by Burton et al., who used tris(*tert*-pentoxy)silanol (TPS) rather than –butoxy because it has several more-desirable qualities. It is a liquid at room temperature rather than a solid, has a higher vapor pressure, and showed rapid vapor deposition as low as 125°C and much less sensitivity of the growth rate to vapor exposure [72]. Tying it all together with some of the original pyridine-catalyzed-silica ALD work mentioned above, they also investigated the effects of a pyridine-based impurity in the TPS and indeed found significant effects on growth.

Some processing with TMA/TBS to grow rapid-vapor-deposited silica was attempted to complement the alumina and hafnia ALD films in the thermal deformation work presented in Ch. 5, but nothing noteworthy was achieved due to the difficulty in getting the process to work reliably. Perhaps the TPS process could have fared better, but too late for this work. The state of ALD or rapid-vapor-deposited silica remains highly specialized and generally not an available process in commercial deposition systems.

## 4.4 Application to optical coatings

Optical coatings have a set of requirements that matches up fairly well with the capabilities of ALD: precise and accurate control of thickness, consistent refractive indices, sharp transitions between materials in multilayers, and fully dense films that are stable in presence of water. The one glaring drawback is the need for relatively large thickness. Individual visible-wavelength coating layers are on the order of 50–100 nm to achieve quarter-wave optical thickness, and multilayer designs can easily contain tens

or hundreds of these layers. Infrared coatings are substantially thicker, especially the mid-wave (3–5 $\mu$m wavelength) and long-wave ($\sim$ 8–14 $\mu$m wavelength) regions. The time required to achieve enough thickness is a serious limitation and to date seems to have prevented large-scale adoption of ALD by the optical coating community.[5]

The specific use of ALD for optical applications was "introduced" in the scientific literature by Riihelä et al. in 1996 [73], citing the method's precise control of thickness as a primary advantage and giving several examples of coatings that take advantage of it. The most interesting examples were the two Fabry-Perot filters, a 12-layer and a 20-layer design, where the position of the actual transmission resonance matched the design exceptionally well. There was some deviation in the side bands, especially in the 20-layer design, which was mostly attributed to thickness issues in the uppermost layers due to depletion of the precursors near the end of the 16-hour deposition. It almost goes without saying that the slow deposition rate was cited as the most serious shortcoming of the technique, and roughness was mentioned as well.

The TMA/TBS or TMA/TPS processes presented in §4.3.3 represent one possible avenue for overcoming the primary drawback, but as noted above, these remain nascent processes. Specifically embracing this uniquely high growth rate, Willey presented a "fence post" design methodology for antireflection coatings and filters to maximize the proportion of silica, with only thin layers of a high-refractive-index material [74]. That theoretical study was aimed at making ALD more practical for optical coatings, but does not yet appear to have been cited. However, the TMA/TBS process has been applied to protect optical components from chemical corrosion [75].

Besides the slow growth rates, crystallinity and roughness are the other significant drawback pertaining to optical coatings. As noted in §4.3.2 on hafnia, ALD films tend to become more rough with increasing thickness due to growth of crystallites. Nanolaminates are one possible solution to the roughness problem, and have been explored in various contexts. Smooth and amorphous zirconia/alumina and hafnia/alumina nanolaminates with total thicknesses around 100 nm were presented for general use [47]. Specifically for optical purposes, a titania/alumina nanolaminate has been grown by ALD to

[5] This was certainly the case at Optical Interference Coatings 2010, a topical conference held every three years covering all aspects of dielectric optical coatings, and attended by academic, government, and corporate researchers and engineers. Various sputtering or ion-assisted evaporation techniques were by far the dominant deposition methods employed, with ALD playing a minor, exploratory role.

produce a titania-rich film that is amorphous to improve surface roughness and laser damage threshold [48]. These same researchers had previously demonstrated smooth tuning of the refractive index of ALD alumina-titania nanolaminate films from 1.9 to 2.3, then used the result to make a nearly ideal narrowband antireflection coating for Si [76].

### 4.4.1 Metal fluorides

Metal fluorides are one important "missing link" for ALD to achieve broader appeal in optics. In 1994, a handful of ALD metal fluorides were presented with a focus on optical coatings, including an example 21-layer ultraviolet (UV) filter using ZnS and $SrF_2$ [77]. It was not explicitly noted but it can be inferred that this 930 nm thick coating took several hours to grow, which is actually quite reasonable relative to other coating methods. This is quite fast by ALD standards (§4.2.4), for two reasons. The coating was primarily ZnS, which has a growth rate per cycle close to 0.2 nm/cycle, twice that of typical ALD films. Also, the purge times between half cycles were $<$ 1 s, which is quite fast, although it is not clear that complete purging and self-limiting growth was verified.

Despite this early and promising entry, practical ALD fluorides remain more elusive than oxides, having limited success due to the need for a fluorine-based precursor that tends to be incompatible with most oxide films; dreaded HF vapor was used in the 1994 work. Only recently has notable progress been made [78–80], and it included ALD of perhaps the most optically significant flouride, $MgF_2$, important due to its unique combination of low refractive index ($\sim$ 1.38) and low absorption into the vacuum UV ($<$ 200 nm wavelength). The initial breakthrough was the use of $TiF_4$ as the fluorine source rather than HF, but those films contained enough Ti impurity to affect the UV transparency [78]. The follow-up work used $TaF_5$ instead, and was a fairly successful process [80]. Films could be grown between 225 and 400°C, but the level of impurity was unacceptable for UV transparency until 350°C or higher. Unfortunately, as is the case for ALD hafnia as described above in §4.3.2, the higher temperature films had unacceptable levels of surface roughness and were polycrystalline. The particular films studied were rather thick, however, and it would be interesting to see the thickness threshold for this crystallinity and roughness. A nanolaminate approach may not work

as well in this case, because the desired properties of low-refractive index and UV transparency could be affected substantially by inclusion of a film such as alumina.

### 4.4.2 Scandia

Scandium oxide, or $Sc_2O_3$, is another technologically significant optical coating because, like hafnia, it is a high-refractive-index material with a sufficiently large bandgap energy to show good resistance to laser damage [81, 82]. Not much work has been done on the ALD of scandia, however, as it is primarily used for optical coatings and thus is usually prepared by evaporation or sputtering.

It appears that there have been only two reports of ALD scandia. Putkonen et al. made the original leap from CVD to ALD in 2001 [83], trying both a $\beta$-diketonate precursor that had been applied in CVD and a novel cyclopentadienyl (CPD) precursor, with various oxidants. The CPD precursor resulted in much higher growth rates per cycle than the $\beta$-diketonate, as was expected due to the smaller ligands that reduce steric hindrance (§4.2.4). The ALD growth window with the CPD precursor was around 200°C up to 350°C, but it again forces a choice between impurities or roughness. The 130–150 nm thick films were only smooth when $\leq 250$°C, where RMS roughness was $<$ 2 nm. Unfortunately, there was also considerable H and C impurity in the films unless deposited above 300°C, where RMS roughness was at least 5 nm.

The second report of ALD scandia used an amidinate-based precursor [40], a new class of precursors that has only been in use for ALD since 2003 [33]. Their stated goal was to produce amorphous films and electrically characterize them, both missing from the earlier work. The ALD growth window was found to be about 290–360°C, with a growth rate per cycle about half that of the CPD-based scandia and a strong temperature dependence. The films were smooth and nearly amorphous, although they were only grown up to 40 nm so it is difficult to compare directly to the CPD-based films. The C and N impurity levels were $<$ 1 at.%, but the H impurities were not measured.

It is worth noting that the original ALD scandia work was followed up with ALD of $YScO_3$ films in 2006 [84], and although it was targeted as a next-generation high-$\kappa$ dielectric, the films were amorphous and smooth and could perhaps have optical use as well.

ALD of scandia, like metal fluorides and rapid silica, is possible but remains very much in the early development stage, and is unlikely to show up in optical coatings in the near term. It is likely (but untested) that a nanolaminate approach similar to that for hafnia could be used to get around the tradeoff between impurities at lower temperatures and roughness at higher temperatures for optically-relevant thicknesses. For example, the CPD-based scandia process from [83] could be run at 300°C along with ALD alumina by TMA and water to form nanolaminates. Carbon and H impurities in the scandia were very low at $\geq$ 300°C, and this is within the alumina ALD growth window as well (§4.3.1).

### 4.4.3 Backside coating

The highly conformal nature of ALD presents a rather peculiar problem for some applications, particularly in glass optics where the coatings on front and back surfaces serve a purpose. It is difficult to prevent ALD growth on all surfaces of a substrate, including nearly all of a bottom surface even if the substrate is resting on it. The points of contact will be determined by the curvature of the back surface. This curvature need not be noticeable to the eye, which can come as a surprise; even the slight curvature of a "flat" silicon wafer allows enough penetration of vapor to coat much of the backside.

Polyimide film (e.g. DuPont Kapton® HN) was found to be a useful bulk material for the prevention of ALD growth where it was not desired. It can be cut to shape, withstands the growth temperatures, and was indeed impermeable to the precursor vapors, but adhesion of a bulk film to surfaces especially near the edges proved too troublesome for reliable use. Polyimide tape that employs a high-temperature adhesive (e.g. 3M 5419) easily fixes the adhesion problem and is removable after deposition, but breakage of thin substrates during tape removal can occur. Spin-on polyimide thin films were not attempted, nor were self-assembled monolayers [85].

In the thermal deformation work on thin substrates in Ch. 5, the backside-coating issue was mitigated by positioning the substrate to allow conformal coating of both sides, then ion milling the coating off of the backside with argon.

On the other hand, this characteristic can be an advantage. Nearly identical coatings could be formed simultaneously on both sides of a substrate, and multiple samples can be stacked to increase process throughput. The extreme conformality over large areas

within narrow channels was embraced and characterized in the work presented in Ch. 6, with applications in general ALD processing, waveguides, or encapsulation.

## 4.5 Summary

There are several key points to take away from this chapter about atomic layer deposition.

The advantages of properly optimized ALD processes are precise and accurate control of thickness at a scale $< 1\,\text{nm}$, conformal coating of high-aspect-ratio structures, and lower deposition temperatures than general CVD. Growth temperature will affect the impurity content of the film and its morphology.

The two primary drawbacks of slow growth rate and high roughness are particularly detrimental in optical coatings (as opposed to gate dielectrics) because both issues become worse when individual film layers are $\gtrsim$ 20–50 nm. ALD-like rapid growth of silica is an interesting approach to the first issue, and it is definitely a topic to watch. Nanolaminates are a potential strategy to reduce the roughness problem in thicker films, as has been investigated by previous researchers and will be expanded with new work presented in Ch. 7.

ALD alumina has proven to be a very versatile film, shown to encapsulate, passivate, or otherwise protect polymers, solar cells, OLEDs, MEMS, and others. It remains amorphous at any practical thickness and pinhole-free down to 50°C. ALD hafnia is now used by Intel and others as a high-performance gate dielectric, but crystallites and roughness appear around 20–40 nm so use in optical coatings requires more attention. These two films are applied experimentally in the remaining chapters, using TMA/water and TDMAH/water precursors, respectively.

# Chapter 5

# Control of thermal deformation

## 5.1 Overview

In this chapter, a mechanical design technique for optical coatings is reported that simultaneously controls thermal deformation and optical reflectivity, relying on atomic layer deposition (ALD) to produce very consistent mechanical and optical film properties.

The method presented in §5.2 requires measurement of the refractive index and thermal stress of single films prior to design. An eight layer $Al_2O_3/HfO_2$ distributed Bragg reflector was designed with a predicted peak reflectivity and thermal deformation, and measurements of the actual structure matched both predictions closely.

Leveraging those results that indicate highly predictable films by ALD, simulations of various ALD coatings in §5.3 demonstrate curvature invariance with minimal impact on the optical characteristics of high-reflectivity mirrors.

Much of the work in this chapter was published in *Optics Letters* in 2009 [86] or presented at Optical Interference Coatings 2010 [87].

## 5.2 Repeatable thermomechanical behavior

### 5.2.1 Introduction

The design of optical coatings has traditionally focused on the spectral characteristics of the multilayers. This is, of course, the primary function of a coating, but when coatings are used in extreme environments or at high optical powers, or are deposited on

membranes or micromechanical structures, mechanical effects can cause unwanted shape changes that degrade the performance of the optical system. Under these conditions, the mechanical design of a multilayer stack can be just as important as the optical.

Fortunately, the linear mechanics of multilayer films have been known for some decades. As discussed in §3.4.1 and Appendix B, one of the most prominent early applications of this theory was in the development of bi-metal thermostats [17]. This theory was extended to multilayers by Vasudevan and Johnson [18]. It has been previously applied to optical coating design by Liu and Talghader [88]. In their work, a distributed Bragg reflector was designed and deposited and then its thermal deformation and spectral properties were measured. A bilayer coating was subsequently used to adjust the mechanical deformation with minimal impact on the optics. However, since this work required that the coating be deposited in two steps to allow for an intermediate measurement of the coating properties, it is not optimal for production optics.

It would be ideal to be able to design the mechanics of a coating using known material constants before the films are deposited. However, one of the major difficulties is that the mechanical properties of a coating, specifically the coefficient of thermal expansion (CTE) and elastic modulus, tend to drift or vary from run to run, particularly using sputtering techniques, where there are many variables that can affect the properties of a film. Atomic layer deposition (ALD), however, is a chemical deposition technique where growth rate, density, and composition are tightly controlled by the nature of the process, as discussed in Ch. 4, making it suitable for *a priori* optomechanical design. In ALD, alternating vapor pulses of each precursor material are applied to a heated substrate, with complete purging between pulses. These sequential surface reactions are self-limiting, leading to considerable film thickness precision and uniformity. Each set of precursor pulses is one "cycle", and by simply controlling the number of cycles one can obtain very precise film thickness.

In this section, we present an optomechanical design technique where the thermal stress and refractive index of single films are measured and then used to design high-reflectivity coatings with specific spectral and deformation properties. ALD has been chosen as the deposition process because of its expected high run-to-run repeatability. The thermomechanical model is the previously mentioned linear multilayer thermostat analysis[18] as described in Appendix B, and the silicon wafers used as substrates for

these high-reflectivity coatings are well-approximated as linear free-plates. Optically, we use the matrix method presented by Yeh [89] and detailed in Appendix C, which is valid for a wide range of layered media under plane wave illumination.

Specifically, we consider a dielectric mirror consisting of alternating layers of ALD alumina ($Al_2O_3$) (§4.3.1) and hafnia ($HfO_2$) (§4.3.2) deposited on 100 mm diameter 250 $\mu$m thin (100) silicon wafers. All films were deposited at 225°C in a commercial Savannah S200 reactor from Cambridge NanoTech. $Al_2O_3$ was deposited using water and trimethylaluminum (TMA) precursors kept at room temperature, and $HfO_2$ with water and heated tetrakis(dimethylamido)hafnium (TDMAH) at 75°C. A process pressure of approximately 1 Torr and purge time of 5 s between precursor pulses was used.

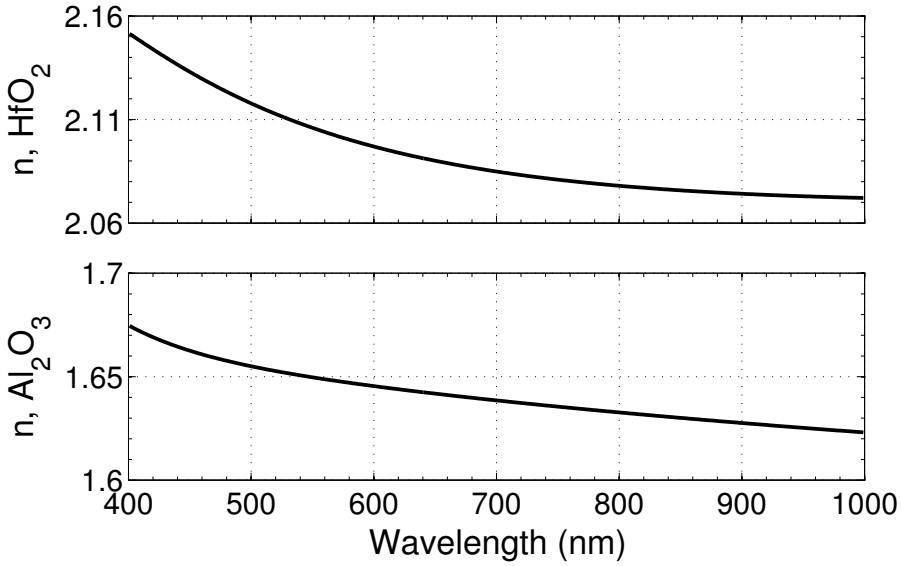


Figure 5.1: Parametric fits of the refractive indices of $Al_2O_3$ and $HfO_2$ to VASE measurement data using a modified 4-parameter Cauchy model that includes an inverse wavelength term. Parameters are given in Table 5.1.

### 5.2.2 Single film characterization

Single films of each material were deposited, with film thickness and optical constants measured by variable-angle spectroscopic ellipsometry (VASE) over the wavelength range 400–1000 nm using a J.A. Woollam VASE tool. The deposition rate for $Al_2O_3$

Table 5.1: Cauchy parameters for alumina and hafnia dispersion obtained from VASE measurements and plotted in Fig. 5.1, valid using Eq. 5.1 where $\lambda$ is in the range 0.400–1.000 $\mu$m.

| Parameter | alumina | hafnia |
|---|---|---|
| A | 1.5556 | 2.1038 |
| B | $+9.5191 \times 10^{-2}$ | $-8.0734 \times 10^{-2}$ |
| C | $-2.9381 \times 10^{-2}$ | $+5.078 \times 10^{-2}$ |
| D | $+1.6618 \times 10^{-3}$ | $-1.728 \times 10^{-3}$ |

was found to be 0.1155 nm/cycle and the rate for $HfO_2$ was 0.096 nm/cycle. These values were used to choose the number of cycles to obtain desired thickness in subsequent runs. The dispersion was fit to a modified Cauchy model, with an additional inverse wavelength term included to slightly improve the fit. This is Eq. (5.1), where $n$ is the real part of refractive index, $\lambda$ is wavelength, and the four remaining terms are fit parameters. The results of fitting dispersion to this modified Cauchy model using VASE data are shown in Fig. 5.1 with parameters in Table 5.1. These refractive index results are the main fixed inputs to the optical design simulation.

$$n(\lambda) = A + \frac{B}{\lambda} + \frac{C}{\lambda^2} + \frac{D}{\lambda^4} \tag{5.1}$$

In order to simulate the thermal deformation, the CTE and biaxial modulus of each layer must be measured or otherwise determined. The biaxial modulus of single-crystal silicon is invariant for all directions in the (100) plane and equal to 180.5 GPa [29]. The silicon CTE is taken from data reported by Okada and Tokumaru [2]. Those data are CTE vs. temperature over a very wide range; here an average value over the applicable temperature range is used, *i.e.* 3.13 ppm/K over the range 30–200°C.

The film parameters were extracted from measurements of wafer curvature over temperature on the same single films of $Al_2O_3$ and $HfO_2$ deposited on silicon wafers. These measurements were performed with a Frontier Semiconductor FSM-900TC, which uses an optical lever technique to measure curvature, with continuous water cooling and heating provided by an array of tungsten-halogen lamps. Each measurement consisted of six temperature cycles 30–200°C, ramping up at 5°C/min and partially controlled

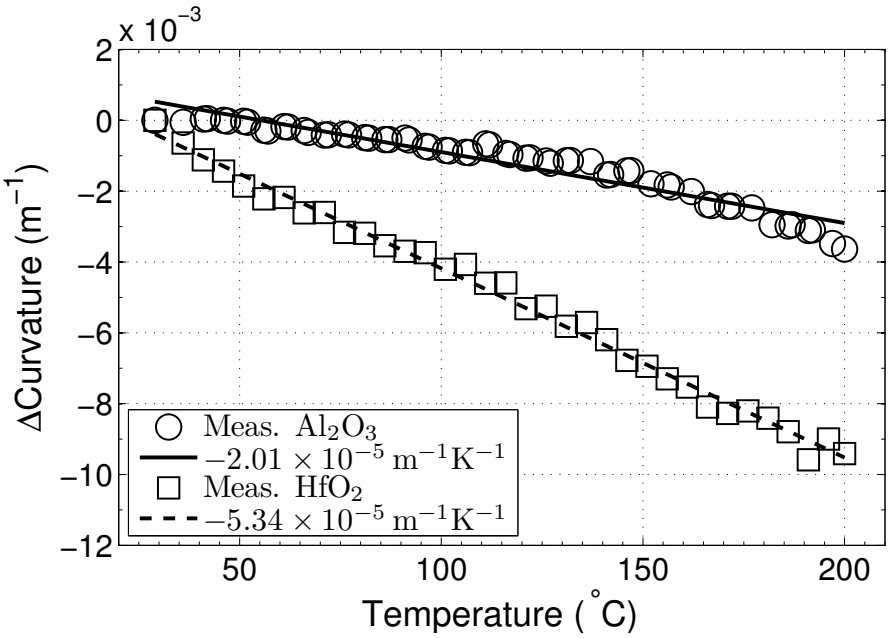


Figure 5.2: Measurement of single-film thermal expansion-induced change in curvature with temperature for $Al_2O_3$ and $HfO_2$ on silicon, with a linear fit shown for each.

cooling no faster than $-5$°C/min. The average values from the heating portion of the relative curvature vs. temperature data from cycles 2–6 were used. The result for $Al_2O_3$ and $HfO_2$ films is shown in Fig. 5.2, along with linear fits. Instead of using the aforementioned multilayer model in this case—a single film on a much thicker substrate—it is easier to use the Stoney equation to relate the curvature data to useful parameters as described in §3.4.1. Briefly, Eq. (5.2) gives film stress from measurements of curvature:

$$\sigma_f = \frac{E'_s t_s^2}{6 t_f} \rho. \tag{5.2}$$

Here $\sigma_f$ is film stress, $E'_s$ is substrate biaxial modulus, $t$ is substrate or film thickness, and $\rho$ is substrate curvature (inverse radius of curvature). The change in film stress we observe is related to elastic thermal strain, $\epsilon_T$, by $\mathrm{d}\sigma_f = \epsilon_T E'_f$, and this thermal strain is due to CTE mismatch between film and substrate over a given change in temperature $\mathrm{d}T$, or $\epsilon_T = (\alpha_s - \alpha_f)\,\mathrm{d}T$. Thus we arrive at the result in Eq. (5.3) expressing thermal stress.

$$\frac{\mathrm{d}\sigma_f}{\mathrm{d}T} = (\alpha_s - \alpha_f)\, E'_f \tag{5.3}$$

Equating (5.3) and the derivative of (5.2) with respect to temperature, we find the following:

$$(\alpha_s - \alpha_f)\, E'_f = \frac{E'_s t_s^2}{6 t_f} \frac{\mathrm{d}\rho}{\mathrm{d}T} \tag{5.4}$$

Eq. (5.4) is our desired result to convert the measured $\mathrm{d}\rho/\mathrm{d}T$ into physical parameters for use in simulation. The coefficient in front of $\mathrm{d}\rho/\mathrm{d}T$ is effectively a constant, obtained using the aforementioned $E'_s$ assumption for silicon and film thickness measurements, plus substrate thickness measurements with a Fowler step gauge (251.5 $\mu$m for the $Al_2O_3$ system and 254 $\mu$m for $HfO_2$). In our case we find thermal stress, $\mathrm{d}\sigma/\mathrm{d}T$, to be $-0.435$ MPa/K for $Al_2O_3$ and $-1.47$ MPa/K for $HfO_2$. The single-film measurement results are presented in Table 5.2.

Table 5.2: Summary of single-film measurement parameters and results.

| Parameter | symbol | alumina | hafnia | units |
|---|---|---|---|---|
| Growth temperature | – | 225 | 225 | °C |
| Refractive index | $n$ | Table 5.1 | | |
| Thermal curvature | $\mathrm{d}\rho/\mathrm{d}T$ | $-0.0201$ | $-0.0534$ | $\mathrm{km}^{-1}\mathrm{K}^{-1}$ |
| Substrate modulus[a] | $E'_s$ | 180.5 | 180.5 | GPa |
| Substrate thickness | $t_s$ | 251.5 | 254 | $\mu$m |
| Film thickness | $t_f$ | 87.95 | 70.45 | nm |
| ALD cycles | – | 762 | 733 | cycles |
| $t_f$ per cycle | – | 0.1154 | 0.0961 | nm/cycle |
| Thermal stress | $\mathrm{d}\sigma_f/\mathrm{d}T$ | $-0.435$ | $-1.47$ | MPa/K |

[a]From [29], which calculated biaxial modulus for (100) Si based on crystal structure.

### 5.2.3 An eight-layer mirror

An 8-layer quarter-wave distributed Bragg reflector (DBR) centered on 550 nm wavelength (at normal incidence) was chosen to demonstrate the concept. Quarter-wave layers of our $Al_2O_3$ and $HfO_2$ films at this wavelength have thickness 83.3 nm and 65.2 nm, respectively, corresponding to iterations of 721 and 680 ALD cycles. The reflectance of the fabricated coating was measured with the spectroscopic ellipsometer at

15° from normal incidence using fixed $s$ polarization. The 15° angle was included in the simulation, causing the designed 550 nm center wavelength to occur at 542.4 nm. The result is shown in Fig. 5.3, with good agreement seen between design and theory. The actual peak reflectance of 85.7% at 541.7 nm is below the predicted 87.9% peak by 2.2% (a 2.5% relative error), but the peak wavelength error is only −0.7 nm (0.13% error).

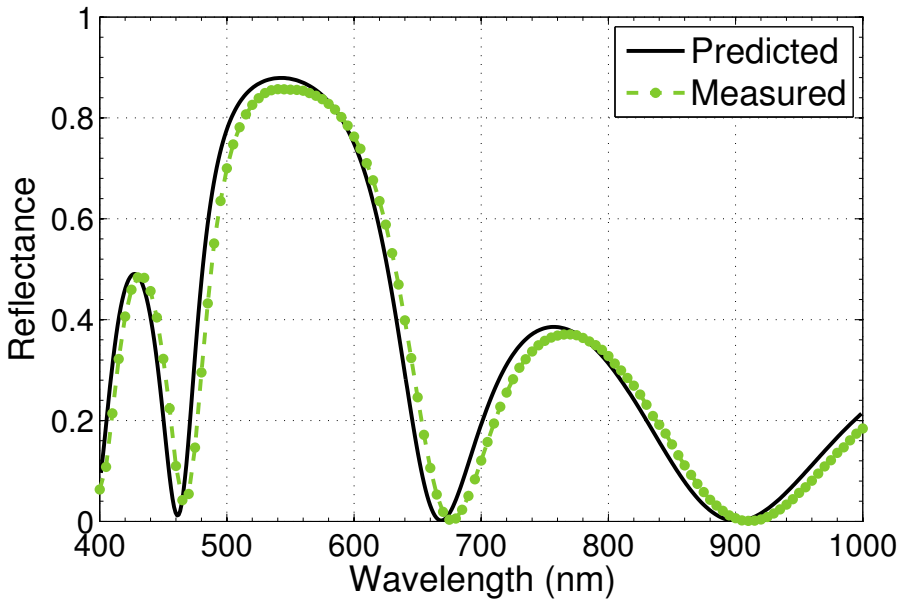


Figure 5.3: Comparison of simulated and measured reflectivity data for the 4-pair multilayer at 15° from normal incidence using $s$-polarized light.

The thermal deformation of the 4-pair DBR was predicted using the model in Appendix B with the thermal stress values extracted from the single-film measurements as inputs. But since the model uses CTE and biaxial modulus separately, we assumed arbitrary film biaxial moduli and found the corresponding film CTE from Eq. (5.3). Doing so is valid because it can be shown for this thick substrate special case that the exact linear model based on independent CTE and modulus parameters in [18] reduces to one requiring only thermal stress. This is derived in §B.2 of the Appendix. It is also analogous to "special case 3" presented in [30] and the "zero-order approximation" in [31].

Thermal deformation of the 4-pair DBR was measured between 30–200°C, yielding the result in Fig. 5.4. The predicted value of $-2.88 \times 10^{-4}\,\mathrm{m^{-1}K^{-1}}$ nearly matches

the linear fit to the data of $-2.77 \times 10^{-4}\,\mathrm{m}^{-1}\mathrm{K}^{-1}$. This is an error of $-3.8\%$. The close agreement with prediction suggests reliable deposition rates along with repeatable thermal expansion behavior of each film. This result was achieved in spite of deposition runs being separated by several weeks in a shared laboratory setting, with no special attention paid to usage by other users nor any pre-conditioning of the process equipment prior to each coating run. Also, all 6 heat cycles are shown in Fig. 5.4 including the first one, with no sign of stress hysteresis like there typically is in films deposited at these moderately low temperatures [88, 90]. This is an indication that the films are not porous or the encapsulation abilities of ALD alumina described in §4.3.1 are again at work. The lack of hysteresis is characteristic of high-quality films like silicon nitride deposited at much higher temperatures, $> 800°\mathrm{C}$ [91].

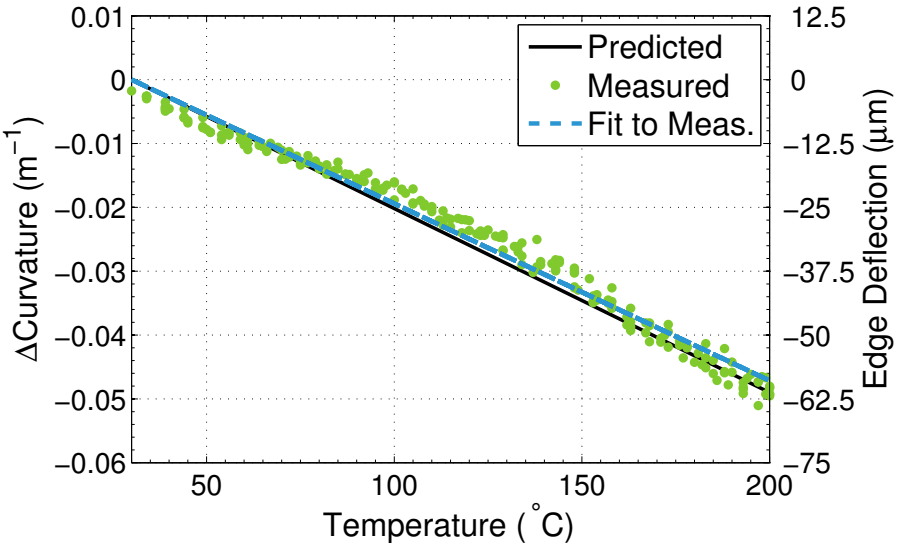


Figure 5.4: Relative wafer curvature vs. temperature for the 4-pair design, comparing the simulated prediction to actual measurement (all 6 heat cycles are shown). The equivalent edge deflection is shown at the right.

The result in Fig. 5.4 is plotted both in terms of curvature and converted to edge deflection, $\delta$. The two are related by $\delta \approx \rho L^2/8$ for small deflections. In our case $L = 0.1$ m, yielding a predicted thermal edge deflection of $-360\,\mathrm{nm/K}$ compared to an actual measurement of $-346\,\mathrm{nm/K}$.

## 5.3 Achieving curvature invariance

### 5.3.1 Introduction

As the thickness of an optical substrate decreases, thin-film coatings have an increasing mechanical impact, leading to changes in curvature with temperature, humidity, or other environmental factors. In many designs this impact needs to be accounted for, and in some cases removed completely. This adds additional complexity for system designers who will not only need to know the detailed optical properties of the substrate and coating materials but also will need detailed thermomechanical material properties. In a perfect world this would be a fairly simple characterization task, but in general, process engineers cannot guarantee these properties will be constant over time in any real process. A variety of *in situ* monitoring techniques have been developed to continuously deal with variation in optical properties, but thermomechanical properties usually must be measured after the fact, making any mechanical design susceptible to error due to drift in parameters. Atomic layer deposition (ALD) is a coating technology that produces thin films with particularly repeatable properties, and, as such, lends itself well to this problem.

In this section, we extrapolate the work described in the previous section where we demonstrated an ability to accurately predict the optical and thermomechanical performance of an ALD multilayer mirror based on straightforward a priori measurements. The results will be used to demonstrate mirror designs that achieve curvature invariance as defined in Appendix B.2.

### 5.3.2 Summary of previous results

In §5.2, thin films of aluminum oxide ($Al_2O_3$) and hafnium oxide ($HfO_2$) were deposited by ALD on silicon substrates approximately 250 $\mu$m thick at a temperature of 225°C. The parameters needed to design a high-reflectance mirror from these two materials were obtained from spectroscopic ellipsometry measurements of each single film. Specifically, we obtained the deposition rate along with the refractive index as a function of wavelength from 400-1000 nm. Thermomechanical measurements were also performed on the single films from 30-200°C, yielding thermal stress parameters of -0.435 MPa/K for $Al_2O_3$ and -1.47 MPa/K for $HfO_2$, using the well-known biaxial modulus value for

single-crystal silicon.

Thermal stress is also a product of a film's thermal expansion mismatch with the substrate and its own biaxial modulus, so if desired, film CTE can be extracted from these results with independent knowledge of the film's biaxial modulus and the substrate CTE. However, if the substrate remains consistent and the film layers behave linearly then the thermal stress parameters alone are sufficient for modeling multilayer systems; this was demonstrated in 5.2. The extracted parameters were used to design a four-pair distributed Bragg reflector (DBR) mirror with 500 nm resonance. The mirror was then fabricated based on precisely determined ALD parameters and measured, yielding optical and thermomechanical performance nearly identical to the design without any adjustment or empirical fitting needed.

### 5.3.3 On D263 glass substrate

The ultimate goal is to be able to influence the thermally-induced curvature of a mirror through small changes in individual layer thickness, and do this reliably at the design stage. This is similar to the concept for thermally invariant micromirrors demonstrated in [88], but without the need for an iterative approach with multiple measurement and deposition steps. The work in §5.2 demonstrates such a predictive ability that avoids the need for iteration by relying on the temporal stability of ALD coating processes. However, both ALD $Al_2O_3$ and $HfO_2$ have larger CTE than that of silicon, indicated by the similar sign of their measured values of thermal stress; both negative. Unless coatings are applied to both sides of the substrate, this Si/ALD $Al_2O_3$/ALD $HfO_2$ system will always curve in one direction with increasing temperature, never achieving thermal invariance. Fig. 5.5 illustrates this effect in the asymptotic behavior of the $Al_2O_3$ and $HfO_2$ thermal stress curves as they approach the Si CTE.

We propose that one would be able to achieve thermal invariance using ALD $Al_2O_3$ and $HfO_2$ by switching to a substrate with a moderately larger coefficient of thermal expansion than silicon, such as Schott D263 glass, which has an average CTE of 7.2 ppm/K (ppm $\equiv 10^{-6}$) when measured over a range 20-300°C and is presently available in thicknesses down to 30 $\mu$m [92]. In Fig. 5.5 we can see both films cross this D263 CTE value. With additional knowledge of the biaxial modulus of each film, we can reduce the curve in each case to a single point associated with a specific CTE value.

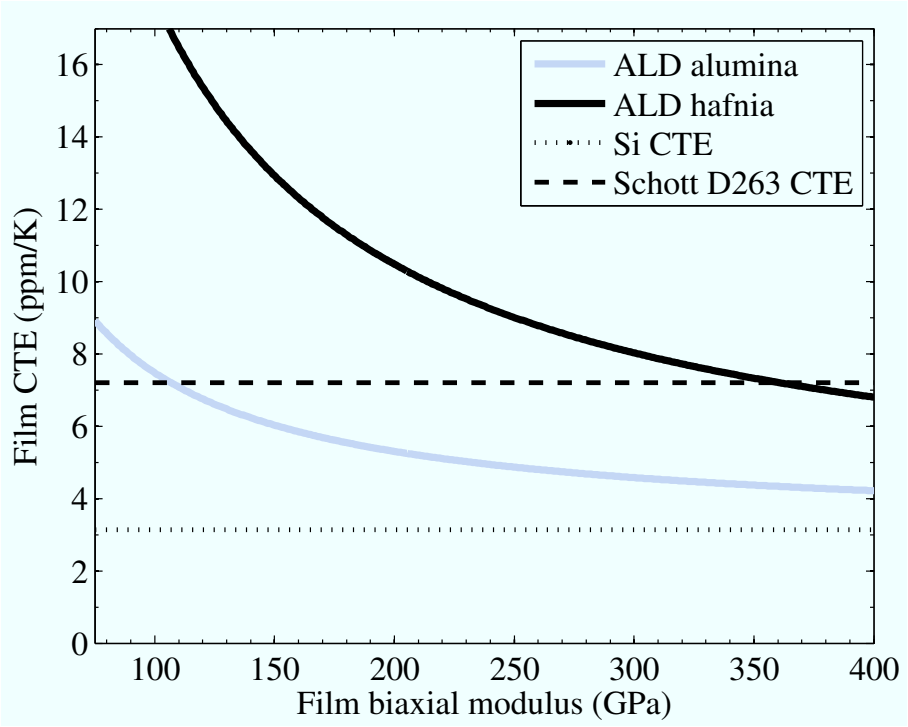


Figure 5.5: Possible combinations of CTE and biaxial modulus associated with thermal stress parameters reported in §5.2: $-0.435\,\mathrm{MPa/K}$ for alumina and $-1.47\,\mathrm{MPa/K}$ for hafnia. Thermal stress determines a line in the CTE-modulus plane; an independent measurement of biaxial modulus is needed to extract actual CTE. Si and Schott D263 glass CTE are shown for reference.

The biaxial modulus of a nearly identical ALD $Al_2O_3$ film was estimated to be 247 GPa by nanoindentation measurements [49], yielding an $Al_2O_3$ CTE value of 4.89 ppm/K based on Fig. 5.5. Tapily et al. also performed nanoindentation on ALD $Al_2O_3$ along with ALD $HfO_2$ [93], both deposited under conditions very similar to our films, notably using identical precursor materials and similar substrate temperatures. They found the biaxial moduli of both films to be roughly $314 \pm 57\,\mathrm{GPa}$ (calculated from the Young's moduli of $220 \pm 40\,\mathrm{GPa}$ and assumed Poisson ratio of 0.3 that was actually reported in [93]). Nanoindentation is notoriously susceptible to measurement and analytical errors [32], so this amount of variation is to be expected. In light of this uncertainty, we will consider three cases in the range given: both films having biaxial modulus of 260 GPa, 310 GPa, or 370 GPa.

We can see qualitatively from Fig. 5.5 that having film biaxial moduli near 260 GPa would be a fairly good situation for achieving thermal invariance on D263 glass using these ALD $Al_2O_3$ and $HfO_2$ films in a multilayer mirror coating. In that case, the CTE difference between each coating and the D263 substrate is quite similar but opposite in sign, thus upon a change in temperature the two films will "push" roughly equally in opposing directions. On the other hand, if both films actually have biaxial moduli near 370 GPa, the upper limit measured in [93], we would be faced with an impossible task because both films would have CTE less than the 7.2 ppm/K of the D263 glass, and upon heating would "push" the substrate curvature in the same direction. In reality the situation will be between those extremes. To get a quantitative sense of what is achievable in the D263 glass/ALD $Al_2O_3$/ALD $HfO_2$ system, we perform optical and thermomechanical simulations using the known material parameters along with assumed film biaxial moduli of 260 GPa or 310 GPa. As before, we choose an arbitrary design resonance for demonstration, 500 nm wavelength.

Schott D263 glass has a vendor-reported CTE of 7.2 ppm/K in this temperature range and a biaxial modulus of 92.0 GPa, where biaxial modulus is $E/(1-\nu)$ when $E = 72.9$ GPa and $\nu = 0.208$ [92]. First, assuming moduli of 260 GPa for both films, from Fig. 5.5 we obtain an $Al_2O_3$ CTE of 4.80 ppm/K and an $HfO_2$ CTE of 8.78 ppm/K. Along with the refractive index curves measured in 5.2, we simulate the linear thermal deformation and multilayer optical performance exactly as was done in §5.2. These 260 GPa simulation results are shown in Fig. 5.6, depicting a standard five-pair quarter-wave DBR along with a six-pair DBR design using modified layer thickness to yield near-zero thermal deformation without sacrificing reflectance at peak resonance. The results are much less ideal if we assume film biaxial moduli of 310 GPa, as one could infer from the curves in Fig. 5.5 at 310 GPa where $Al_2O_3$ CTE is 4.54 ppm/K and $HfO_2$ CTE is 7.87 ppm/K, much less evenly distributed about the 7.2 ppm/K line. A quantitative 310 GPa result is shown in Fig. 5.7, where in this case the modified thermally-invariant design has 8 additional layers for a total of 18 but still yields peak reflectance 0.023 below the 0.800 peak in the nominal 5-pair quarter-wave design. Thermal invariance comes at a much higher cost because the films are not well matched to the substrate, too far from the thermal-invariance condition in Eq. (B.12).

One could certainly apply other schemes of achieving thermal invariance in addition

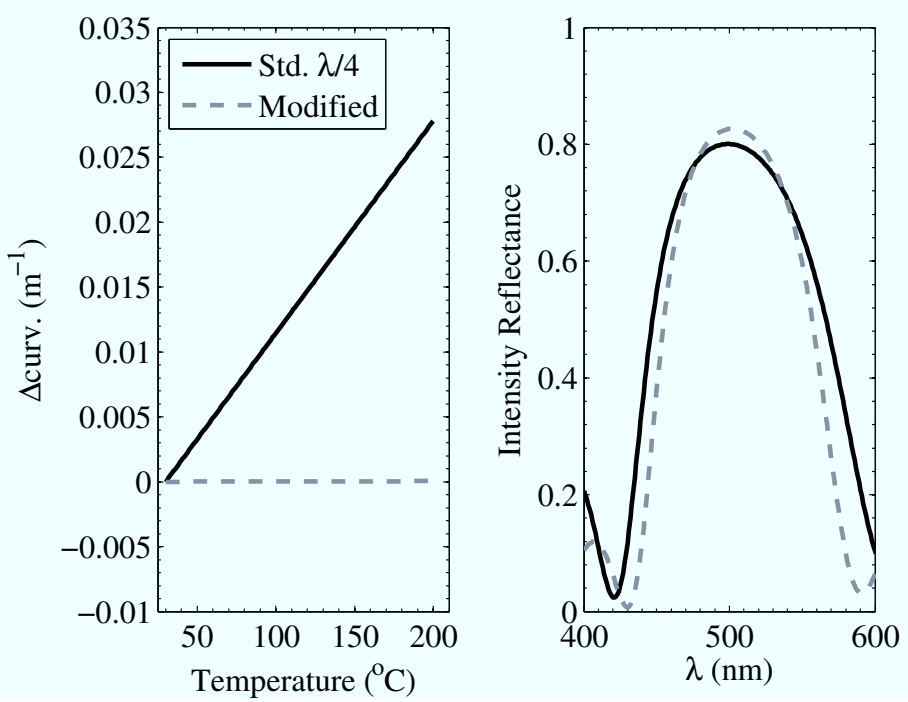


Figure 5.6: Thermomechanical and optical simulations of ALD hafnia alumina DBRs on D263 glass, assuming both film biaxial moduli are 260 GPa. The solid lines are a five-pair DBR with standard quarter wave thicknesses of 75.5 nm and 59.0 nm for alumina and hafnia, respectively. The dashed lines are a modified DBR with one additional pair and where each alumina layer thickness was decreased to 50.6 nm and each hafnia layer thickness was increased to 76.7 nm; this yields near-zero thermal deformation, but slightly increased peak reflectance due to the additional two layers.

to the technique used above, where all $Al_2O_3$ layer thicknesses are kept equal to one another as are all $HfO_2$ layers. A full minimization search will yield an optimum design depending on the relative weight given to optical and thermal performance parameters. But at this stage, the more simple approach yields great insight into the importance of choosing the proper starting materials and sets reasonable expectations for the range of parameters that will yield acceptable results.

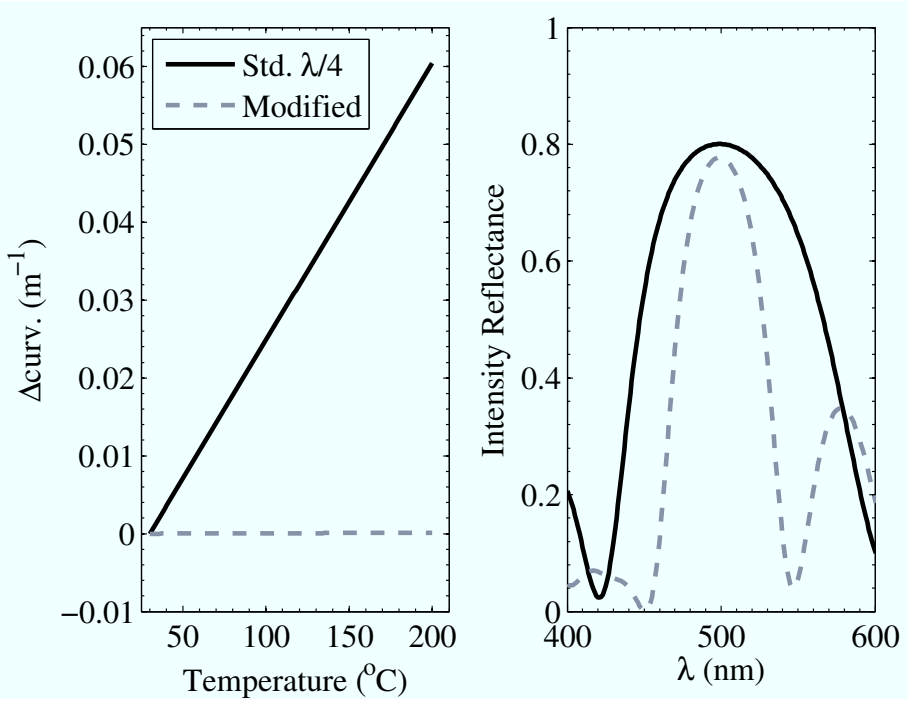


Figure 5.7: Simulations of ALD hafnia alumina DBRs on D263 glass, assuming both film biaxial moduli are 310 GPa. The solid lines are the same design as in Fig. 5.6 with updated modulus. The dashed lines are a modified DBR with four additional pairs and where each alumina layer thickness was decreased to 24.1 nm and each hafnia layer thickness was increased to 95.6 nm, indicating the much less ideal situation at 310 GPa.

## 5.4 Summary

A mechanical design technique for optical coatings has been shown that simultaneously controls thermal deformation and optical reflectivity. This method only requires knowledge of refractive index, CTE, and elastic modulus of single layers of the films that will compose the desired multilayer stack. The method will have great utility for optical coatings that must withstand large temperature swings or high optical powers. It also benefits coatings deposited on membranes or micromechanical components.

We applied this to the thermally invariant mirror problem through simulations of the same films but on a commercially available thin glass substrate, Schott D263, which has a more appropriate CTE. The change in substrate introduces some uncertainty such that film biaxial moduli must be assumed based on nanoindentation measurements, but

other properties needed for simulations were obtained from actual measurements. Two cases were simulated for a nominally five-pair DBR with 500 nm resonance. If both film's biaxial moduli are closer to 310 GPa, it is fairly difficult to achieve thermal invariance, with many additional pairs needed to make up the drop in reflectance caused by the layer thickness modifications. However, if film biaxial moduli are actually closer to 260 GPa, a thermally invariant mirror can be achieved at a cost of only one additional pair in the design. The results suggest that the D263 glass/ALD $Al_2O_3$/ALD $HfO_2$ system is very promising if thermally invariant mirrors are needed for a given application, and further investigation is warranted.

# Chapter 6

# ALD in channels

## 6.1 Overview

High-aspect-ratio channels may be coated using atomic layer deposition (ALD) due to the unique self-limiting nature of the process, and as mentioned in Ch. 4, this has been often demonstrated using nanoscale deep reactive-ion etched (DRIE) holes or trenches in silicon. However, for optical and microfluidic applications, many channels are centimeters deep with diameters of tens to hundreds of micrometers and the relatively large area exposes more difficult problems of temperature and gas flow uniformity.

To quantify the uniformity of optical coatings deposited by ALD under those conditions, in §6.3, an air wedge has been created between two square wafers of silicon approximately 7 cm on a side, with the air gap varying linearly from 0-1560 $\mu$m. Single-film results in §6.4.1 show that ALD alumina uniformity is astounding, while hafnia shows a need for process optimization but still exceeds the capability observed in other deposition techniques. In §6.4.2, a six-layer Fabry-Pérot optical cavity with fixed 500 nm resonance was deposited inside a wedge, and the measured resonant wavelength closely matched predictions except at the deepest regions of the wedge.

The work in this section was published in *Applied Optics* in March 2010 [94].

## 6.2 Motivation

The self-limiting nature of atomic layer deposition (ALD) is often demonstrated by coating deep trenches or holes etched into silicon wafers. These structures are usually many micrometers deep with an opening having sub-micrometer dimensions [35, 36, 38, 40, 41], often used to form nanoscale capacitors in dynamic random access memory (DRAM) technology. ALD has also been put to practical use in the manufacture of electroluminescent and liquid crystal displays on large pieces of glass [34, 95], and for depositing transistor gate dielectrics on 300 mm wafers with exceptional uniformity [96]. However, microoptical coatings are a technology that could particularly benefit from ALD. These coatings occur at mixed length scales, where micro- and nanoscale features exist alongside much larger, centimeter-scale dimensions. Here the self-limiting nature of ALD could allow uniform penetration into high-aspect ratio channels with small openings, along with an ability to uniformly coat large areas in spite of any temperature or gas flow gradients that may exist. Hollow waveguides, like those recently proposed or fabricated [97, 98], and etch-released optical microstructures are among the devices could benefit from the use of ALD optical coatings in such a way.

Some work has been done that involved sputtered or plasma-enhanced CVD (PECVD) coatings on the inside of relatively narrow tubes using highly customized equipment [99–102]. Specifically, Hagedorn et al. and Fujiyama have each used custom-sputtering apparatus to apply metal coatings to the inside of tubes with an inner diameter of 10 mm [99] or as low as 8 mm [100] and lengths up to 60 cm. Jansen and Krommenhoek [101] applied a special pulsed-plasma CVD technique to coat the inside of polyethylene terephthalate vials 10 cm long with 10 mm inner diameter, in a process that somewhat resembles ALD.

Noteworthy variations on the aforementioned nanoscale ALD capacitors for DRAM are a custom ALD reactor used to coat 7 $\mu$m diameter holes etched entirely through 310 $\mu$m thick silicon wafers [103], and the use of ALD to seal the surface of a porous dielectric with a few nanometers of silica to prevent subsequent ALD growth deeper in the pores [38]. It seems that the coating of microscale channels with much larger internal area has received little attention.

Here we present experimental results of thin films of alumina ($Al_2O_3$) and hafnia

($HfO_2$) deposited by ALD in relatively large high-aspect ratio structures. The inside of a 12 cm long capillary tube with a square cross section of 500 $\mu$m is coated with $Al_2O_3$, and "air wedge" structures are built and coated to precisely quantify film uniformity and quality. Finally, a Fabry-Pérot cavity is deposited in such a wedge to examine the repeatability of the process under these demanding conditions.

## 6.3 Experimental

$Al_2O_3$ and $HfO_2$ coatings were deposited using standard recipes at 250°C in a 200 mm diameter cross-flow ALD reactor (a Savannah S200 from Cambridge NanoTech). These are continuous-flow processes, with 20 sccm (standard cubic centimeters per minute) of nitrogen flow and continuous pumping resulting in a chamber pressure of roughly 1 Torr. The coating process consists of alternating pulses of precursor gas separated by 5 seconds of purging. As discussed in Ch. 4, the $Al_2O_3$ precursors are water and trimethylaluminum (TMA), and those for $HfO_2$ are water and tetrakis(dimethylamido)hafnium, $Hf(NMe_2)_4$, which is maintained at 75°C to achieve adequate vapor pressure. Each set of two precursor pulses and the associated purging is referred to as one "cycle", and growth rates can be linearly expressed as a thickness obtained per cycle.

### 6.3.1 Capillary tube

Our first experiment to test optical coatings inside microchannels was performed using a glass capillary tube 12 cm in length with an interior dimension defined by a square 500 $\mu$m opening, a 240:1 aspect ratio. The tube was placed inside the ALD chamber with its axis oriented along the gas flow direction and $Al_2O_3$ was deposited with 1000 cycles of TMA and $H_2O$. The internal coating thickness was investigated at the midpoint of the tube by sawing it with wafer dicing equipment and imaging it in cross section with a scanning electron microscope (SEM).

Fig. 6.1 shows cross-sectional SEM images at the midpoint of the coated tube. Fig. 6.1(d) indicates that the interior coating is on the order of 100 nm, near the expected 120 nm thickness for this nominally 0.12 nm/cycle process (§4.3.1 and 5.2.2). The result is encouraging, but the method is time-consuming, destructive, and not highly precise.

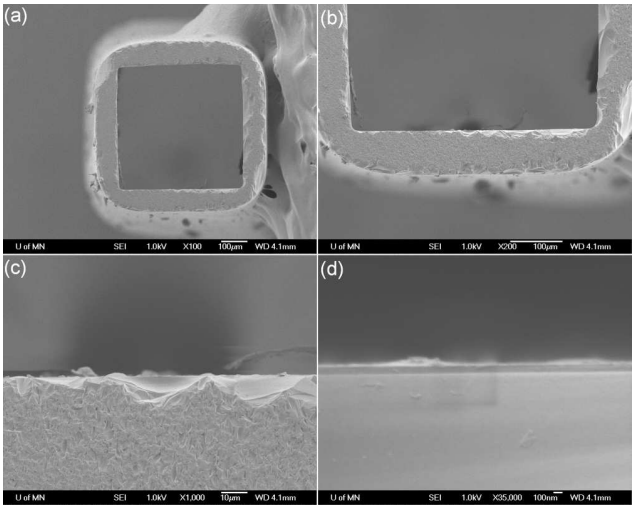


Figure 6.1: Cross-sectional SEM images at the midpoint of a 12 cm long capillary tube coated with 1000 cycles of ALD $Al_2O_3$. Images are at progressive levels of magnification; in (a) the 500 $\mu$m square cross section is visible, while (b) and (c) indicate the location of the final image in (d), where an inner coating of approximately 100 nm thickness can be seen.

### 6.3.2 Air wedge structure

In order to quantify the coating behavior in the presence of a variable air gap, structures with a wedge profile were created, as depicted in Fig. 6.2. Standard (100) silicon wafers were cleaved into nearly square pieces approximately 7 cm on a side. Two of these were centered in the ALD reactor with the polished surfaces facing the wedge interior, in contact along one edge and open at the opposite edge except for two small 1560 $\mu$m thick spacers. The process gas flow was perpendicular to this $\sim 1.3^\circ$ incline, presenting a variable cross section to the flow. The edge lengths of the actual structures varied between 62 and 70 mm due to the manual scribing process used to define the pieces, but the orientation was chosen to reduce the range to 66-70 mm in the incline direction. This 4 mm variation corresponds to a range of actual incline angles from 1.28–1.35°. Actual dimensions of all top and bottom pieces are given in Table 6.1. In this wedge structure we will use the term "aspect ratio" to refer to the ratio between penetration depth into the structure in the $x$ direction and the gap height. The parameter is included to give a sense of relative scale encountered by the vapor flux, not for direct comparison to the

aspect ratio of the capillary tube.

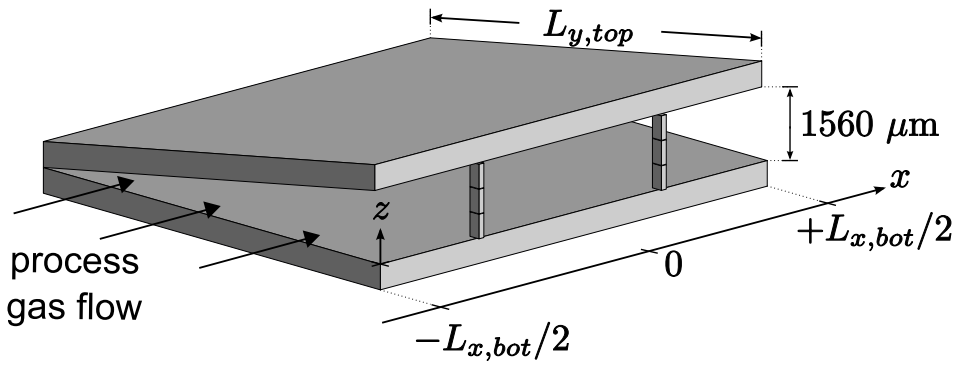


Figure 6.2: Diagram of an air wedge structure constructed from two cleaved silicon wafers separated at one edge by small spacers. The diagram is only partially to scale; the $z$ dimension is highly exaggerated relative to the $x$-$y$ plane. Actual $x$ and $y$ piece dimensions are in Table 6.1.

Single films of each material were deposited in air wedges by ALD, with 500 growth cycles used for each. The thickness and refractive index at 633 nm was measured using a variable-angle spectroscopic ellipsometer (VASE), specifically the V-VASE by J.A. Woollam with WVASE32 analysis software. These measurements were performed on the bottom piece of each wedge in two sets: at 5 mm intervals over a 60 mm $\times$ 60 mm region at the center of each sample, and at finer 2 mm $\times$ 1 mm resolution within 4 mm of the wedge vertex. The results are maps of thickness and refractive index as a function of position in the wedge, which is converted to approximate gap height by a simple trigonometric relation. The finite spot size of the equipment did not allow us to measure within about 1 mm of the vertex, which corresponds to a 22–24 $\mu$m minimum measurable gap height for the range of incline angles among the three wedges.

A six-layer optical cavity was deposited in a wedge structure consisting of layers $L$-$H$-$2L$-$H$-$L$-$H$, from bottom-to-top, where $L$ represents a low-index quarter-wave layer of $Al_2O_3$ and $H$ is a high-index quarter-wave layer of $HfO_2$. This structure yields a resonance at the arbitrarily chosen design wavelength $\lambda_0 \equiv 500$ nm. The proper thickness and associated number of ALD cycles needed for each layer in order to achieve the design resonance was determined using the relation $N_i = t_i/r_i$, where $N_i$ is the number of ALD cycles needed for layer $i$, $r_i$ is the deposition rate per cycle for that layer, and $t_i$ is the desired quarter-wave thickness given by $\lambda_0/(4n_i)$ where $n_i$ is refractive

Table 6.1: Dimensions of each wedge structure along centerlines.

| | $L_x$ (mm) | $L_y$ (mm) | wedge incline angle[a] | Max. measurable aspect ratio[b] |
|---|---|---|---|---|
| $Al_2O_3$ | | | | |
| Top | 63 | 70 | 1.28° | 1410:1 |
| Bottom | 67 | 70 | | |
| $HfO_2$ | | | | |
| Top | 62 | 66 | 1.35° | 1316:1 |
| Bottom | 66 | 66 | | |
| Six-layer cavity | | | | |
| Top | 65 | 70 | 1.31° | 1422:1 |
| Bottom | 68 | 68 | | |

[a]The incline angle $\theta$ for each wedge was calculated from the smaller of the two $L_y$ dimensions, using inverse tangent or inverse sine.

[b]The maximum measurable aspect ratio is defined as $L_{x,min}/(2z_{min})$, where $L_{x,min}$ is the $L_x$ of the smaller Si piece and $z_{min}$ is the gap height 1 mm from the wedge vertex by trigonometry, i.e. $z_{min} = (1\text{ mm})\sin\theta$.

index. The determination of each $t_i$ and $N_i$ was made prior to the single-film wedge characterization that is presented later in this paper. We had previously found the refractive index at 500 nm of similar films (Fig. 5.1 in §5.2.2) to be 1.655 for $Al_2O_3$ and 2.12 for $HfO_2$, so the desired quarter-wave thickness of the layers is $t_L = 75.5$ nm and $t_H = 59.0$ nm. In a simple experiment where we coated a silicon parallel-plate structure having a 530 $\mu$m gap with 1000 $Al_2O_3$ ALD cycles, the film thickness at the center was found to be 105.8 nm by a VASE measurement, or 0.1058 nm/cycle. The $HfO_2$ thickness per cycle was found to be 0.0855 nm/cycle based on a VASE measurement of a standard baseline coating where 725 ALD cycles yielded a 62 nm film thickness. Thus we arrive at the desired result for our 500 nm optical cavity design. The $L$ layers were set at $N_L = 714$ cycles, the $2L$ layer was $N_{2L} = 1427$ cycles, and $H$ layers were $N_H = 690$ cycles.

The reflectance of the resulting multilayer was measured at several locations along the bottom piece of this wedge structure, this time as a function of wavelength, usually 425–675 nm in 2 nm increments, with fixed $s$ polarization and a 15° angle of incidence

from normal. These spectral measurements were much more resource intensive, so we chose to measure along two slices. The first was a diagonal line going from $x = -33$ mm to $x = +30$ mm with $z$ increasing starting from 23 $\mu$m (1 mm from the vertex). The second was a line along $x = 0$. The $x$ and $z$ coordinates are defined in Fig. 6.2, and subsequent discussion of these two measurements will refer to the former as "the diagonal slice" and the latter as "the $x = 0$ slice". We chose to measure the diagonal slice because nearly the full range of observed $HfO_2$ thickness variation occurs along that diagonal, besides the small region very near the vertex. The $x = 0$ slice was chosen to observe what we felt would be worst-case conditions, furthest from all wedge openings. These results were compared to simulations of reflected intensity versus wavelength using the multilayer matrix method by Yeh [89] as described in Appendix C, with thickness and refractive index parameters as simulation inputs obtained from the single-film measurements presented in the next section.

## 6.4 Results and discussion

### 6.4.1 Single films in wedge

As expected from the capillary tube result, the $Al_2O_3$ process shows remarkable ability to coat within the air wedge structure, with only a 2.2 nm thickness variation across the measured area shown in Fig. 6.3. The thickness profile in this case seems insensitive to the flow direction, instead showing slightly decreasing thickness with increasing distance from any opening of the wedge. The overall thickness range of 54.0-56.2 nm represents a maximum variation from the peak of only $-3.9\%$. The results are summarized in Table 6.2.

500 ALD cycles of $HfO_2$ were deposited in an air wedge structure yielding the thickness profile shown in Fig. 6.4. There is significantly more variation than was seen in $Al_2O_3$. Thickness varies from the median value of 41.6 nm by +12.2 nm (+29%) and $-5.6$ nm ($-13\%$), thinnest at the corner furthest from the gas inlet ($x = +30$ mm) and near the wedge opening ($z = 1560$ $\mu$m), and thickest near the wedge vertex ($z = 24$ $\mu$m) and centered along the $x$ direction.

Refractive index profiles were also measured on each film at 633 nm. The $Al_2O_3$ film showed a refractive index of $1.645 \pm 0.005$, basically constant across the measured

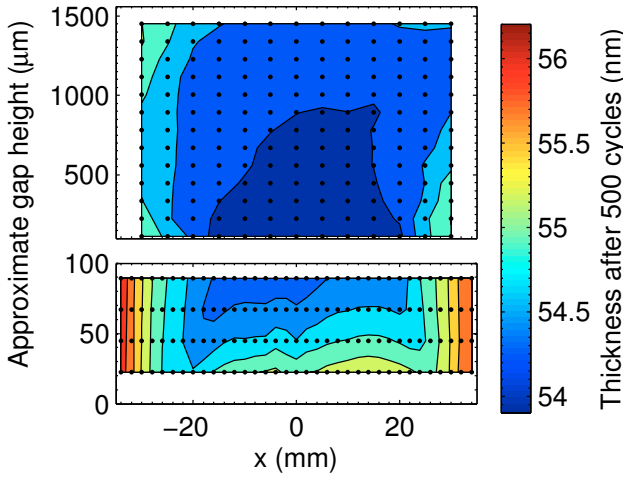


Figure 6.3: $Al_2O_3$ thickness profile when deposited in a wedge structure; black dots represent actual measurement locations. The data on the bottom set of axes are a separate measurement taken at much finer spatial resolution, shown on an exaggerated y-axis scale relative to the upper dataset.

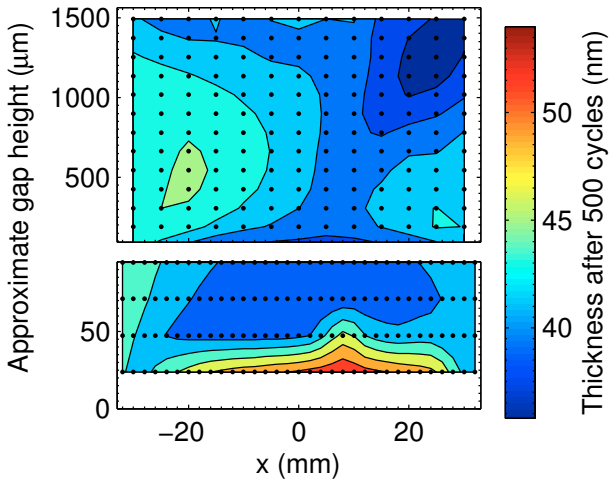


Figure 6.4: $HfO_2$ thickness profile when deposited by ALD in a wedge structure; black dots represent actual measurement locations. (The diagonal slice mentioned above and later applied to simulation of the optical cavity goes from the lower left to upper right of these data.)

area within experimental error during $x$–$y$ translation. It is quite remarkable that the $Al_2O_3$ refractive index did not vary with either the wedge cross section or distance along the gas flow direction. The $HfO_2$ film showed more variation and its refractive index is shown in Fig. 6.5. It was found to range between 2.02 and 2.07 around a median of 2.05, decreasing primarily with wedge gap. The lowest values are found closest to the wedge vertex, near $z = 0$. As mentioned above, the measurement did not include the 1 mm nearest the wedge vertex, so we could only measure down to a 24 $\mu$m gap height on this sample. There is also some variation in refractive index along the gas flow direction, especially near the edges. In general, it appears that the lowest refractive indices occur furthest from any opening of the wedge, i.e. at the highest aspect ratios. These results are summarized along with the $Al_2O_3$ data in Table 6.2.

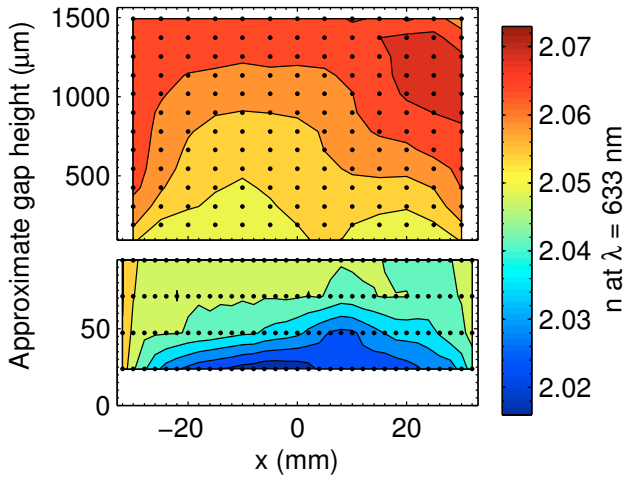


Figure 6.5: $HfO_2$ refractive index profile measured at 633 nm, obtained simultaneously with the thickness data in Fig. 6.4.

The refractive index data are particularly interesting because for a given transparent film there tends to be a correlation between density and refractive index. This relationship is often suggested, but has also been experimentally demonstrated on various thin films, e.g. in evaporated silicon dioxide thin films as shown by Scherer et al. [104] or in three oxide optical coatings deposited by several different techniques in [105]. Thus we speculate that the region of $HfO_2$ film near the vertex of the wedge has the lowest density. This could be explained by typical non-ideal ALD growth mechanisms, where

Table 6.2: Summary of single-film wedge results.

| | $Al_2O_3$ | | $HfO_2$ | |
|---|---|---|---|---|
| | thickness (nm) | $n$ at 633 nm | thickness (nm) | $n$ at 633 nm |
| Median | 54.5 | 1.645 | 41.6 | 2.05 |
| Min. | 54.0 | 1.64 | 36.0 | 2.02 |
| Max. | 56.2 | 1.65 | 53.8 | 2.07 |
| Range | 2.2 | $< 0.01$ | 17.8 | 0.05 |
| Per cycle[a]: | | | | |
| median | 0.109 | – | 0.083 | – |
| min. | 0.108 | – | 0.072 | – |
| max. | 0.112 | – | 0.108 | – |
| expected[b] | 0.1058 | – | 0.0855 | – |

[a]Each film was grown using 500 ALD cycles.

[b]The expected thicknesses per cycle are the previously measured values used in the Fabry-Pérot design as discussed in §6.3.2.

a lack of complete purging in some areas leads to more general CVD-like growth (§4.2). Since this type of CVD growth is not fully self-limiting it could lead to a film region with more voids, which has a reduced density and refractive index but also an increased thickness relative to the more ideal ALD regions.

### 6.4.2 Fabry-Pérot cavity

A six-layer optical cavity with a 500 nm design resonance was deposited inside an air wedge to check the repeatability of coating behavior inside such a structure from run-to-run and to demonstrate a practical optical coating. The sensitivity of the resonance position of a Fabry-Pérot cavity to deposited thickness has been successfully used in previous ALD optical studies to determine coating behavior (§4.4), albeit not inside a confined structure like this wedge. Reflected intensity versus wavelength was measured along the diagonal slice described above, yielding distinct resonance shown in Fig. 6.6. Actual $x$ location and gap height $z$ for each measurement is specified in the legend as $(x, z)$ in millimeters.

The reflectance was also simulated using the measured single-film refractive index

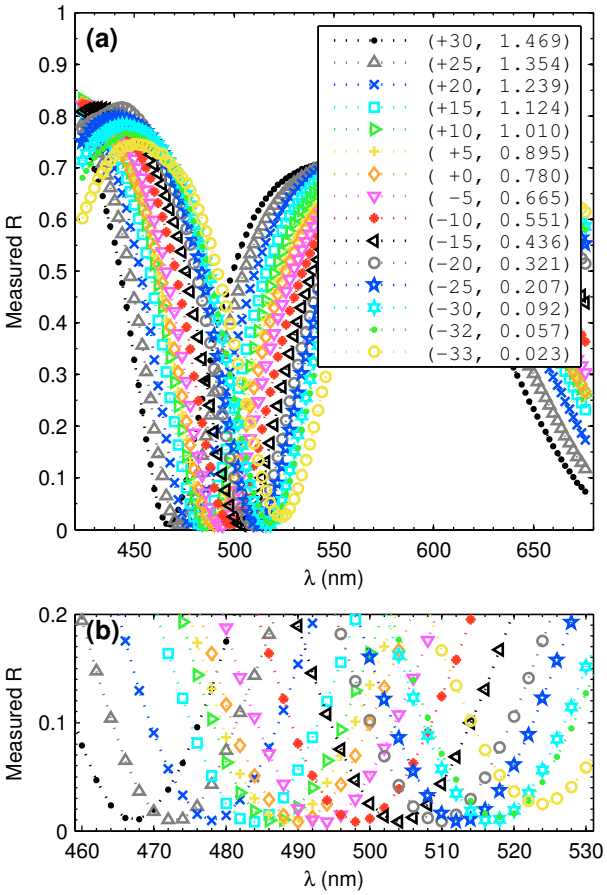


Figure 6.6: Intensity reflectance versus wavelength of the in-wedge optical cavity as measured along the diagonal slice. In (a) the spatial coordinates of each measurement are indicated in the form ($x$, $z$) where the units are millimeters, and a subset of the measurement is shown in (b). Dotted lines are shown for visual clarity only.

and thickness profiles in Figs. 6.3–6.5, with thickness scaled to the appropriate number of cycles used for each layer, e.g. a 714/500 ratio for the $L$ layers using Fig. 6.3 data. By doing this, we were essentially checking the hypothesis that these ALD processes inside the wedge structures are repeatable and approximately linear in thickness per cycle. Comparison of the measured reflectance minima to simulated predictions based on the single-film results are shown in Fig. 6.7. It should be noted that the gap height associated with simulated data is slightly offset from the measured gap height due to the slightly different incline angle of the various wedges indicated in Table 6.1; simulated data is referenced to $HfO_2$ gap height since that film had the most variation and is expected to be the source of most deviation observed in the optical cavity performance.

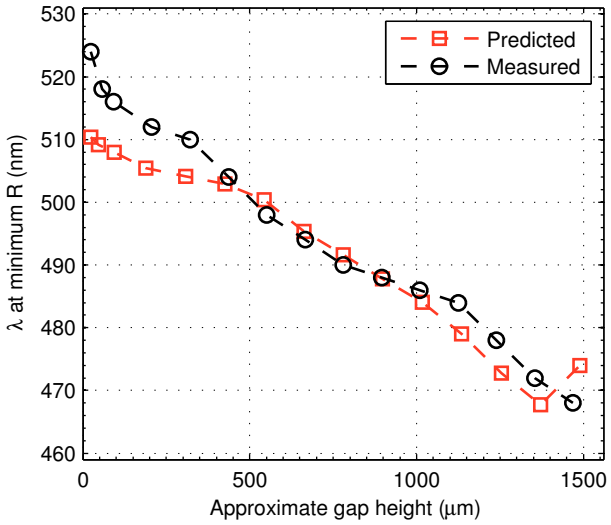


Figure 6.7: Comparison of measured R minima from Fig. 6.6 to simulated predictions based on single-film measurements along the same diagonal slice, with slight spatial offsets due the variation in wedge parameters indicated in Table 6.1.

There is reasonably close agreement between the predicted and measured data indicating that the microchannel ALD growth behavior is quite repeatable along the diagonal slice. There is a small but noticeable divergence from predicted behavior when less than about 400 $\mu$m gap height. The absolute performance along this slice is also quite good. The measured resonance only shifted by $-56$ nm overall, from 524 nm to 468 nm, over a lateral distance of 89 mm. This is a deviation from the 500 nm design

wavelength of only +4.8% and −6.4% in the presence of an air gap variation from 23 $\mu$m to 1.47 mm. This small absolute variation in resonance wavelength could be attributed in part to the extreme uniformity of the $Al_2O_3$ coating, but also to the trade-off between thickness and refractive index in the different growth regimes observed in the $HfO_2$ film. The more ideal ALD growth regime yields a film with the highest refractive index and self-limited thickness, whereas the regions with non-ideal CVD-like growth have slightly reduced refractive index but generally increased thickness.

The reflectance versus wavelength was also measured along the $x = 0$ slice, and a subset of those data are shown in Fig. 6.8(a). Comparison of the location of the observed relative minima to simulated predictions is presented in Fig. 6.8(b). The optical cavity behavior was less predictable along this slice, which is located further from any wedge opening than much of the diagonal slice and contains the highest aspect ratios as we have defined them. As indicated in Figs. 6.8(a) and (b), the cavity performs as expected down through $z = 780$ $\mu$m, with resonance staying near 500 nm and close to zero minimum reflectance. This point is very near the center of the wedge, having an aspect ratio of about 42:1 by our definition. Closer to the vertex, however, the resonance starts to broaden, it shifts much further in wavelength than expected, and the minimum reflectance increases, becoming a relative rather than an absolute minimum. The simulated curves are not shown in Fig. 6.8(a), but they predict resonance locations between 475 and 500 nm that maintain their width and near-zero minimum reflectance all the way to the vertex. In the simulations, the increase in $HfO_2$ thickness when approaching the vertex is mostly offset by the reduction in refractive index. Something else is occurring here besides the thickness and refractive index variation measured on the single films. Absorption and dispersion were not considered in the single-film measurements or in the simulations and could play a role, especially deep in the wedge where there is clearly some CVD-like behavior occurring in the $HfO_2$ films. Any increased absorption in the CVD-like regions would be expected to increase the losses in the cavity, broadening the resonance. Similarly, a shift in the location of absorption centers towards the visible region would cause a more rapid increase in $n$ than otherwise expected with decreasing wavelength, disrupting the designed cavity performance.

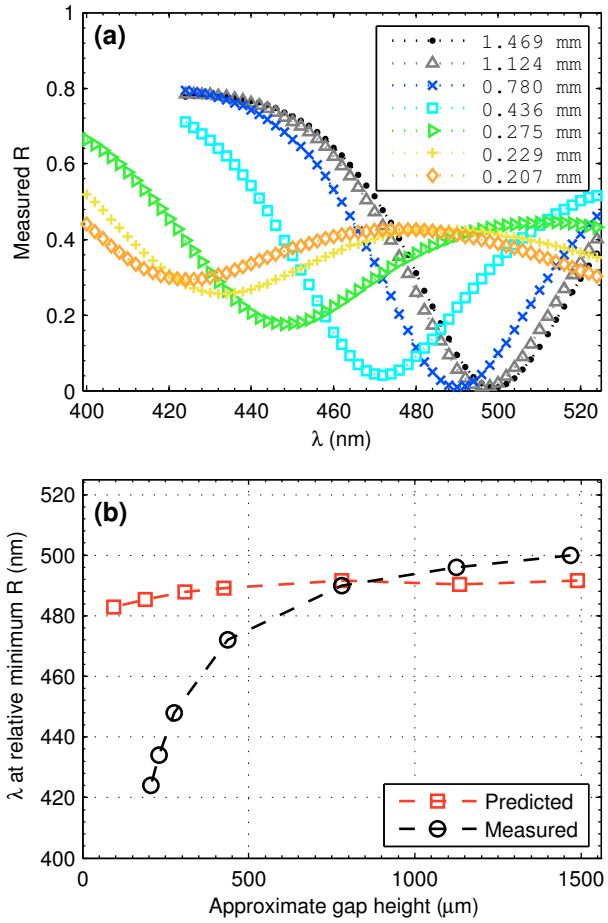


Figure 6.8: A subset of measured intensity reflectance versus wavelength along the $x = 0$ slice of the six-layer cavity. Measured data in (a) are at the gap heights indicated in the legend. The measured relative minima are shown in (b) along with simulated predictions based on the single-film measurements presented in Figs. 6.3-6.5.

## 6.5 Summary

We have demonstrated the use of ALD to coat the inside of microscale channels with $Al_2O_3$ and $HfO_2$. These films could be used as optical coatings for waveguides and microoptics, or more generally for improved environmental stability in a variety of applications. The agreement between design and experiment was extremely good over most aspect ratios, which we defined as the ratio between penetration depth and gap height.

ALD $Al_2O_3$ is particularly impressive, with an overall thickness range of only 4% and refractive index variation $< 0.01$, despite being measured over a 3800 $mm^2$ area in the presence of a gap variation from about 1.5 mm down to 22 $\mu$m. These uniformity values are more typical of what one would expect from a coating in the absence of a severely limited geometry, e.g. a fully exposed silicon wafer.

The $HfO_2$ variation and unexpected behavior of the optical cavity very near the wedge vertex for the highest aspect ratios indicates that modifications to the standard process are required to achieve the proper exposure and purging conditions needed to stay in the ALD growth regime everywhere inside the wedge. However, our ALD $HfO_2$ result should also be evaluated relative to the other non-ALD deposition techniques previously discussed, where coating inside a structure with one dimension on the order tens of micrometers was not even attempted, even with their use of highly customized equipment. In that context, our observed thickness variation from the median of +29% and −13% is quite good. Moreover, the ALD process tends to be partially self-correcting from an optical perspective because mild CVD-like growth behavior leads to increased thickness with decreased refractive index, reducing the impact on the effective optical path length.

The distinguishable peaks in our Fabry-Pérot results indicate that the use of resonance tracking in a simple cavity is a viable characterization technique for deposition in confined structures. This could be applied as a process characterization tool in less-ideal measurement situations, e.g. instead of or in addition to performing cross-sectional SEM on a coated capillary tube. In our case the cavity measurements also gave significant additional information about film quality near the vertex that was not observed in the single-film ellipsometric data.

# Chapter 7

# Thermal conductivity in ALD hafnia-alumina nanolaminates

## 7.1 Overview

Hafnia-alumina nanolaminates show improved smoothness and reduced crystallinity relative to pure hafnia in films formed by atomic layer deposition (ALD). However, typical nanolaminates also show significantly reduced cross-plane thermal conductivity due to the much larger interface density relative to continuous films. We find that the interface thermal resistance in hafnia/alumina nanolaminates is very low and does not dominate the film thermal conductivity, which is 1.0 to 1.2 W/(m K) at room temperature in 100 nm thin films regardless of the interface density. Measured films had a number of interfaces ranging from 2 to 40, equivalent to interface spacing varying from about 40 to 2 nm. The degree of crystallinity of these films appears to have a much larger effect on thermal conductivity than interface density. Cryogenic measurements to 30 K show reasonably good agreement with both the minimum thermal conductivity model for disordered solids and the diffuse mismatch model of interface resistance. We find that the films are quite smooth through a 400:5 ratio of hafnia to alumina in terms of ALD cycles, and the refractive index scales as expected with increasing alumina concentration.[1]

[1] The work in this chapter was submitted for journal publication in February 2011.

## 7.2 Motivation

As mentioned in §4.3, ultra-thin hafnium oxide films grown by atomic layer deposition (ALD) have been applied to gate dielectrics in field effect transistors, but at larger thicknesses they are partially crystalline and tend to have high surface roughness due to the variation in growth rate between crystallites and amorphous regions [47, 65]. These relatively higher thicknesses, near 100 nm, are particularly relevant to optical coating applications where crystallinity and roughness are detrimental [48]. Nanolaminate films consisting of occasional layers of alumina ($Al_2O_3$) to form hafnia-rich coatings have been demonstrated to substantially reduce the roughness and crystallinity [47], but the upper limit in the hafnia/alumina ratio remained somewhat vague. In a study of the nanosecond-scale laser-induced damage threshold (LIDT) of an ALD titania/alumina nanolaminate relative to a polycrystalline titania film indicated that the smooth, amorophous nanolaminate had at least twice the LIDT of the titania film [48].

A serious potential tradeoff that has been demonstrated in similar nanolaminates is reduced thermal conductivity due to the high interface density that scatters phonons [106]. While the reduced thermal conductivity is advantageous for thermal barrier coatings and thermoelectric materials, it can be detrimental to the performance of optical coatings, particularly in high-power laser systems.

We set out to characterize the thermal conductivity of these hafnia-based nanolaminates and also investigate the variation in refractive index, surface roughness, and crystallinity due to hafnia concentration above the 100:5 hafnia:alumina upper limit suggested by Hausmann and Gordon [47]. Maximizing the hafnia content should lead to larger effective refractive index and the smaller interface density to increased thermal conductivity, both advantages for optical coatings.

The differential $3\omega$ method is applied to measure the thermal conductivity of each thin film [107, 108]. The method is derived from the original $3\omega$ technique that was applied to bulk materials based on the frequency-dependent third-harmonic response of a heater wire deposited on a substrate [109]. It was later extended to measurements of dielectric films using the frequency-independent offset introduced by a thin film [110]. The thin-film technique required calculation of a substrate model for direct comparison to the measured data, which is sensitive to errors in assumed substrate thermal

properties, particularly the heat capacity, that can introduce an offset in the model indistinguishable from the thin film contribution. That original thin-film $3\omega$ technique has a lower limit of about 200 nm in practice [110, 111]. In contrast, the differential $3\omega$ method compares a particular multilayer film to a reference film where the film of interest is omitted, eliminating the need to apply handbook values for substrate properties. The potential tradeoff is that the differential result contains the uncertainty from two experimental measurements rather than one, but in practical cases with careful measurements this tends to be less than the combined uncertainty [107] in substrate thermal conductivity, heat capacity, and a geometrical factor usually referred to as $\eta$, especially when measuring very thin films or over a wide temperature range.

## 7.3 Experimental

Thin films containing alumina and hafnia were grown by atomic layer deposition in at 250°C, with processes described in §4.3.1 and 4.3.2. To reduce roughness and crystallinity, hafnia-rich nanolaminates with a varying periodic thickness of hafnia were grown by systematically changing the number of alternating-pulse growth cycles, based on the work of Hausmann and Gordon[47]. All films were deposited on pieces from B-doped, 1–10 ohm-cm, 100 mm diameter (100) silicon wafers.

Crystallinity was measured by x-ray diffraction (XRD) with monochromatic Cu $K_{\alpha 1}$ radiation at diffraction angles below the peaks from the silicon substrate. In XRD, the x-ray wavelength is on the order of interatomic spacing so that planes of atoms cause diffraction according to the Bragg condition, $m\lambda = 2d\sin\theta$, where $\lambda$ is wavelength, $d$ is crystal lattice spacing, and $\theta$ is the diffracted angle ($m$ is diffraction order). $K_\alpha$ x-rays from any atom are a result of electron transitions from a 2p to the 1s orbital. There are two possible $K_\alpha$ transition energies because electron spin and orbital angular momentum causes p orbitals to split into two discrete levels, having total angular quantum number of 1/2 or 3/2. The transitions from these two split levels are referred to as $K_{\alpha 2}$ and $K_{\alpha 1}$; the $K_{\alpha 1}$ photons are more numerous and slightly higher in energy, with a wavelength of 1.5406 Å in Cu [112].

Surface roughness was measured on some samples by scanning probe microscopy

Table 7.1: Parameters of the nanolaminates studied in this work. The number of alumina cycles per period was fixed at 5. The order of the layer deposition was hafnia then alumina so that a half period in the table below refers to a hafnia layer.

| Shorthand[a] | Hafnia cycles | Number of periods | Interface spacing[b] (nm) |
|---|---|---|---|
| NL400 | 400 | 2.25[c] | 40.0 |
| NL200 | 200 | 4.5 | 20.0 |
| NL100 | 100 | 10.5 | 10.0 |
| NL50 | 50 | 20.5 | 5.0 |
| NL20 | 20 | 40.5 | 2.0 |

[a] Used to refer to a particular design in figures and text.

[b] Interface spacing is given as the thickness of the hafnia layers based on 0.10 nm/cycle, which is one possible interpretation of the spacing between interfaces.

[c] To maintain overall thickness near 100 nm, this structure was finished with 200 hafnia cycles in the final half period rather than 400.

(SPM) using both the topological and phase-contrast images to get more detailed information about the morphology[113]. Estimates of roughness variation with nanolaminate parameters were obtained from variable-angle spectroscopic ellipsometery (VASE) on all samples, which also yielded film thickness and refractive index versus wavelength from 280 to 1080 nm. Spectroscopic ellipsometry measures two quantities, $\Psi$ and $\Delta$, at each wavelength, and these data can be numerically fit to a model to extract the desired parameters. $\Psi$ is the inverse tangent of the measured intensity ratio of $p$- and $s$-polarized components of light reflected from the sample, and $\Delta$ is the measured phase difference between those components.[2] To maximize the sensitivity of the measurement to film parameters, the angle of incidence was set near each film's Brewster angle, which is where the corresponding refraction angle into the film does not allow the $p$-polarized component to reflect from the top surface. Instead it is completely transmitted through

[2] The $s$ and $p$ components are perpendicular to and parallel to the plane of incidence, respectively; see Fig. C.2 in Appendix C.

the film and reflects from the film-substrate interface instead, which has a large impact on the relative phase of the $p$ component. The Brewster angle is very sensitive to wavelength because of dispersion in the film, causing $\Delta$ to be very sensitive to wavelength as well. This improves the sensitivity of the fitting algorithm to the 5 model parameters, which were thickness, roughness, and three Cauchy dispersion parameters, all of which will be explained in more detail in the results section (§7.5.2).

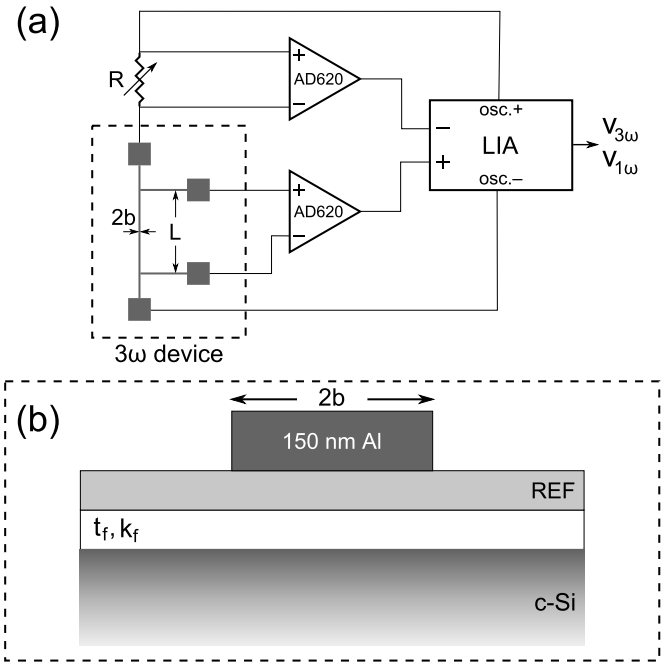


Figure 7.1: A diagram of the 3$\omega$ experimental setup is shown in (a) indicating connections of the device to a series potentiometer, unity-gain AD620 instrumentation amplifiers, and the LIA. In (b), a cross-sectional view of a test structure on single-crystal Si indicates the film of interest having thickness $t_f$ and thermal conductivity $k_f$ along with a reference film (REF) and aluminum heater-thermometer; the reference samples for the differential method have the primary film omitted.

The differential 3$\omega$ measurements were performed as depicted in Fig. 7.1. They were based on a nominally identical 100 nm ALD alumina reference film applied to all samples. Each sample had a heater and thermometer formed by electron-beam evaporation of 150 nm of aluminum onto the reference alumina, patterned by photolithography and etched to an 8.0 $\mu$m wide strip with 1.00 mm length defined by the voltage readout

lines in a four-wire resistance measurement configuration. The thickness of the Al line was chosen near the minimum allowable for wire-bonding of connections to reduce effects due to its heat capacity[107], and the 8.0 $\mu$m width was sufficiently wide relative to the 0.1 $\mu$m film thickness to approximate one-dimensional heat flow. The 100 nm films of interest were assembled into test samples in three batches, each batch having its own co-deposited reference sample. ALD alumina was chosen as the reference film due to its excellent electrical insulation properties, extreme uniformity across the deposition area for consistency within each batch[94], and run-to-run repeatability for consistency between batches. The Al temperature coefficient of resistance (TCR) is a very important parameter in this method, and it was measured on every device with two heat/cool cycles from 295–335 K, where its behavior is highly linear. There was some variation in TCR between the three batches but the variation within each batch was smaller than the estimated TCR measurement precision, so the mean TCR was applied to the calculations for each batch as recorded in Table 7.2.

As shown in Fig. 7.1(a), a lock-in amplifier (LIA) was used as the sinusoidal input voltage source and as the detection instrument. The very large input heating signal was subtracted from the signal sent to the LIA by a series potentiometer and two identical Analog Devices AD620 instrumentation amplifiers. The readout system is conceptually similar to the one described in detail by Cahill in his original report[109], except that our LIA is digital and can internally select an arbitrary harmonic of the driving signal. The measured $3\omega$ data are shown in Fig. 7.2. These were converted to experimental $\Delta T$ data using the expression [109, 114]

$$\Delta T = \frac{2v_{3\omega}}{\alpha v_{1\omega}}, \tag{7.1}$$

where $\alpha$ is the measured TCR of the Al and the $v$ terms are RMS magnitudes of the in-phase third-harmonic and fundamental voltages. As an additional check of the data validity, the slope of the measured $\Delta T$ versus $\ln(\omega)$ can be used to directly estimate the thermal conductivity of the substrate [109], which we found to be consistently near the tabulated 300 K values for silicon [115–117] of 142 to 156 W/(m K). These values are strongly dependent on temperature in that range and also vary with dopant levels, making this an imprecise verification.

To get a better sense of the role of the hafnia-alumina interfaces in the observed

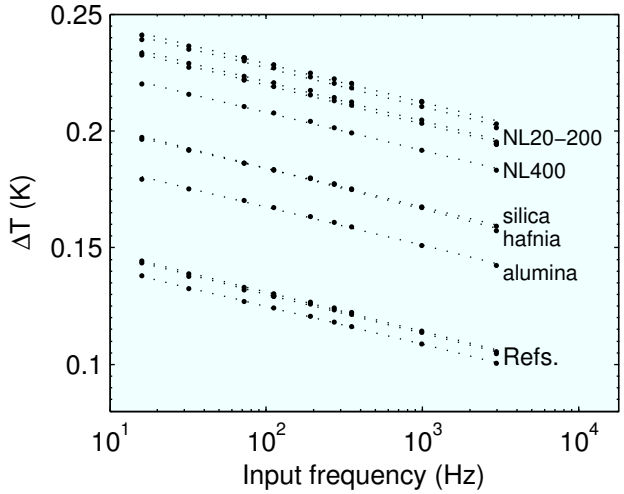


Figure 7.2: Measured data from the lock-in amplifier for all of the 100 nm film samples along with the three reference samples, converted to temperature units using Eq. (7.1). The offset relative to the respective reference film is proportional to film thermal conductivity, and the indicated logarithmic linear fits yield estimates of substrate thermal conductivity based on the original $3\omega$ method. Hafnia and silica nearly overlap as do most of the nanolaminates.

thermal conductivity, cryogenic differential $3\omega$ measurements were performed on the nanolaminate film with highest interface density (NL20) down to the minimum temperature allowed by the TCR of the Al resistor, which was around 30 K. This allows more detailed comparison to interface model predictions. We also measured the pure hafnia film down to 30 K to compare the results to the minimum thermal conductivity model for disordered crystals and amorphous materials [118, 119] as has been done for thick sputtered oxides [111]. The TCR in these experiments was measured while slowly heating each sample between the measurement temperatures and comparing the resistance of the device to a calibrated Si diode mounted in the cryostat. The TCR is quite nonlinear over this large range so the derivative of $R$ versus $T$ was used, with some smoothing, to estimate the TCR near each measurement temperature.

## 7.4 Theory

### 7.4.1 Minimum thermal conductivity model

To describe some of the film results we will apply a minimum thermal conductivity model for amorphous solids developed by Cahill and Pohl[118] and also applied successfully to disordered crystals[119].

$$k_{min} = \left(\frac{\pi}{6}\right)^{1/3} k_B n^{2/3} \sum_m c_m \left(\frac{T}{\Theta_m}\right)^2 \int_0^{\Theta_m/T} \frac{x^3 e^x}{(e^x-1)^2} dx \tag{7.2}$$

$T$ is temperature, $n$ is the atomic number density, $c_m$ is the acoustic velocity of phonon mode $m$, and $\Theta_m$ is the Debye temperature for that mode. The integral can be numerically solved for a given Debye temperature ratio. This model of localized oscillators is applicable when the phonon mean free path is very small, true near room temperature and reasonably accurate down to about 50 K, below which the longer wavelength phonons become more dominant. A primary assumption in the model is that the coupled oscillators have arbitrary phase; this is not true in crystals but does apply to fully disordered materials and is the main reason for its applicability as an effective lower limit to thermal conductivity.

### 7.4.2 Interface thermal conductivity

We will also discuss the physics of interface behavior as applicable to the nanolaminate films. A note about the definition of interfaces in these films is important before exploring the detailed behavior. The nanolaminate films consist of alternating layers of hafnia of various thickness with fixed ultra-thin layers of alumina. We consider the thickness of these alumina layers to be sufficiently thin such that they serve as a single interface per period, rather than counting one interface at each hafnia-alumina or alumina-hafnia transition for a total of two per period.

Above about 20 K in solids, the diffuse mismatch model (DMM) is a reasonably accurate description of phonon behavior across an interface[120]. The primary assumption of the DMM is that all phonons are incoherently scattered at the interface; as Swartz and Pohl put it simply in Ref. [120], "each phonon forgets where it came from". Like its lower-temperature cousin the acoustic mismatch model (AMM), the DMM is an elastic

scattering model, which means that the energy (frequency) of a scattered phonon does not change during the scattering process. Inelastic processes do occur in real materials and will increase the interface conductance above that predicted by the model, but the effect is not significant in most solid material combinations[120]. This is because the phonon densities of states of most solids are similar enough that phonons from one material can scatter easily enough into a state at the same energy on the other side of the interface. When the material mismatch is great—Swartz and Pohl give lead-diamond as an example interface—then inelastic scattering is dominant and the DMM will greatly underestimate the interface conductivity. Material mismatch in this context can be quantified by the ratio of Debye temperatures of each material, which is equivalent to the ratio of sound velocities (see §2.2.3 in Ch. 2, particularly Eq. 2.9).

We apply the usual simplifying assumption that hafnia and alumina behave as Debye solids in this temperature range, with the phonon density of states per unit volume $D_m(\omega)$ of each mode $m$ (one longitudinal and two transverse) described by[3] a sound velocity $c_m$:

$$D_m(\omega) = \frac{\omega^2}{2\pi^2 c_m^3}. \tag{7.3}$$

Debye density of states was also presented as Eq. 2.7 in the chapter discussing thermal expansion. The number of phonons in each mode at a given frequency at a specific temperature, $N_m(\omega, T)$, is the product of the density of states and the Bose-Einstein occupancy factor, yielding

$$N_m(\omega, T) = \frac{D_m(\omega)}{\exp(\frac{\hbar\omega}{k_B T}) - 1}, \tag{7.4}$$

where $k_B$ is the Boltzmann constant.

Under this Debye simplification, both the AMM and DMM are described by the same equation for thermal boundary conductivity[120] based on the acoustic velocities $c_m$, integrated transmission probabilities $\Gamma_m$, and phonon number densities $N_m$ for each of the three acoustic phonon modes $m$:

$$h_{\mathrm{Bd}} = \frac{1}{2} \sum_m c_{1,m} \Gamma_{1,m} \int_0^{\omega_1^D} \hbar\omega \frac{dN_{1,m}(\omega, T)}{dT} d\omega \tag{7.5}$$

[3] For example, see [4], p. 112

The only parameter that differs between the two models is $\Gamma$, the integrated transmission probability, which is where the specular versus diffuse scattering assumptions manifest. In the DMM, $\Gamma$ does not depend on incident angle; it is a ratio of acoustic velocities on each side of the interface for each of three acoustic modes:

$$\Gamma_1^{\mathrm{DMM}} = \frac{1}{2} \frac{\sum\limits_m c_{2,m}^{-2}}{\sum\limits_m c_{1,m}^{-2} + \sum\limits_m c_{2,m}^{-2}}. \tag{7.6}$$

Applying Eq. (7.6) and the temperature derivative of Eq. (7.4) to Eq. (7.5) yields the following DMM boundary conductivity expression that we compared to our measured data:

$$h_{Bd} = \frac{1}{8\pi^2 k_B T^2} \frac{\left(\sum\limits_m c_{1,m}^{-2}\right)\left(\sum\limits_m c_{2,m}^{-2}\right)}{\sum\limits_m c_{1,m}^{-2} + \sum\limits_m c_{2,m}^{-2}} \int_0^{\omega_1^D} \frac{\hbar^2 \omega^4 d\omega \exp(\frac{\hbar\omega}{k_B T})}{\left[\exp(\frac{\hbar\omega}{k_B T}) - 1\right]^2} \tag{7.7}$$

The model inputs are thus temperature $T$, acoustic velocities for the longitudinal and two transverse modes for both materials $c_{i,L}$ and $c_{i,t}$, and the lowest of the two materials' Debye cutoff frequency, $\omega_1^D$. In the low-temperature limit, Eq. (7.7) has a simpler, $T^3$, dependence just like Debye heat capacity, but in this case the full expression was numerically integrated to cover the entire temperature range of interest. The $\hbar$ constants were left in the integral to balance the $\omega$ terms since $\omega^D$ is roughly $10^{13}$ rad/s. Note the similarity of this integral to that in Eq. (7.2) since both are based on Debye models.

### 7.4.3 Differential 3$\omega$ model

The model for extracting film thermal conductivity from the differential 3$\omega$ method is [107]

$$k_f = \frac{t_f}{WL} \frac{1}{(\Delta T/P)_f - (\Delta T/P)_0} \tag{7.8}$$

The subscripts $f$ and 0 represent the film and reference samples, the measured temperature differences $\Delta T$ are given by Eq. (7.1), $W$ and $L$ are the width and length of the metal lines, $t_f$ is the film thickness, and $P$ is the average input power calculated from $v_{1\omega}^2/R$ where $R$ is device electrical resistance at $P$ measured using the balanced potentiometer. Equation 7.8 is derived from a simple one-dimensional heat flow model where the reference film(s) and the film of interest both contribute a thermal conductance of

$G_i = WLk_i/t_i$, and these $G_i$ terms are added inversely. It is important to note that the contribution of the reference film(s) only cancel out to yield Eq. (7.8) if both samples have the same width $W$ and length $L$ and see the same input power $P$. This matching of area and power input per unit length causes a $W_0L_0k_0/t_0$ reference-film term to cancel, as well as a more complicated thermal diffusivity term from the $3\omega$ substrate model [109]. Further details on the derivation of Eq. (7.8) and its assumptions are found in Appendix D.1.

## 7.5 Results and discussion

### 7.5.1 Crystallinity

The x-ray diffraction results are presented in Fig. 7.3. A broad amorphous peak with maximum at $2\theta = 32^\circ$ is found in all nanolaminates, but they have none of the many crystalline monoclinic hafnia peaks that are evident in the pure hafnia film. This is a significant result, since previous work on similar nanolaminate films suggested that x-ray-observable crystallinity appeared with hafnia layers greater than 10 nm (100 ALD cycles) [47]. We see no such crystallinity through 40 nm or 400 ALD cycles per period, potentially significant for applications where alumina content should be minimized. This is not entirely unprecedented according to the previous ALD hafnia reports reviewed in Table 4.1. Specifically, an ALD hafnia film 33 nm thick (330 ALD cycles) was found to be amorphous by XRD while a nominally identical film at twice that thickness was partially crystalline [65], and similar ALD hafnia films 20–30 nm thick were also x-ray amorphous [60].

The percentage of crystallinity of the pure hafnia film can be determined by the area under all of the crystalline peaks relative to the area under the much broader amorphous "peaks". This determination is sensitive to the choice of background or baseline shape. Choosing a baseline shape matching the shape of the measured bare silicon data yields a hafnia crystallinity of about 14%. An alternative is to choose a linear background that follows general slope of the measured pattern without resulting in a negative number of counts for any value of $2\theta$. This background yielded a crystallinity of 32%, which is larger because the linear background cut off some regions previously included in the amorphous area. The actual percent crystallinity likely falls somewhere between these

two values.

Also noteworthy is a peak near $2\theta = 11°$ in NL20 that corresponds to a lattice spacing of about 0.8 nm using the Bragg condition and x-ray wavelength. That measured spacing is similar to the nanolaminate period of the film, since it has 40 periods of hafnia-alumina pairs formed from 20 ALD cycles of hafnia and 5 ALD cycles of alumina. Based on the 0.1 nm/cycle deposition rate each period is expected to be about 2.0 nm of hafnia and 0.5 nm of alumina. Wide-angle XRD is not a particularly sensitive way to measure the spacing of such a film structure since this diffraction angle is relatively small, but it is indicative of order in the film near the expected scale. The other films have at least twice the interface spacing (and at most half the number of interfaces) as NL20, so any diffraction from them would likely occur at $2\theta \lesssim 5°$ (and lower in intensity by at least half).

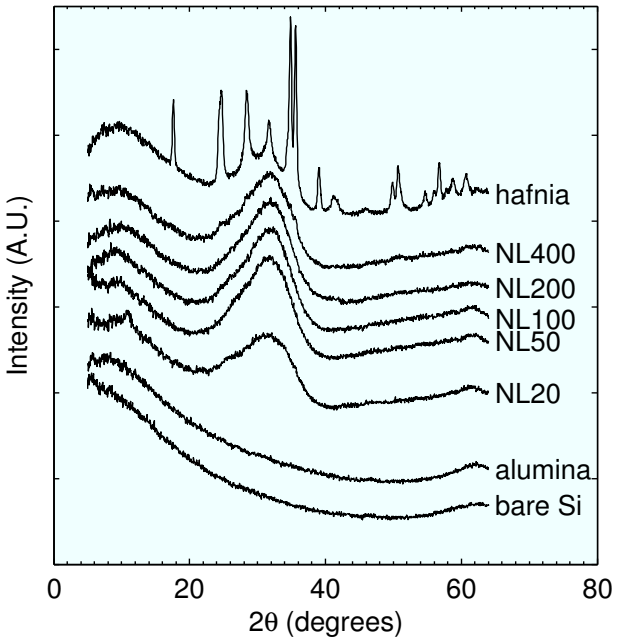


Figure 7.3: X-ray diffraction results showing the amorphous nature of alumina and all of the nanolaminate films, which are labeled as defined in Table 7.1 with the number of hafnia ALD cycles per period. The hafnia film has over twenty monoclinic crystalline peaks and is about 14–32% crystalline based on the relative area under amorphous and crystalline regions.

### 7.5.2 Surface roughness and refractive index

The scanning probe microscopy data for the hafnia in Fig. 7.4 and the NL100 film in Fig. 7.5 show that the expected large drop in surface roughness with incorporation of alumina does indeed occur, corroborating the results of Hausmann and Gordon[47]. The alumina film and the bare substrate were also measured and all four results are summarized in Fig. 7.6.

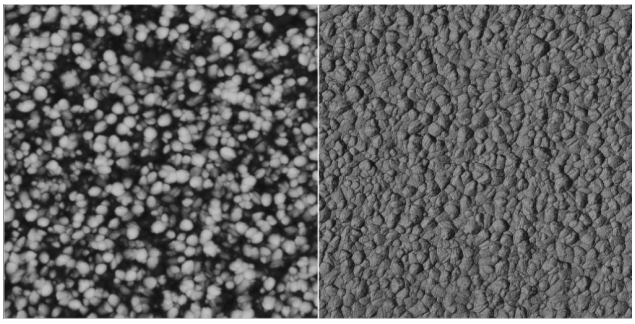

Figure 7.4: SPM results on a ∼100 nm thick hafnia film, indicating a large surface roughness of 6.3 nm root mean square (RMS). The topographic image on the left has a pixel range of 0–30 nm and covers a 2 $\mu$m × 2 $\mu$m area. The phase-contrast image on the right covers the same lateral area, giving a clearer look at the boundaries between surface features.

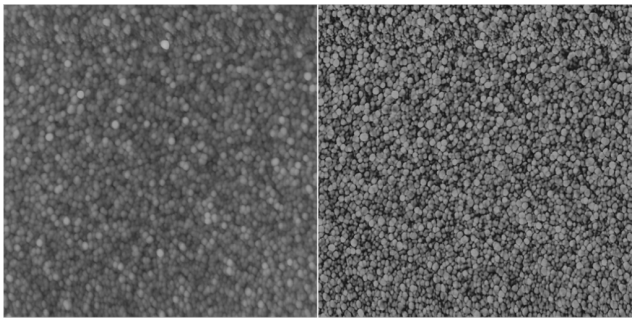

Figure 7.5: SPM results on NL100, a ∼100 nm thick hafnia nanolaminate film having 100 layers (∼10 nm) of hafnia per period. The topographic (left) and phase-contrast (right) images correspond to those in Fig. 7.4 except the pixel range is reduced by half (to 0–15 nm) in this case. This nanolaminate film is smooth, 0.75 nm RMS, and lacks the well-defined regions on the surface.

We are particularly interested in the optical behavior of these films, considering

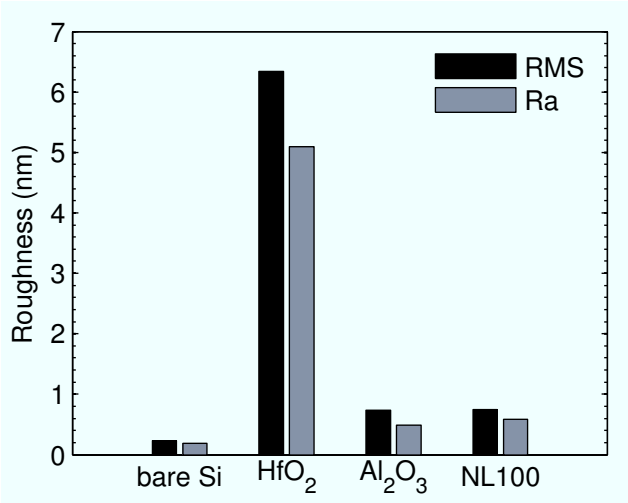


Figure 7.6: A summary of SPM surface roughness results, with RMS and arithmetic average (Ra) roughness measures shown for the bare Si, hafnia from Fig. 7.4, alumina, and NL100 from Fig. 7.5. This nanolaminate film is as smooth as the alumina, and much more suitable for optical applications than the partially crystalline hafnia.

the demonstrated high laser-induced damage threshold of hafnia[121], in-part due to its relatively high bandgap energy[81]. With alumina interlayers on the order of only 0.5 nm, much shorter than visible wavelengths, we expect each nanolaminate to behave as an effective refractive index based on relative alumina content. The spectroscopic ellipsometry data were fit to a Cauchy model for each film with thickness along with three free parameters representing dispersion.

$$n(\lambda) = A + \frac{B}{\lambda^2} + \frac{C}{\lambda^4} \tag{7.9}$$

This three-parameter model fit the ellipsometric data very well for the nanolaminate films, with refractive index versus wavelength maintaining a shape like the hafnia film. The expected reduction in refractive index with increasing alumina composition was observed, as shown in Fig. 7.7 for some selected wavelengths.

Since each ellipsometric dataset contained 81 wavelength steps from 280 nm to 1080 nm, each wavelength having both a $\Psi$ and a $\Delta$ datapoint representing reflected polarization amplitude and phase ratios, the solution to each system was highly over-constrained, allowing an additional layer to be included in the fit to represent surface roughness. This effective-medium approximation (EMA) layer was set to match the

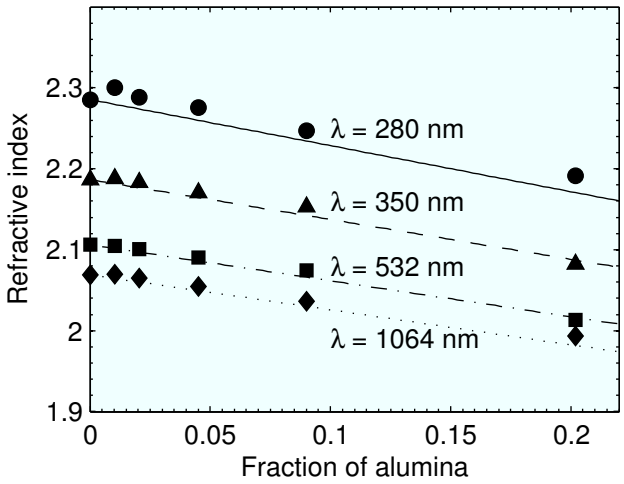


Figure 7.7: Hafnia and nanolaminate refractive index versus composition for selected wavelengths along with a model for each based on a linear combination of measured hafnia and alumina refractive indices. Wavelengths shown are 280 nm (circles), 350 nm (triangles), 532 nm (squares), and 1064 nm (diamonds).

fitted film dispersion according to Eq. (7.9) but also consist of 50% voids having a refractive index of 1. The thickness of the EMA layer was allowed to vary along with the other four parameters, and a reasonable solution was obtained in each case except in the most extreme nanolaminate (NL20). A solution to the model was reached for NL20 as well, but there was a large amount of correlation between the parameters, especially thickness and EMA roughness. The correlation means, for example, that if thickness was fixed at some value, then the model fit would yield a certain EMA roughness value, but if thickness was increased then it would yield a different, lower, EMA roughness value. None of the other films showed this behavior. The shorter-wavelength portion of the model was particularly sensitive to the EMA roughness fit for surface roughness of this magnitude and was especially helpful in the fitting. Roughness is plotted as a function of alumina concentration in Fig. 7.8, showing good agreement with the subset of SPM results from Fig. 7.6. NL20 is omitted from the plot. We see that even the most moderate nanolaminate, NL400, has fairly low roughness relative to the pure hafnia film. This is expected considering that we found all of our nanolaminate films to be x-ray amorphous, but it was surprising considering the previously reported maximum

of roughly 100 hafnia layers per period for smooth, amorphous films[47]. That work did suggest a strong temperature dependence of crystallinity in the vicinity of 250°C, so it is plausible that moderate temperature variations or measurement uncertainty at various points in the deposition chamber could significantly affect these film properties.

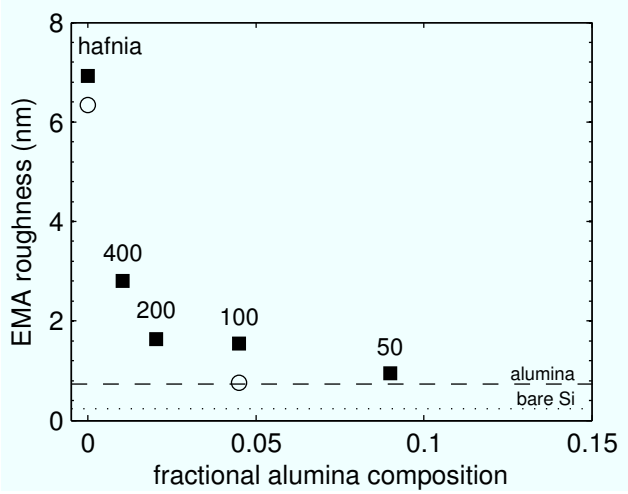


Figure 7.8: Roughness values of all films obtained from VASE measurements as a function of alumina composition. Roughness here is the thickness of a 50% void effective-medium approximation (EMA) layer included in the fits to ellipsometric data. Open circles and dashed and dotted lines show RMS values from SPM data in Fig. 7.6 for comparison.

### 7.5.3 Room-temperature thermal conductivity

Thermally grown silica films were included to verify the accuracy of the measurement technique. A 109.5 nm thick $SiO_2$ film had a measured thermal conductivity of 1.61 W/(m K) at room temperature, and a 66.5 nm film was measured to be 1.49 W/(m K). These are slightly above but reasonably close to reported values[111]. All room-temperature results are shown in Table 7.2, along with important parameters. The alumina film has a relatively high thermal conductivity, and the partially crystalline hafnia film has a thermal conductivity 50–60% larger than that of the nanolaminates.

The variation of thermal conductivity among the nanolaminates contains important information about the behavior of the constituent films. We can immediately see from Table 7.2 that the nanolaminates all have very similar thermal conductivity. These are

Table 7.2: Measured thermal conductivity at room temperature.

| Film | $k_f$[a] (W/m K) | $t_f$[b] (nm) | meas. batch[c] |
|---|---|---|---|
| th-$SiO_2$ | 1.61 | 109.6 | 1 |
| th-$SiO_2$ | 1.49 | 66.5 | 2 |
| alumina | 2.59 | 107.7 | 2 |
| hafnia | 1.72 | 101.1 | 2 |
| NL400 | 1.17 | 103.1 | 3 |
| NL200 | 1.07 | 110.1 | 3 |
| NL100 | 1.02 | 110.2 | 2 |
| NL50 | 1.07 | 119.7 | 3 |
| NL20 | 1.04 | 105.6 | 3 |

[a] Absolute uncertainty in measured $k_f$ is nonlinear and is estimated to be between ±25% and ±50%; this is discussed in detail in Appendix D.2.

[b] Film thickness is excluding the EMA roughness layer included in ellipsometric model for hafnia films.

[c]Room-temperature TCR for Eq. (7.1) applied by batch mean. Batch 1 TCR 0.2864 ± 0.0025 %/K, batch 2 TCR 0.2586 ± 0.0043 %/K, and batch 3 TCR 0.2655 ± 0.0034 %/K; ± values represent measured range within each batch.

plotted versus interface density in Fig. 7.9 along with several models. The first case is that the hafnia and alumina layers behave as a series combination of individual layer thermal resistance, with zero interfacial resistance. The dependence is then on alumina concentration rather than interface density, not matching the observed behavior. Another possibility is that each hafnia layer is in series with the interface resistance, with two free parameters of intrinsic (amorphous) hafnia thermal conductivity and interface conductivity that are fit to the data using least squares, resulting in 1.10 W/(m K) and 1.5 GW/($m^2$ K). The former value is quite reasonable based on these data and previously reported hafnia film results[64, 111], but the latter is about two times higher than what is expected for any solid-solid interfaces[122]. This indicates that the interface conductivity is on the same order as the individual layer thermal conductivity, at the

low end of the detectable range using this technique. A final model variant is also plotted in Fig. 7.9, using the minimum thermal conductivity model result of 1.04 W/(m K) from Eq. (7.2) for the hafnia layers and the DMM result of 500 MW/(m$^2$ K) from Eq. (7.7) calculated for these interfaces. We used estimated acoustic velocities for alumina and hafnia[4] and Debye temperatures based on atomic number density calculated from reported mass densities for a fully-dense amorphous alumina film [111] of 3.51 g/cm$^3$ and for ALD hafnia [69] of 9.23 g/cm$^3$.

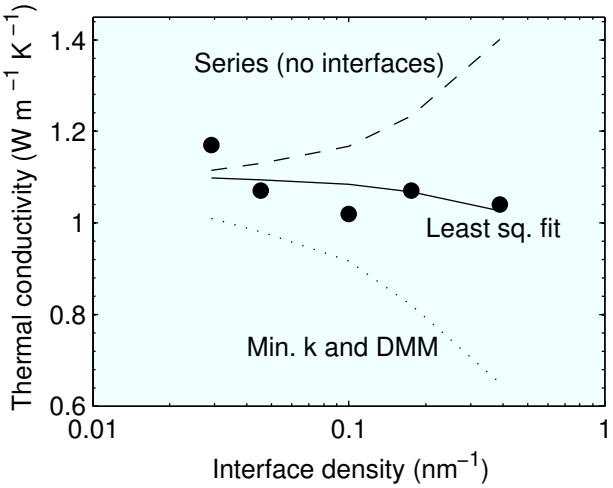


Figure 7.9: The measured thermal conductivity of the nanolaminate films are shown versus interface density along with several models. The dashed line is a model with no interface resistance, the solid line is a least squares fit to hafnia intrinsic thermal conductivity (1.10 W/m K) and interface conductance (1.5 GW/m$^2$K), and the dotted line is the same model but with parameters calculated from the minimum thermal conductivity model (Eq. (7.2)) and DMM (Eq. (7.7)).

### 7.5.4 Cryogenic thermal conductivity

The measured 30–300 K data for the pure hafnia film along with NL20, the nanolaminate film with hafnia layers approximately 2 nm thick, are shown in Fig. 7.10 along with minimum thermal conductivity and diffuse mismatch models calculated from Eqs. 7.2 and 7.7 using the aforementioned parameters.

[4] We applied values from Ref. [111]: $c_l$ = 8.8 and $c_t$ = 5.74 km/s for alumina and $c_l$ = 4.8 and $c_t$ = 3.3 km/s for hafnia

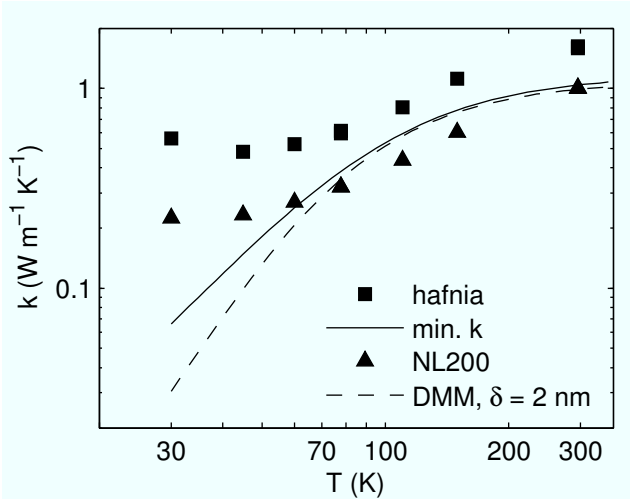


Figure 7.10: The measured thermal conductivity of the hafnia film (squares) and NL20 (triangles) are shown with two models based on Debye parameters of acoustic velocities and atomic number density; a minimum thermal conductivity model for hafnia (solid line), and a diffuse mismatch model for alumina-hafnia interfaces assuming interface-dominated conductivity with 2 nm interface spacing (dashed line).

The hafnia film is significantly above the minimum thermal conductivity model and comparable to the previous result for sputtered hafnia [111]. An additional mechanism possibly at work in the partially crystalline hafnia film at lower temperatures is the increase in thermal conductivity of crystalline solids as temperature decreases due to increased phonon mean free path. The slight increase at 30 K may be indicative of this crystalline behavior, or it may simply be due to the greater uncertainty as the TCR of Al approaches zero, becoming more difficult to measure accurately and also reducing the $3\omega$ signal.

At temperatures above about 70 K, the NL20 film could be described equally well by the fully amorphous hafnia model or an interface-dominated diffuse mismatch model. This result could be interpreted in several different ways. The very thin alumina interlayers may simply be serving their intended role of disrupting all hafnia crystallite growth, yielding phonon behavior like a fully amorphous hafnia. Alternatively, the hafnia-alumina interfaces could be completely dominating the thermal conductivity, or the interfaces and amorphous hafnia film regions could be contributing equally. These three possibilities can not be easily separated because the thermal conductance of each

8.0 $\mu$m $\times$ 1.0 mm hafnia-alumina DMM interface seems to be very similar to the thermal conductance of a 2 nm thick region of amorphous hafnia; both are very near 4.1 W/K at 300 K.

The divergence of the nanolaminate data from both models below about 50 K in Fig. 7.10 is expected because the dominant phonon wavelength in real materials is inversely proportional to temperature. The consequence for each model is similar but for different reasons. The minimum thermal conductivity model (solid line) is based on local oscillators, but as the dominant phonon wavelength increases with decreasing temperature the localized model becomes less accurate, predicting an excessive decrease in thermal conductivity. In the case of interface resistance based on the DMM (dashed line), the model itself is quite accurate through this range[120], but the assumption of interface-dominated thermal resistance in this nanolaminate breaks down, also due to the longer wavelength phonons, so that the effective thermal conductivity can no longer reasonably be described as $k \approx \delta G_{DMM}$ where $\delta$ is interface spacing.

Measurements below 30 K would be useful to observe the transition from diffuse to specular scattering expected near 20 K in most solids and described by the acoustic mismatch model [120], but below 30 K the temperature-dependence of the aluminum resistor quickly becomes too close to zero, diminishing the $3\omega$ signal below the measurement threshold. Similar issues have been observed in $3\omega$ measurements using silver resistors[119] and are a difficult limitation of the $3\omega$ method.

## 7.6 Summary

We have shown that the thermal boundary resistance within hafnia-alumina nanolaminates deposited by ALD is small enough that it does not significantly reduce the effective film thermal conductivity, an important finding for its use in high-power optical coatings. The crystallinity and surface roughness of relatively thick ALD hafnia films can be reduced substantially by forming very modest nanolaminate structures with alumina, with ALD-cycle-based hafnia:alumina ratios of at least 400:5. The partially crystalline hafnia does have enhanced thermal conductivity relative to fully amorphous films, as demonstrated by comparison to the measured nanolaminate results or to the minimum thermal conductivity model for amorphous or disordered crystals.

# Chapter 8

# Conclusion

This dissertation expands the body of knowledge on the usage of atomic layer deposition (ALD) for optical coatings, especially when thermal effects or complex geometry are significant design factors. Entirely new work was presented in Chs. 5–7 after reviewing relevant concepts in the field in Chs. 2–4.

In Ch. 2, the underlying physics of solid-state thermal expansion was described in some detail. The theory comes from the study of phonons and heat capacity, where thermal expansion is related to heat capacity by a Grüneisen parameter. The temperature dependence was discussed relative to the Debye temperature as is the established convention both experimentally and in theoretical derivations. The Debye temperature can be well above or below room temperature depending on the material. The thermal expansion coefficient or CTE is mostly constant above a material's Debye temperature, goes to zero at very low temperatures, and behaves in a complicated fashion in between.

A review of thin film thermal expansion modeling and coefficient of thermal expansion (CTE) measurement was presented in Ch. 3. The two broad categories are based on either measuring thickness changes or curvature changes with temperature. The thickness-based techniques rely on some form of x-ray reflectivity to measure thickness, and, after removing the effect of substrate confinement, out-of-plane CTE is the result. Limitations include difficulty measuring low CTE values and limited applicability of out-of-plane CTE values to real-world thin film problems. In the curvature-based techniques, the curvature data are converted to film stress, then to strain, which is then mapped to a CTE value. Model inputs are substrate and film thickness and biaxial

modulus, and substrate CTE. In the case of the double-substrate technique the second substrate CTE takes the place of film biaxial modulus.

Chapter 4 reviewed the key characteristics of atomic layer deposition (ALD) along with specific information on alumina and hafnia processes and others relevant to optics. The advantages of properly optimized ALD processes are precise and accurate control of thickness at a scale $< 1\,\text{nm}$, conformal coating of high-aspect-ratio structures, and lower deposition temperatures than general CVD. Growth temperature (within the "ALD window") is a key parameter that will affect the impurity content of the film and its morphology. ALD has two primary drawbacks, slow growth rate and high roughness in thicker films, and these can be particularly detrimental in optical coatings. Faster growth can be done using processes like "rapid vapor deposition" of silica, and roughness can be reduced by forming nanolaminates.

The brand new work in this dissertation was presented in the final three chapters. In Ch. 5, a mechanical design technique for optical coatings was shown that simultaneously controls thermal deformation and optical reflectivity. The method only requires knowledge of refractive index, CTE, and elastic modulus of single layers of each film. The precision and accuracy of ALD allowed for *a priori* or "open-loop" design, with multilayer behavior matching design on the first iteration. We applied this method to the thermally invariant mirror problem through simulations of the same films but on a commercially available thin glass substrate, Schott D263, which has a more appropriate CTE. The change in substrate introduces some uncertainty such that film biaxial moduli must be assumed based on nanoindentation measurements, but other properties needed for simulations were obtained from actual measurements. The results suggest that the D263 glass/ALD alumina/ALD hafnia system is very promising if thermally invariant mirrors are needed for a given application.

In Ch. 6, we demonstrated the use of ALD to coat the inside of microscale channels with alumina and hafnia, quantified using a wedge structure with gap varying from about $20\,\mu\text{m}$ to $1500\,\mu\text{m}$. Alumina is particularly impressive, with an overall thickness range of only 4% and refractive index variation $< 0.01$. These uniformity values are more typical of what one would expect from a coating in the absence of any geometrical confinement. The larger variation in hafnia indicates that modifications to that process are required to achieve the proper exposure and purging conditions needed to stay in the ALD growth

regime everywhere inside the wedge. But the behavior was quite consistent, and still very impressive relative to the other non-ALD deposition techniques that had been attempted by others. The ALD process tends to be self-correcting from an optical perspective because mild CVD-like growth behavior leads to increased thickness with decreased refractive index, reducing the impact on the effective optical path length. Also, the multilayer Fabry-Pérot film measurements gave significant additional information about film quality near the vertex that was not observed in the single-film ellipsometric data.

Finally, in Ch. 7, we demonstrated the lower limits of alumina incorporation into hafnia-rich nanolaminates while still achieving smooth films. A hafnia:alumina ALD-cycle-ratio of at least 400:5 is acceptable, which is a thickness ratio of about 40 nm:0.5 nm. That film has a refractive index that is almost identical to pure hafnia, and refractive index scales smoothly downward with increased alumina concentration. Moreover, thermal conductivity measurements demonstrated that interface density has little effect beyond making the nanolaminates behave as amorphous hafnia films. These are very important findings for their potential use in high-power optical coatings, where hafnia is often the high-refractive-index material of choice.

# Bibliography


[1] L. B. Freund, J. A. Floro, and E. Chason. Extensions of the stoney formula for substrate curvature to configurations with thin substrates or large deformations. *Applied Physics Letters*, 74(14):1987–9, 1999.

[2] Y. Okada and Y. Tokumaru. Precise determination of lattice parameter and thermal expansion coefficient of silicon between 300 and 1500K. *Journal of Applied Physics*, 56(2):314–20, 1984.

[3] Neil W. Ashcroft and N. David Mermin. *Solid State Physics*. Holt, Rinehart and Winston, USA, 1976.

[4] Charles Kittel and Paul McEuen. *Introduction to Solid State Physics*. Wiley, USA, 8th edition, 2005.

[5] T. R. Ravindran, Akhilesh K. Arora, and T. A. Mary. Anharmonicity and negative thermal expansion in zirconium tungstate. *Physical Review B*, 67(6):064301, February 2003.

[6] E. Grüneisen. Zustand des festen körpers. In H. Geiger and Karl Scheel, editors, *Handbuch der Physik*, volume 10, pages 1–59. Julius Springer, Berlin, 1926.

[7] F. R. Drymiotis, H. Ledbetter, J. B. Betts, T. Kimura, J. C. Lashley, A. Migliori, A. P. Ramirez, G. R. Kowach, and J. Van Duijn. Monocrystal elastic constants of the Negative-Thermal-Expansion compound zirconium tungstate ($ZrW_2O_8$). *Physical Review Letters*, 93(2):025502, July 2004.

[8] J.G. Collins and G.K. White. Thermal expansion of solids. *Progress in Low Temperature Physics*, 4:450–479, 1964.

[9] T.H.K. Barron, J.G. Collins, and G.K. White. Thermal expansion of solids at low temperatures. *Advances in Physics*, 29(4):609, July 1980.

[10] G. D. Barrera, J. A. O. Bruno, T. H. K. Barron, and N. L. Allan. Negative thermal expansion. *Journal of Physics: Condensed Matter*, 17(4):R217–R252, 2005.

[11] T. A. Mary, J. S. O. Evans, T. Vogt, and A. W. Sleight. Negative thermal expansion from 0.3 to 1050 kelvin in $ZrW_2O_8$. *Science*, 272(5258):90–92, April 1996.

[12] Charles Martinek and F. A. Hummel. Linear thermal expansion of three tungstates. *Journal of the American Ceramic Society*, 51(4):227–228, 1968.

[13] Kai Wang and R. R. Reeber. Mode grüneisen parameters and negative thermal expansion of cubic $ZrW_2O_8$ and $ZrMo_2O_8$. *Applied Physics Letters*, 76(16):2203–4, April 2000.

[14] Michael S. Sutton and Joseph J. Talghader. Zirconium tungstate ($ZrW_2O_8$)-based micromachined negative thermal-expansion thin films. *Journal of Microelectromechanical Systems*, 13(4):688–95, August 2004.

[15] HF Liu, XN Cheng, and ZP Zhang. Preparation and properties of negative thermal expansion zirconium tungstate thin films deposited by radio frequency magnetron sputtering. *Physica Status Solidi B*, 245(11):2509–2513, November 2008.

[16] G. Gerald Stoney. The tension of metallic films deposited by electrolysis. *Proceedings of the Royal Society of London*, 82:172–175, January 1909.

[17] S. Timoshenko. Analysis of bi-metal thermostats. *Journal of the Optical Society of America*, 11(3):233–255, 1925.

[18] M. Vasudevan and W. Johnson. On multi-metal thermostats. *Applied Scientific Research, Section B*, 9(6):420–430, 1963.

[19] F. Jansen, M. A. Machonkin, N. Palmieri, and D. Kuhman. Thermomechanical properties of amorphous silicon and nonstoichiometric silicon oxide films. *Journal of Applied Physics*, 62(12):4732–6, December 1987.

[20] J. Thurn and M. P. Hughey. Evaluation of film biaxial modulus and coefficient of thermal expansion from thermoelastic film stress measurements. *Journal of Applied Physics*, 95(12):7892–7, 2004.

[21] Jr. M. M. de Lima, R. G. Lacerda, J. Vilcarromero, and F. C. Marques. Coefficient of thermal expansion and elastic modulus of thin films. *Journal of Applied Physics*, 86(9):4936–42, November 1999.

[22] W. Fang, H. C. Tsai, and C. Y. Lo. Determining thermal expansion coefficients of thin films using micromachined cantilevers. *Sensors and Actuators A: Physical*, A77(1):21–7, 1999.

[23] J. H. Zhao, Y. Du, M. Morgen, and P. S. Ho. Simultaneous measurement of young's modulus, poisson ratio, and coefficient of thermal expansion of thin films on substrates. *Journal of Applied Physics*, 87(3):1575–7, February 2000.

[24] E. Chason and T. M Mayer. Thin film and surface characterization by specular x-ray reflectivity. *Critical Reviews in Solid State and Materials Sciences*, 22(1):1–67, 1997.

[25] M. Bhattacharya, M. Mukherjee, M. K. Sanyal, T. Geue, J. Grenzer, and U. Pietsch. Energy dispersive x-ray reflectivity technique to study thermal properties of polymer films. *Journal of Applied Physics*, 94(5):2882–7, September 2003.

[26] T. Suzuki, I. Sugiura, S. Sato, and T. Nakamura. Thermal expansion coefficients of nano-clustering silica (NCS) films measured by x-ray reflectivity and substrate curvature methods. *Japanese Journal of Applied Physics, Part 2 (Letters)*, 43(5A):614–16, 2004.

[27] W. L. Wu and H. C. Liou. Study of ultra-thin hydrogen silsesquioxane films using x-ray reflectivity. *Thin Solid Films*, 312(1-2):73–7, January 1998.

[28] M. Mukherjee, M. Bhattacharya, M. K. Sanyal, T. Geue, J. Grenzer, and U. Pietsch. Reversible negative thermal expansion of polymer films. *Physical Review E: Statistical, Nonlinear, and Soft Matter Physics*, 66(6):61801, 2002.

[29] W. A. Brantley. Calculated elastic constants for stress problems associated with semiconductor devices. *Journal of Applied Physics*, 44(1):534–5, 1973.

[30] Zhe chuan Feng and Hong du Liu. Generalized formula for curvature radius and layer stresses caused by thermal strain in semiconductor multilayer structures. *Journal of Applied Physics*, 54(1):83–85, January 1983.

[31] C. H. Hsueh. Thermal stresses in elastic multilayer systems. *Thin Solid Films*, 418(2):182–188, October 2002.

[32] W. C. Oliver and G. M. Pharr. Measurement of hardness and elastic modulus by instrumented indentation: Advances in understanding and refinements to methodology. *Journal of Materials Research*, 19(1):3–20, January 2004.

[33] Riikka L. Puurunen. Surface chemistry of atomic layer deposition: A case study for the trimethylaluminum/water process. *Journal of Applied Physics*, 97(12):121301–52, June 2005.

[34] Tuomo Suntola and Jorma Antson. Method for producing compound thin films, November 1977.

[35] Dennis Hausmann, Jill Becker, Shenglong Wang, and Roy G. Gordon. Rapid vapor deposition of highly conformal silica nanolaminates. *Science*, 298(5592):402–6, 2002.

[36] Dennis M. Hausmann, Esther Kim, Jill Becker, and Roy G. Gordon. Atomic layer deposition of hafnium and zirconium oxides using metal amide precursors. *Chemistry of Materials*, 14(10):4350–8, 2002.

[37] J. Kim, H. Hong, K. Oh, and C. Lee. Properties including step coverage of TiN thin films prepared by atomic layer deposition. *Applied Surface Science*, 210(3-4):231–239, April 2003.

[38] Philippe de Rouffignac, Zhengwen Li, and Roy G. Gordon. Sealing porous low-k dielectrics with silica. *Electrochemical and Solid-State Letters*, 7(12):G306–G308, December 2004.

[39] Jian Jim Wang, Xuegong Deng, Ron Varghese, Anguel Nikolov, Paul Sciortino, Feng Liu, Lei Chen, and Xiaoming Liu. Filling high aspect-ratio nano-structures by atomic layer deposition and its applications in nano-optic devices and integrations. *J. Vac. Sci. Technol. B*, 23:3209–3213, November 2005.

[40] Philippe de Rouffignac, Andrew P. Yousef, Kyoung H. Kim, and Roy G. Gordon. ALD of scandium oxide from scandium tris(N,N'-diisopropylacetamidinate) and water. *Electrochemical and Solid-State Letters*, 9(6):F45–F48, June 2006.

[41] Jaakko Niinistö, Kaupo Kukli, Maarit Kariniemi, Mikko Ritala, Markku Leskelä, Nicolas Blasco, Audrey Pinchart, Christophe Lachaud, Nadia Laaroussi, Ziyun Wang, and Christian Dussarrat. Novel mixed alkylamido-cyclopentadienyl precursors for ALD of $ZrO_2$ thin films. *Journal of Materials Chemistry*, 18(43):5243–5247, 2008.

[42] Kai-Erik Elers, Tom Blomberg, Marko Peussa, Brad Aitchison, Suvi Haukka, and Steven Marcus. Film uniformity in atomic layer deposition. *Chemical Vapor Deposition*, 12(1):13–24, 2006.

[43] G. S. Higashi and C. G. Fleming. Sequential surface chemical reaction limited growth of high quality $Al_2O_3$ dielectrics. *Applied Physics Letters*, 55(19):1963–1965, November 1989.

[44] P. F. Carcia, R. S. McLean, and M. H. Reilly. Permeation measurements and modeling of highly defective $Al_2O_3$ thin films grown by atomic layer deposition on polymers. *Applied Physics Letters*, 97(22):221901, 2010.

[45] Riikka L. Puurunen, Marina Lindblad, Andew Root, and A. Outi I. Krause. Successive reactions of gaseous trimethylaluminium and ammonia on porous alumina. *Physical Chemistry Chemical Physics*, 3(6):1093–1102, 2001.

[46] Y. Kim, S. M. Lee, C. S. Park, S. I. Lee, and M. Y. Lee. Substrate dependence on the optical properties of $Al_2O_3$ films grown by atomic layer deposition. *Applied Physics Letters*, 71(25):3604–3606, December 1997.

[47] Dennis M. Hausmann and Roy G. Gordon. Surface morphology and crystallinity control in the atomic layer deposition (ALD) of hafnium and zirconium oxide thin films. *Journal of Crystal Growth*, 249(1-2):251–261, February 2003.

[48] Shin ichi Zaitsu, Shinji Motokoshi, Takahisa Jitsuno, Masahiro Nakatsuka, and Tatsuhiko Yamanaka. Laser damage properties of optical coatings with nanoscale layers grown by atomic layer deposition. *Japanese Journal of Applied Physics*, 43:1034–1035, 2004.

[49] Sangho S. Kim, Nicholas T. Gabriel, Woo-Bin Song, and Joseph J. Talghader. Encapsulation of low-refractive-index $SiO_2$ nanorods by $Al_2O_3$ with atomic layer deposition. *Optics Express*, 15(24):16285–16291, 2007.

[50] J. Meyer, D. Schneidenbach, T. Winkler, S. Hamwi, T. Weimann, P. Hinze, S. Ammermann, H.-H. Johannes, T. Riedl, and W. Kowalsky. Reliable thin film encapsulation for organic light emitting diodes grown by low-temperature atomic layer deposition. *Applied Physics Letters*, 94(23):233305–3, June 2009.

[51] W. C. Sun, W. L. Chang, C. H. Chen, C. H. Du, T. Y. Wang, T. Wang, and C. W. Lan. High efficiency silicon solar cells with bilayer passivation structure. *Electrochemical and Solid-State Letters*, 12(10):H388–H391, October 2009.

[52] Isaac D. Scott, Yoon Seok Jung, Andrew S. Cavanagh, Yanfa Yan, Anne C. Dillon, Steven M. George, and Se-Hee Lee. Ultrathin coatings on Nano-$LiCoO_2$ for Li-Ion vehicular applications. *Nano Letters*, in press:10.1021/nl1030198, December 2010.

[53] T. M. Mayer, J. W. Elam, S. M. George, P. G. Kotula, and R. S. Goeke. Atomic-layer deposition of wear-resistant coatings for microelectromechanical devices. *Applied Physics Letters*, 82(17):2883–2885, April 2003.

[54] Yanhang Zhang, Martin L. Dunn, Ken Gall, Jeffrey W. Elam, and Steven M. George. Suppression of inelastic deformation of nanocoated thin film microstructures. *Journal of Applied Physics*, 95(12):8216–8225, June 2004.

[55] Front end processes. In *International Technology Roadmap for Semiconductors*. ITRS, http://www.itrs.net/Links/2009ITRS/Home2009.htm, 2009.

[56] Glen D. Wilk, Robert M. Wallace, and J. M. Anthony. High-$\kappa$ gate dielectrics: Current status and materials properties considerations. *Journal of Applied Physics*, 89(10):5243–5275, 2001.

[57] Jill S. Becker. *Atomic Layer Deposition of Metal Oxide and Nitride Thin Films*. PhD thesis, Harvard University, Cambridge, Massachusetts, December 2002.

[58] Anand Deshpande, Ronald Inman, Gregory Jursich, and Christos Takoudis. Atomic layer deposition and characterization of hafnium oxide grown on silicon from tetrakis(diethylamino)hafnium and water vapor. *Journal of Vacuum Science and Technology A*, 22(5):2035–2040, 2004.

[59] E. P. Gusev, H. Shang, M. Copel, M. Gribelyuk, C. D'Emic, P. Kozlowski, and T. Zabel. Microstructure and thermal stability of HfO2 gate dielectric deposited on ge(100). *Applied Physics Letters*, 85(12):2334–6, 2004.

[60] Kaupo Kukli, Tero Pilvi, Mikko Ritala, Timo Sajavaara, Jun Lu, and Markku Leskelä. Atomic layer deposition of hafnium dioxide thin films from hafnium tetrakis(dimethylamide) and water. *Thin Solid Films*, 491(1-2):328–338, November 2005.

[61] E. P. Gusev, V. Narayanan, and M. M. Frank. Advanced high-$\kappa$ dielectric stacks with polySi and metal gates: Recent progress and current challenges. *IBM Journal of Research and Development*, 50(5):387–410, 2006.

[62] Lijuan Zhong, Weston L. Daniel, Zhihong Zhang, Stephen A. Campbell, and Wayne L. Gladfelter. Atomic layer deposition, characterization, and dielectric properties of HfO2/SiO2 nanolaminates and comparisons with their homogeneous mixtures. *Chemical Vapor Deposition*, 12(2-3):143–150, 2006.

[63] K. Mistry, C. Allen, C. Auth, B. Beattie, D. Bergstrom, M. Bost, M. Brazier, M. Buehler, A. Cappellani, R. Chau, C.-H. Choi, G. Ding, K. Fischer, T. Ghani, R. Grover, W. Han, D. Hanken, M. Hattendorf, J. He, J. Hicks, R. Huessner, D. Ingerly, P. Jain, R. James, L. Jong, S. Joshi, C. Kenyon, K. Kuhn, K. Lee, H. Liu, J. Maiz, B. Mclntyre, P. Moon, J. Neirynck, S. Pae, C. Parker, D. Parsons, C. Prasad, L. Pipes, M. Prince, P. Ranade, T. Reynolds, J. Sandford, L. Shifren,

J. Sebastian, J. Seiple, D. Simon, S. Sivakumar, P. Smith, C. Thomas, T. Troeger, P. Vandervoorn, S. Williams, and K. Zawadzki. A 45nm logic technology with High-k+Metal gate transistors, strained silicon, 9 cu interconnect layers, 193nm dry patterning, and 100% pb-free packaging. In *Technical Digest of IEEE International Electron Device Meeting (IEDM)*, pages 247–250, Washington, DC, USA, 2007. IEEE.

[64] M.A. Panzer, M. Shandalov, J.A. Rowlette, Y. Oshima, Yi Wei Chen, P.C. McIntyre, and K.E. Goodson. Thermal properties of ultrathin hafnium oxide gate dielectric films. *Electron Device Letters, IEEE*, 30(12):1269–1271, 2009.

[65] Justin C. Hackley and Theodosia Gougousi. Properties of atomic layer deposited $HfO_2$ thin films. *Thin Solid Films*, 517(24):6576–6583, October 2009.

[66] Johan Swerts, Nick Peys, Laura Nyns, Annelies Delabie, Alexis Franquet, Jan Willem Maes, Sven Van Elshocht, and Stefan De Gendt. Impact of precursor chemistry and process conditions on the scalability of ALD $HfO_2$ gate dielectrics. *Journal of The Electrochemical Society*, 157(1):G26–G31, January 2010.

[67] H. Kattelus, M. Ylilammi, J. Salmi, T. Ranta-aho, E. Nykänen, and I. Suni. Electrical properties of tantalum based composite oxide films. In *Materials Research Society Symposium Proceedings*, volume 284, pages 511–516. Materials Research Society, 1993.

[68] Mikko Ritala, Markku Leskelä, Lauri Niinistö, Thomas Prohaska, Gernot Friedbacher, and Manfred Grasserbauer. Development of crystallinity and morphology in hafnium dioxide thin films grown by atomic layer epitaxy. *Thin Solid Films*, 250(1-2):72–80, October 1994.

[69] Dennis M. Hausmann. *Atomic layer deposition of metal oxide thin films.* PhD thesis, Harvard University, Cambridge, Massachusetts, July 2002.

[70] Jason W. Klaus, Ofer Sneh, and Steven M. George. Growth of $SiO_2$ at room temperature with the use of catalyzed sequential Half-Reactions. *Science*, 278(5345):1934–1936, December 1997.

[71] Lijuan Zhong, Fang Chen, Stephen A. Campbell, and Wayne L. Gladfelter. Nanolaminates of zirconia and silica using atomic layer deposition. *Chemistry of Materials*, 16(6):1098–1103, 2004.

[72] B. B. Burton, M. P. Boleslawski, A. T. Desombre, and S. M. George. Rapid $SiO_2$ atomic layer deposition using tris(tert-pentoxy)silanol. *Chemistry of Materials*, 20(22):7031–7043, October 2008.

[73] Diana Riihelä, Mikko Ritala, Raija Matero, and Markku Leskelä. Introducing atomic layer epitaxy for the deposition of optical thin films. *Thin Solid Films*, 289(1-2):250–255, 1996.

[74] Ronald R. Willey. Using fence post designs to speed the atomic layer deposition of optical thin films. *Applied Optics*, 47(13):C9–C12, May 2008.

[75] Xiaohua Du, Kevin Zhang, Kathy Holland, Thomas Tombler, and Martin Moskovits. Chemical corrosion protection of optical components using atomic layer deposition. *Applied Optics*, 48(33):6470–6474, November 2009.

[76] Shin ichi Zaitsu, Takahisa Jitsuno, Masahiro Nakatsuka, Tatsuhiko Yamanaka, and Shinji Motokoshi. Optical thin films consisting of nanoscale laminated layers. *Applied Physics Letters*, 80(14):2442, 2002.

[77] M. Ylilammi and T. Ranta-aho. Metal fluoride thin films prepared by atomic layer deposition. *Journal of The Electrochemical Society*, 141(5):1278–1284, May 1994.

[78] Tero Pilvi, Timo Hatanpaa, Esa Puukilainen, Kai Arstila, Martin Bischoff, Ute Kaiser, Norbert Kaiser, Markku Leskela, and Mikko Ritala. Study of a novel ALD process for depositing $MgF_2$ thin films. *Journal of Materials Chemistry*, 17(48):5077–5083, 2007.

[79] Tero Pilvi, Kai Arstila, Markku Leskelä, and Mikko Ritala. Novel ALD process for depositing $CaF_2$ thin films. *Chemistry of Materials*, 19(14):3387–3392, 2007.

[80] Tero Pilvi, Esa Puukilainen, Ulrich Kreissig, Markku Leskelä, and Mikko Ritala. Atomic layer deposition of $MgF_2$ thin films using $TaF_5$ as a novel fluorine source. *Chemistry of Materials*, 20(15):5023–5028, August 2008.

[81] M. Mero, J. Liu, W. Rudolph, D. Ristau, and K. Starke. Scaling laws of femtosecond laser pulse induced breakdown in oxide films. *Physical Review B*, 71(11):115109, March 2005.

[82] Erik M. Krous, Dinesh Patel, Ashot Markosyan, Duy N. Nguyen, Luke A. Emmert, Peter Langston, Roger Route, Martin Fejer, Wolfgang Rudolph, Michelle Shinn, and Carmen S. Menoni. Optimization of scandia thin films for high power laser coating applications. In Gregory J. Exarhos, Vitaly E. Gruzdev, Detlev Ristau, M. J. Soileau, and Christopher J. Stolz, editors, *Proceedings of SPIE*, volume 7504, page 750407, Boulder, CO, USA, 2009. SPIE.

[83] M. Putkonen, M. Nieminen, J. Niinisto, L. Niinisto, and T. Sajavaara. Surface-controlled deposition of $Sc_2O_3$ thin films by atomic layer epitaxy using $\beta$-diketonate and organometallic precursors. *Chemistry of Materials*, 13(12):4701–7, December 2001.

[84] Pia Myllymäki, Minna Nieminen, Jaakko Niinistö, Matti Putkonen, Kaupo Kukli, and Lauri Niinistö. High-permittivity $YScO_3$ thin films by atomic layer deposition using two precursor approaches. *Journal of Materials Chemistry*, 16(6):563–569, 2006.

[85] Rong Chen, Hyoungsub Kim, Paul C. McIntyre, David W. Porter, and Stacey F. Bent. Achieving area-selective atomic layer deposition on patterned substrates by selective surface modification. *Applied Physics Letters*, 86(19):191910–191910–3, May 2005.

[86] Nicholas T. Gabriel, Sangho S. Kim, and Joseph J. Talghader. Control of thermal deformation in dielectric mirrors using mechanical design and atomic layer deposition. *Optics Letters*, 34(13):1958–1960, July 2009.

[87] Nicholas T. Gabriel, Sangho S. Kim, and Joseph J. Talghader. Mechanical design of thermally invariant mirrors coated by atomic layer deposition. In *Optical Interference Coatings*, page WD2, Tucson, AZ, June 2010. OSA Technical Digest (Optical Society of America).

[88] Wei Liu and Joseph J. Talghader. Thermally invariant dielectric coatings for micromirrors. *Applied Optics*, 41(16):3285–93, June 2002.

[89] Pochi Yeh. *Optical Waves in Layered Media*. Wiley, New York, 1988.

[90] J. Thurn and R. F. Cook. Stress hysteresis during thermal cycling of plasma-enhanced chemical vapor deposited silicon oxide films. *Journal of Applied Physics*, 91(4):1988–92, February 2002.

[91] Yvete Toivola, Jeremy Thurn, Robert F. Cook, Greg Cibuzar, and Kevin Roberts. Influence of deposition conditions on mechanical properties of low-pressure chemical vapor deposited low-stress silicon nitride films. *Journal of Applied Physics*, 94(10):6915–6922, November 2003.

[92] Characteristics of d 263 thin glass. `http://www.us.schott.com/special_applications/english/products/thin_glass/d263t.html`, January 2010.

[93] K. Tapily, J. E. Jakes, D. S. Stone, P. Shrestha, D. Gu, H. Baumgart, and A. A. Elmustafa. Nanoindentation investigation of $HfO_2$ and $Al_2O_3$ films grown by atomic layer deposition. *Journal of The Electrochemical Society*, 155(7):H545–H551, July 2008.

[94] Nicholas T. Gabriel and Joseph J. Talghader. Optical coatings in microscale channels by atomic layer deposition. *Applied Optics*, 49(9):1242–1248, March 2010.

[95] Kam Law, Quanyuan Shang, William Reid Harshbarger, and Dan Maydan. Deposition of passivation layers for active matrix liquid crystal display (AMLCD) applications, March 2005.

[96] Jeffrey Hicks, Daniel Bergstrom, Mike Hattendorf, Jason Jopling, Jose Maiz, Sangwoo Pae, Chetan Prasad, and Jami Wiedemer. 45nm transistor reliability. *Intel Technology Journal*, 12(02):131–144, June 2008.

[97] A. Husakou and J. Herrmann. Soliton-effect pulse compression in the single-cycle regime in broadband dielectric-coated metallic hollow waveguides. *Optics Express*, 17(20):17636–17644, 2009.

[98] Katsumasa Iwai, Akihito Hongo, Hiroyuki Takaku, Mitsunobu Miyagi, Jun-Ichi Ishiyama, Xiao-Xu Wu, Yi-Wei Shi, and Yuji Matsuura. Fabrication and transmission characteristics of infrared hollow fiber based on silver-clad stainless steel pipes. *Applied Optics*, 48(32):6207–6212, November 2009.

[99] D. Hagedorn, F. Löffler, and R. Meeß. Magnetron sputter process for inner cylinder coatings. *Surface and Coatings Technology*, 203(5-6):632–637, 2008.

[100] Hiroshi Fujiyama. Inner coating of long-narrow tube by plasma sputtering. *Surface and Coatings Technology*, 131(1-3):278–283, September 2000.

[101] Frank Jansen and Steven Krommenhoek. Thin film deposition on inside surfaces by plasma enhanced chemical vapor deposition. *Thin Solid Films*, 252(1):32–37, November 1994.

[102] Jing Li, Chunzhi Gong, Xiubo Tian, Shiqin Yang, Ricky K.Y. Fu, and Paul K. Chu. Structure and gas-barrier properties of amorphous hydrogenated carbon films deposited on inner walls of cylindrical polyethylene terephthalate by plasma-enhanced chemical vapor deposition. *Applied Surface Science*, 255(7):3983–3988, January 2009.

[103] M. Ritala, M. Kemell, M. Lautala, A. Niskanen, M. Leskelä, and S. Lindfors. Rapid coating of through-porous substrates by atomic layer deposition. *Chemical Vapor Deposition*, 12(11):655–658, 2006.

[104] K. Scherer, L. Nouvelot, P. Lacan, and R. Bosmans. Optical and mechanical characterization of evaporated $SiO_2$ layers. long-term evolution. *Applied Optics*, 35(25):5067–5072, 1996.

[105] C. R. Ottermann, K. Bange, W. Wagner, M. Laube, and F. Rauch. Correlation of hydrogen content with properties of oxidic thin films. *Surface and Interface Analysis*, 19:435–438, 1992.

[106] R. M. Costescu, D. G. Cahill, F. H. Fabreguette, Z. A. Sechrist, and S. M. George. Ultra-Low thermal conductivity in $W/Al_2O_3$ nanolaminates. *Science*, 303(5660):989–990, February 2004.

[107] T. Borca-Tasciuc, A. R. Kumar, and G. Chen. Data reduction in $3\omega$ method for thin-film thermal conductivity determination. *Review of Scientific Instruments*, 72(4):2139, 2001.

[108] G. Pernot, M. Stoffel, I. Savic, F. Pezzoli, P. Chen, G. Savelli, A. Jacquot, J. Schumann, U. Denker, I. Mönch, Ch. Deneke, O. G. Schmidt, J. M. Rampnoux, S. Wang, M. Plissonnier, A. Rastelli, S. Dilhaire, and N. Mingo. Precise control of thermal conductivity at the nanoscale through individual phonon-scattering barriers. *Nature Materials*, 9(6):491–495, June 2010.

[109] David G. Cahill. Thermal conductivity measurement from 30 to 750 k: the $3\omega$ method. *Review of Scientific Instruments*, 61(2):802–808, February 1990.

[110] David G. Cahill, M. Katiyar, and J. R. Abelson. Thermal conductivity of a-Si:H thin films. *Physical Review B*, 50(9):6077, 1994.

[111] S.-M. Lee, David G. Cahill, and Thomas H. Allen. Thermal conductivity of sputtered oxide films. *Physical Review B*, 52(1):253, July 1995.

[112] J.-J. Rousseau. *Basic Crystallography*. Wiley, Chichester, England, 1998.

[113] Geoffrey K. H. Pang, K. Z. Baba-Kishi, and A. Patel. Topographic and phase-contrast imaging in atomic force microscopy. *Ultramicroscopy*, 81(2):35–40, March 2000.

[114] David G. Cahill. Erratum: "Thermal conductivity measurement from 30 to 750 k: The $3\omega$ method" [Rev. sci. instrum. 61, 802 (1990)]. *Review of Scientific Instruments*, 73(10):3701, October 2002.

[115] H. R. Shanks, P. D. Maycock, P. H. Sidles, and G. C. Danielson. Thermal conductivity of silicon from 300 to 1400 k. *Physical Review*, 130(5):1743, June 1963.

[116] C. J. Glassbrenner and Glen A. Slack. Thermal conductivity of silicon and germanium from 3K to the melting point. *Physical Review*, 134(4A):A1058, May 1964.

[117] P.D. Maycock. Thermal conductivity of silicon, germanium, III-V compounds and III-V alloys. *Solid-State Electronics*, 10(3):161–168, March 1967.

[118] David G. Cahill and R. O. Pohl. Heat flow and lattice vibrations in glasses. *Solid State Communications*, 70(10):927–930, June 1989.

[119] David G. Cahill, S. K. Watson, and R. O. Pohl. Lower limit to the thermal conductivity of disordered crystals. *Physical Review B*, 46(10):6131, 1992.

[120] E. T. Swartz and R. O. Pohl. Thermal boundary resistance. *Reviews of Modern Physics*, 61(3):605, July 1989.

[121] M. Alvisi, M. Di Giulio, S. G. Marrone, M. R. Perrone, M. L. Protopapa, A. Valentini, and L. Vasanelli. $HfO_2$ films with high laser damage threshold. *Thin Solid Films*, 358(1-2):250–258, January 2000.

[122] David G. Cahill, Wayne K. Ford, Kenneth E. Goodson, Gerald D. Mahan, Arun Majumdar, Humphrey J. Maris, Roberto Merlin, and Simon R. Phillpot. Nanoscale thermal transport. *Journal of Applied Physics*, 93(2):793, 2003.

# Appendix A

# Acronyms and symbols

Table A.1: Acronyms and symbols

| Acronym or symbol | Meaning |
|---|---|
| Å | angstrom; $1\,\text{Å} = 0.1\,\text{nm}$ |
| ALD | atomic layer deposition |
| AMM | acoustic mismatch model |
| CMOS | complementary metal oxide semiconductor |
| CTE | coefficient of thermal expansion |
| CPD | cyclopentadienyl, $-C_5H_5$ |
| CVD | chemical vapor deposition |
| DBR | distributed Bragg reflector |
| DMM | diffuse mismatch model |
| DRAM | dynamic random access memory |
| LIA | lock-in amplifier |
| QCM | quartz crystal microbalance |
| RMS | root mean square, $\sqrt{\frac{1}{N}\sum_{i}^{N} x_i^2}$ |
| SCCM | standard cubic centimeters per minute |
| SEM | scanning electron microscopy |

Continued on next page

**Table A.1 – continued from previous page**

| Acronym or symbol | Meaning |
|---|---|
| SPM | scanning probe microscopy |
| TBS | tris(*tert*-butoxy)silanol, $[(Bu^tO)_3SiOH]$ |
| TCR | temperature coefficient of resistance |
| TDEAH | tetrakis(diethylamido)hafnium, $Hf[N(C_2H_5)_2]_4$ |
| TDMAH | tetrakis(dimethylamido)hafnium, $Hf[N(CH_3)_2]_4$ |
| TEMAH | tetrakis(ethylmethylamido)hafnium, $Hf[N(C_2H_5)(CH_3)]_4$ |
| TEM | transmission electron microscopy |
| Torr | a unit of pressure, 1 Torr $\approx$ 1 mm Hg $\approx$ 133.32 Pa |
| TMA | trimethylaluminum, $Al(CH_3)_3$ |
| TPS | tris(*tert*-pentoxy)silanol |
| VASE | variable-angle spectroscopic ellipsometry |
| XRD | x-ray diffraction |

# Appendix B

# Multilayer thermal deformation and invariance

This appendix is an extension to the discussion of thin film thermal expansion and thermal deformation in Ch. 3, particularly §3.4.1. The model presented in the first section is applied in Ch. 5 to predict the bending of multilayer mirrors in §5.2, and the concept of curvature invariance from the second section of this appendix is used in §5.3 to design mirrors with nearly zero thermal deformation.

## B.1 Multilayer model

In 1963, Vasudevan and Johnson presented a generalized model for the bending of mulitlayer thermostats [18], which was a follow-up to Timoshenko's bimetal 1925 entry [17]. They used their multilayer model in that case to demonstrate the superiority of a trilayer thermostat over a bilayer, but the model has much more general applicability. The primary assumptions in the model are:

- Uniform heating so that the system is at a temperature $T$.
- The system deforms elastically, with each layer described by an elastic modulus $E_i$.
- Linear deformation with bending defined by a single radius of curvature $R$.

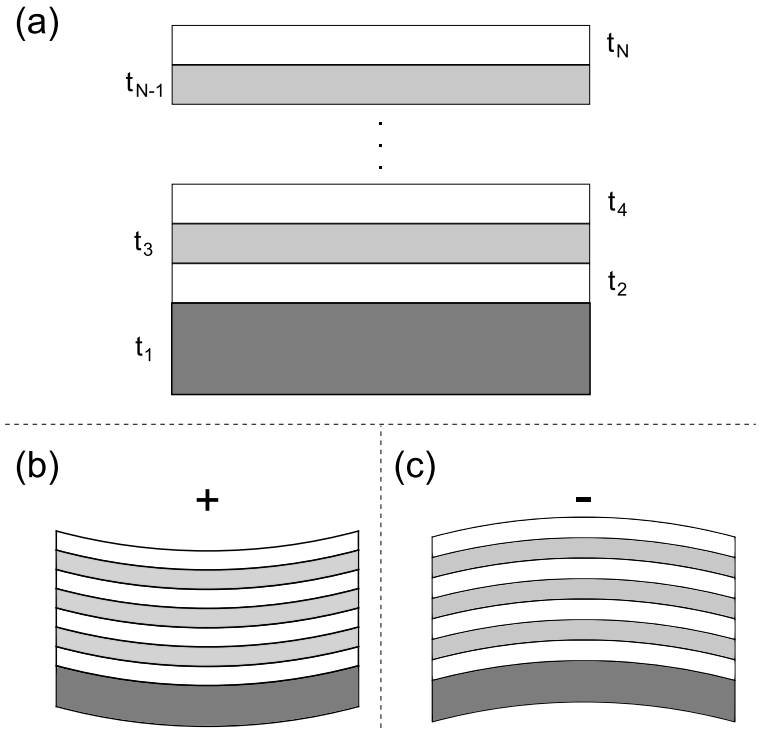


Figure B.1: (a) The multilayer system under consideration, layered from 1 at the bottom to $N$ at the top, along with definitions of (b) positive curvature and (c) negative curvature.

The system of equations for a multilayer with $N$ layers as shown in Fig. B.1 was presented by Vasudevan and Johnson in the form $Ax = b$, where

$$A = \begin{pmatrix} 1 & 1 & 1 & \dots & 1 & 1 & 0 \\ s_2 & -s_1 & 0 & \dots & 0 & 0 & -(t_1+t_2)s_1s_2 \\ 0 & s_3 & -s_2 & \dots & 0 & 0 & -(t_2+t_3)s_2s_3 \\ \vdots & \vdots & \vdots & \ddots & \vdots & \vdots & \vdots \\ 0 & 0 & 0 & \dots & s_N & -s_{N-1} & -(t_{N-1}+t_N)s_{N-1}s_N \\ \ell_1 & \ell_2 & \ell_3 & \dots & \ell_{N-1} & 0 & 2\sum_1^N EI \end{pmatrix}, \tag{B.1}$$

$$b = \begin{pmatrix} 0 \\ (\alpha_2 - \alpha_1)s_1 s_2 \\ (\alpha_3 - \alpha_2)s_2 s_3 \\ \vdots \\ (\alpha_N - \alpha_{N-1})s_N s_{N-1} \\ 0 \end{pmatrix}, \tag{B.2}$$

and

$$x = \frac{1}{2\Delta T}\Delta\left(\frac{1}{R}\right). \tag{B.3}$$

The parameters will be defined momentarily. This linear system can be solved for $x$ by creating another matrix $A'$ that is identical to $A$ except with the $b$ vector substituted for the final column, and then solving[1]

$$x = \frac{\det(A')}{\det(A)} \tag{B.4}$$

The parameters in Eqs. (B.1) through (B.3) are numbered from 1 to $N$ where 1 is the bottom layer and $N$ is the top layer, which results in a curvature sign convention as used in thin film stress calculations, shown in Fig. B.1.[2] Layer thickness, elastic modulus, CTE, and second moment are $t_i$, $E_i$, $\alpha_i$, and $I_i$, where the second moment is $I_i = t_i^3/12$. Two special parameters are defined based on these for reuse; $s_i = t_i E_i$ and

$$\ell_i = \frac{1}{2}\left[t_i + 2\left(\sum_{i+1}^{N-1} t_k\right) + t_N\right].$$

.

Intuitively, the $s_i$ parameter gives the relative strength of the bending exerted by each layer, and the $\ell_i$ parameter is the thickness of all the layers above it in the stack.

To clarify the result of the solution procedure just described, the thermal curvature of the system is given by $1/R$ where $R$ is the radius of curvature in the following

[1] This use of determinants to solve a system of equations is a theorem in linear algebra known as Cramer's rule; e.g. see `http://en.wikipedia.org/wiki/Cramer's_rule`.

[2] In the original 1963 work, Vasudevan and Johnson adopt the opposite order of layers, but also use an opposite curvature sign convention so the end result is equivalent.

expression involving matrix determinants:

$$\Delta\left(\frac{1}{R}\right) = 2\Delta T \frac{\begin{vmatrix} 1 & 1 & 1 & \dots & 1 & 1 & 0 \\ s_2 & -s_1 & 0 & \dots & 0 & 0 & (\alpha_2-\alpha_1)s_1s_2 \\ 0 & s_3 & -s_2 & \dots & 0 & 0 & (\alpha_3-\alpha_2)s_2s_3 \\ \vdots & \vdots & \vdots & \ddots & \vdots & \vdots & \vdots \\ 0 & 0 & 0 & \dots & s_N & -s_{N-1} & (\alpha_N-\alpha_{N-1})s_Ns_{N-1} \\ \ell_1 & \ell_2 & \ell_3 & \dots & \ell_{N-1} & 0 & 0 \end{vmatrix}}{\begin{vmatrix} 1 & 1 & 1 & \dots & 1 & 1 & 0 \\ s_2 & -s_1 & 0 & \dots & 0 & 0 & -(t_1+t_2)s_1s_2 \\ 0 & s_3 & -s_2 & \dots & 0 & 0 & -(t_2+t_3)s_2s_3 \\ \vdots & \vdots & \vdots & \ddots & \vdots & \vdots & \vdots \\ 0 & 0 & 0 & \dots & s_N & -s_{N-1} & -(t_{N-1}+t_N)s_{N-1}s_N \\ \ell_1 & \ell_2 & \ell_3 & \dots & \ell_{N-1} & 0 & 2\sum_1^N EI \end{vmatrix}} \tag{B.5}$$

Equation (B.5) is quite tedious to calculate by hand since each matrix is $N+1$ in size for an $N$ layer system, but calculation in MATLAB is a snap.[3]

This model is one-dimensional for the bending of beams, but as noted by Liu and Talghader in 2002, substitution of biaxial moduli, $M_i = E_i/(1-\nu_i)$, in place of elastic moduli allows the model to be used for the bending of two-dimensional structures [88].

## B.2 Curvature invariance

To gain some design intuition relevant to this dissertation, a special case of Eq. (B.5) is analyzed here. Consider a trilayer, consisting of a substrate and two film layers. For

[3] Research colleague Michael Sutton is acknowledged for creation of a MATLAB function that implements this algorithm.

a trilayer, Eq. (B.5) becomes

$$\Delta\left(\frac{1}{R}\right) = 2\Delta T \frac{\begin{vmatrix} 1 & 1 & 1 & 0 \\ s_2 & -s_1 & 0 & (\alpha_2-\alpha_1)s_1s_2 \\ 0 & s_3 & -s_2 & (\alpha_3-\alpha_2)s_2s_3 \\ \ell_1 & \ell_2 & 0 & 0 \end{vmatrix}}{\begin{vmatrix} 1 & 1 & 1 & 0 \\ s_2 & -s_1 & 0 & -(t_1+t_2)s_1s_2 \\ 0 & s_3 & -s_2 & -(t_2+t_3)s_2s_3 \\ \ell_1 & \ell_2 & 0 & 2(\sum_1^3 E_iI_i) \end{vmatrix}} \tag{B.6}$$

The quotient of determinants can be calculated and simplified into a numerator $\eta$ and and denomiator $D$:

$$\begin{aligned} \eta &= 3M_1t_1M_2t_2\left(\alpha_1-\alpha_2\right)\left(t_1+t_2\right) + \\ &\quad 3M_1t_1M_3t_3\left(\alpha_1-\alpha_3\right)\left(t_1+t_3+2t_2\right) + \\ &\quad 3M_2M_3t_2t_3\left(\alpha_2-\alpha_3\right)\left(t_2+t_3\right) \end{aligned} \tag{B.7}$$

$$\begin{aligned} D &= {M_1}^2{t_1}^4 + {M_2}^2{t_2}^4 + {M_3}^2{t_3}^4 + \\ &\quad 2M_1t_1M_2t_2\left(2{t_1}^2+3t_1t_2+2{t_2}^2\right) + \\ &\quad 2M_1t_1M_3t_3\left(2{t_1}^2+6{t_2}^2+2{t_3}^2+6t_1t_2+3t_1t_3+6t_2t_3\right) + \\ &\quad 2M_2M_3t_2t_3\left(2{t_2}^2+3t_2t_3+2{t_3}^2\right) \end{aligned} \tag{B.8}$$

The $s_i$, $\ell_i$, and $I_i$ have been expanded to physical parameters thickness and/or modulus as described above, and we are using biaxial modulus for the case of a 2D plate rather than a 1D beam.

This coefficient $\eta/D$ has units (length$^{-1}$ temperature$^{-1}$), or curvature/temperature, and if it were zero then the system would not change curvature with temperature. That is a very significant result and will be referred to the curvature invariant or thermally invariant case. The denominator $D$ is always positive and cannot be zero, so we simply require $\eta = 0$ for curvature invariance.

$$\begin{aligned} 0 &= M_2t_2\left(\alpha_1-\alpha_2\right)\left(t_1+t_2\right) + M_3t_3\left(\alpha_1-\alpha_3\right)\left(t_1+t_3+2t_2\right) \\ &\quad + \frac{M_2M_3t_2t_3}{M_1t_1}\left(\alpha_2-\alpha_3\right)\left(t_2+t_3\right) \end{aligned} \tag{B.9}$$

The controlling terms are the three CTE mismatch quantities, $\alpha_1 - \alpha_2$, $\alpha_1 - \alpha_3$, and $\alpha_2 - \alpha_3$. If $\alpha_1 > \alpha_2 > \alpha_3$, then we can pack our bags and go home because it is impossible to achieve curvature invariance; there is no solution to Eq. (B.9) in that case. But if any one of the mismatch terms has opposite sign from the others, then a solution exists for some set of $t_i, M_i, \alpha_i$. So far we have not made any additional assumptions beyond those in the general model described above, and limiting to three layers.

Equation (B.9) is sufficiently complicated that numerical solution is still advisable, e.g. to find the third layer thickness with all other parameters known. To get more intuition, we now assume the substrate is much thicker than either of the two films, i.e. $t_1 \gg t_2, t_3$. Then we can neglect all second order or higher terms of $t_2$ and $t_3$ to arrive at a much simpler condition for curvature invariance.

$$0 = M_2 (\alpha_1 - \alpha_2) t_2 + M_3 (\alpha_1 - \alpha_3) t_3 \tag{B.10}$$

Now we can see all that matters are the CTE of each film relative to the substrate, where one film must have a larger CTE than the substrate and one film must have smaller CTE than the substrate for there to be a solution to Eq. (B.10). Interaction between the two films has become irrelevant. Moreover, the modulus and CTE mismatch terms are thermal stress values for each film-substrate combination, which have units of pressure/temperature and are commonly measured in thin film processing using the Stoney approximation as described in §3.4.1. We can rearrange the invariance condition to get a simple thickness ratio for achieving thermal invariance based on the thermal stress of each film relative to the thick substrate, which is also written in the language of thin film thermal stress.

$$\frac{t_2}{t_3} = \frac{M_3(\alpha_3 - \alpha_1)}{M_2(\alpha_1 - \alpha_2)} \tag{B.11}$$

$$= \frac{\sigma_{T,3}}{\sigma_{T,2}} \tag{B.12}$$

The significant result is that without measuring the biaxial modulus of either film, the thermally invariant thickness ratio can be determined by simply measuring the thermal stress of single films on a substrate. As long as the assumption holds where the substrate

thickness is much larger than the total film thickness, this simplification applies to a multilayer with any number of $t_2/t_3$ film pairs.

# Appendix C

# Multilayer optical modeling

This appendix describes the multilayer optical simulation used for work in Chs. 5 and 6. The model as described by Pochi Yeh [89] was implemented in MATLAB to calculate reflected and transmitted intensity for multilayer films having specified thickness and refractive indices, including dispersion; the input light is defined by its wavelength(s), angle(s) of incidence, and polarization.[1]

## C.1 Multilayer model for plane waves

We apply the matrix method presented by Pochi Yeh [89] to calculate the response of a set of $N$ isotropic layers to incident plane waves. The layers are described by a complex refractive index $\hat{n}_i(\lambda) = n(\lambda) - jk(\lambda)$, where $j = \sqrt{-1}$, although the work presented in this dissertation involves films with zero absorption ($k = 0$) in the wavelength range of interest. The layer structure is shown in Fig. C.1. Note that the layers are numbered in the opposite direction as for the multilayer model presented in Appendix B. That model was set up to match the curvature sign convention used by the film stress community, whereas this one matches the direction of light propagation.

The angle of propagation in each layer changes due to refraction and is given by

$$\cos\theta_i = \sqrt{1 - \left(\frac{n_0 \sin\theta_0}{\hat{n}_i(\lambda)}\right)^2}. \tag{C.1}$$

[1] Joseph Talghader, Michael Sutton, and Anand Gawarikar are acknowledged for their contributions to C and MATLAB implementations of Pochi Yeh's matrix method that were adapted for use in this dissertation.

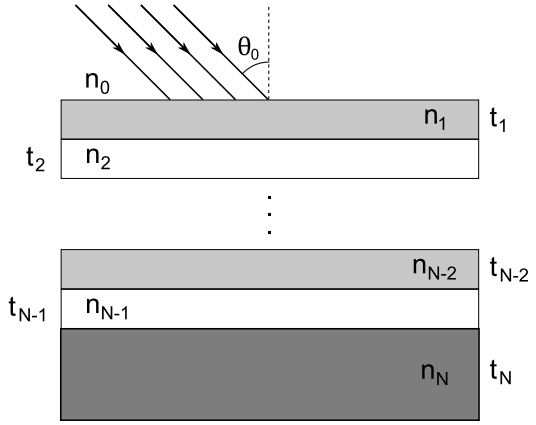


Figure C.1: The optical multilayer used in the model. A plane wave is incident at angle $\theta_0$ from the surface normal, moving from a medium with refractive index $\hat{n}_0$ onto the top layer, which is layer 1.

The dynamical matrices representing behavior across each interface for $s$ and $p$ polarization (see Fig. C.2) are $D_{i,s}$, and $D_{i,p}$.

$$D_{i,s} = \begin{pmatrix} 1 & 1 \\ \hat{n}_i(\lambda)\cos\theta_i & -\hat{n}_i(\lambda)\cos\theta_i \end{pmatrix} \tag{C.2}$$

$$D_{i,p} = \begin{pmatrix} \cos\theta_i & \cos\theta_i \\ \hat{n}_i(\lambda) & -\hat{n}_i(\lambda) \end{pmatrix} \tag{C.3}$$

Propagation through each layer is described by a plane-wave propagation matrix $P_i$,

$$P_i = \begin{pmatrix} \exp(j\psi_i) & 0 \\ 0 & \exp(-j\psi_i) \end{pmatrix}, \tag{C.4}$$

where $\psi_i$ is an optical path length parameter

$$\psi_i = \frac{2\pi\hat{n}_i(\lambda)t_i}{\lambda}\cos\theta_i, \tag{C.5}$$

and the complex exponentials are plane waves propagating in each direction (forward and backward).

These dynamical and propagation matrices are successively multiplied to calculate a $2 \times 2$ matrix that relates the amplitude and phase of plane waves at the initial ($A_0^{\pm}$)

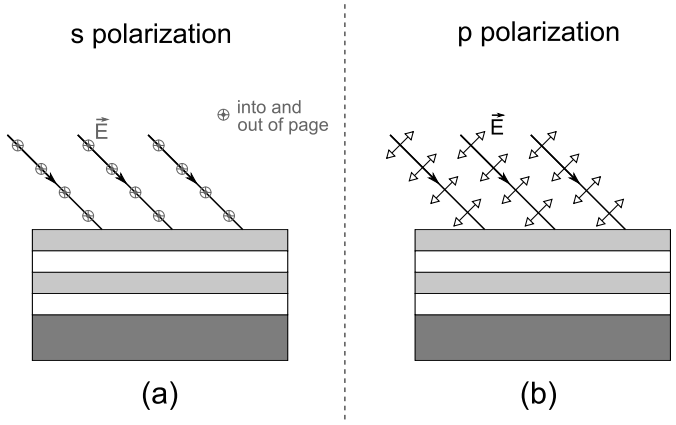


Figure C.2: A plane wave of light is referred to as (a) $s$ polarized when its electric field is perpendicular to the plane of incidence ($s$ is short for *senkrecht* which means perpendicular in German), and (b) $p$ polarized when its electric field is parallel to the plane of incidence.

and final ($A_N^{\pm}$) surfaces, both transmitted ($^+$) and reflected ($^-$).

$$\begin{aligned} M(\lambda) &= D_0^{-1}\left[\prod_{i=1}^{N-1} D_i P_i D_i^{-1}\right] D_N \\ &= \begin{pmatrix} m_{11}(\lambda) & m_{12}(\lambda) \\ m_{21}(\lambda) & m_{22}(\lambda) \end{pmatrix} \end{aligned} \tag{C.6}$$

$$\begin{pmatrix} A_0^+ \\ A_0^- \end{pmatrix} = \begin{pmatrix} m_{11}(\lambda) & m_{12}(\lambda) \\ m_{21}(\lambda) & m_{22}(\lambda) \end{pmatrix} \begin{pmatrix} A_N^+ \\ A_N^- \end{pmatrix} \tag{C.7}$$

Referring to the situation presented in Fig. C.3, for light incident on the initial surface with amplitude $A_0^+$, it is either reflected into $A_0^-$ or transmitted into $A_N^+$; the amplitude $A_N^-$ must be zero for this case. Then we can write the reflected intensity based on the ratio of reflected to incident light.

$$R(\lambda) = \left|\frac{A_0^-}{A_0^+}\right|^2_{A_N^-=0} \tag{C.8}$$

Solving Eq. (C.7) in this case yields

$$\begin{aligned} A_0^+ &= m_{11}(\lambda)A_N^+ + 0 \\ A_0^- &= m_{21}(\lambda)A_N^+ + 0, \end{aligned}$$

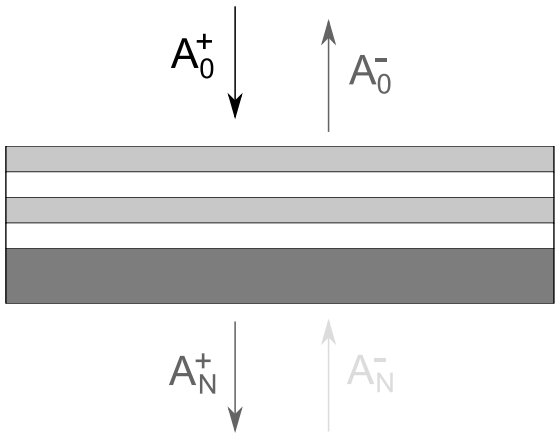


Figure C.3: The case applied to derive the reflected intensity given in Eq. (C.9), where light is incident from the top with amplitude $A_0^+$ and a portion is reflected with amplitude $A_0^-$ and transmitted with amplitude $A_N^+$. In this case $A_N^-$ must be zero.

which gives the reflected intensity versus wavelength

$$R(\lambda) = \left| \frac{m_{21}(\lambda)}{m_{11}(\lambda)} \right|^2 . \tag{C.9}$$

# Appendix D

# Differential 3$\omega$ details

This appendix contains a derivation and uncertainty analysis of the measurement and analysis of thermal conductivity data in Ch. 7.

## D.1 Differential 3$\omega$ derivation

In §7.4.3 the differential 3$\omega$ technique was described and Eq. (7.8) was presented for calculating thermal conductivity from a set of 3rd-harmonic measurements. That equation is repeated here:

$$k_f = \frac{t_f}{WL} \frac{1}{(\Delta T/P)_f - (\Delta T/P)_0} \tag{D.1}$$

The derivation is presented more fully here to give a better sense of the relationship between the film and reference samples. The derivation will proceed allowing the two samples to have different power input and different heater line width and length, but as we will see these quantities must be identical among the two samples to arrive at Eq. (D.1).

Each film layer has a thermal conductance $G_i$ based on its thermal conductivity $k_i$, thickness $t_i$, and the area of the heater line, described by its width $W$ and length $L$.

$$G_i = \frac{k_i W L}{t_i} \tag{D.2}$$

The associated temperature drop $\Theta_i$ for a given input power $P$ is

$$\Theta_i = \frac{P}{G_i} \tag{D.3}$$

Thus,

$$\Theta_i = \frac{Pt_i}{k_i W L} \tag{D.4}$$

In this measurement we have two samples, the film/reference and the reference sample. The reference sample has a single film layer $t_1$, a total thermal conductivity $G_R = G_1$, and an associated temperature drop of

$$\Theta_R = \frac{P_R t_1}{k_1 W_R L_R}. \tag{D.5}$$

The film/reference sample has two layers in series, so the conductance adds inversely:

$$\frac{1}{G_f} = \frac{1}{G_1} + \frac{1}{G_2} = \frac{t_1}{W_f L_f k_1} + \frac{t_2}{W_f L_f k_2}. \tag{D.6}$$

This temperature drop across this layer structure is

$$\Theta_f = P_f \left( \frac{t_1}{W_f L_f k_1} + \frac{t_2}{W_f L_f k_2} \right). \tag{D.7}$$

We are interested in the differential result, or $\Theta_f$ - $\Theta_R$.

$$\Theta_f - \Theta_R = \frac{P_f}{W_f L_f} \left( \frac{t_1}{k_1} + \frac{t_2}{k_2} \right) - \frac{P_R t_1}{W_R L_R k_1} \tag{D.8}$$

We are after the film thermal conductivity, $k_2$, and would rather not care to know the exact values of $k_1$ or $t_1$ of the reference film shared by both samples. We thus require three conditions:

1. the heater wire has identical geometry on both samples, i.e. $W_f = W_R = W$ and $L_f = L_R = L$,

2. the same power is input to both samples during the measurement, i.e. $P_f = P_R = P$, and

3. the two samples have identical reference films, i.e. $t_1$ and $k_1$ are indeed the same across samples as implied in the above derivation.

If these three conditions are true, then the differential result simplifies to

$$\Theta_f - \Theta_R = \frac{P t_2}{W L k_2}. \tag{D.9}$$

We are trying to find the thermal conductivity of the unknown film, $k_2$, so we rearrange:

$$k_2 = \frac{Pt_2}{WL}\frac{1}{\Theta_f - \Theta_R} \tag{D.10}$$

This is a restatement of Eq. (7.8) or Eq. (D.1) and embodies the entire differential $3\omega$ measurement. The parameters $W$ and $L$ are precisely defined by photolithography, $t_2$ is measured independently, the input power is measured, and the $3\omega$ measurement yields experimental values of $\Theta_f$ and $\Theta_R$ as shown in Fig. 7.2 and described by Eq. (7.1), $\Theta = 2v_{3\omega}/(\alpha v_{1\omega})$.

## D.2 Uncertainty in differential $3\omega$

The many measured parameters that go into the differential $3\omega$ technique make it prudent a look at uncertainty in thermal conductivity resulting from each parameter.

We start from this fully-expanded and fairly general expression of the differential $3\omega$ method:

$$k_f = \frac{t_f}{2L}\left[\left(\frac{v_{3\omega}WR}{\alpha v_{1\omega}^3}\right) - \left(\frac{v_{3\omega}WR}{\alpha v_{1\omega}^3}\right)_0\right]^{-1} \tag{D.11}$$

This is basically Eq. (7.8) or Eq. (D.1), but with individual $v_{1\omega}^2/R$ terms inserted in place of input power $P$ and $2v_{3\omega}/(\alpha v_{1\omega})$ in for the $\Delta T$ terms. Here we have only assumed that $L$ is shared among the two samples; parameters like line width $W$ or temperature coefficient of resistance $\alpha$ are allowed to vary individually. Also, the subscript 0 refers to the reference sample and no subscript refers to the film/reference sample or both samples in the case of $L$. We would like to know how errors in $t_f$, $L$, $W$, $\alpha$, $v_{3\omega}$, $v_{1\omega}$, or $R$ propagate to the $k_f$ result.

The approach is to calculate the fractional partial derivative of $k_f$ with respect to each of those parameters. The easy ones are $t_f$ and $L$, which can basically be done by inspection:

$$\frac{\partial k_f}{\partial t_f}\frac{t_f}{k_f} = 1 \tag{D.12}$$

$$\frac{\partial k_f}{\partial L}\frac{L}{k_f} = -1 \tag{D.13}$$

In other words, a 1% error in $t_f$ or $L$ measurement would contribute a 1% or -1% error in $k_f$, respectively.

For subsequent parameters, to avoid silly mistakes the derivatives were performed symbolically using SymPy, an open-source module for the Python scripting language.[1]

There is a term common to all of the film/reference fractional derivatives, which will be called $FD$:

$$FD = \left[1 - \frac{R_0}{R}\frac{v_{3\omega 0}}{v_{3\omega}}\frac{W_0}{W}\frac{\alpha}{\alpha_0}\left(\frac{v_{1\omega}}{v_{1\omega 0}}\right)^3\right]^{-1}. \tag{D.14}$$

Similarly for the fractional derivatives with respect to one of the reference sample parameters, there is a common $FD_0$ term:

$$FD_0 = \left[\frac{R}{R_0}\frac{v_{3\omega}}{v_{3\omega 0}}\frac{W}{W_0}\frac{\alpha_0}{\alpha}\left(\frac{v_{1\omega 0}}{v_{1\omega}}\right)^3 - 1\right]^{-1}. \tag{D.15}$$

Each fractional derivative, $(\partial k_f/\partial X)(X/k_f)$, is simply proportional to either $FD$ or $FD_0$:

- $W$, $R$, or $v_{3\omega}$: $-FD$
- $W_0$, $R_0$, or $v_{3\omega 0}$: $FD_0$
- $\alpha$: $FD$
- $\alpha_0$: $-FD_0$
- $v_{1\omega}$: $3FD$
- $v_{1\omega 0}$: $-3FD_0$

So basically the uncertainty rests on the shoulders of $FD$ and $FD_0$. It is important to note that $v_{1\omega}$ and $v_{1\omega 0}$ have three times the impact of the others, which comes from their dual role in power ($P = v_{1\omega}^2/R$), and in measured temperature drop ($\Delta T = 2v_{3\omega}/\alpha v_{1\omega}$). Also noteworthy is that both $FD$ and $FD_0$ have a singularity if all parameters are equal to their reference sample counterparts, i.e. if $R = R_0$, $W = W_0$, $\alpha = \alpha_0$, $v_{1\omega} = v_{1\omega 0}$, and $v_{3\omega} = v_{3\omega 0}$. This is quite sensible and in particular is caused by the implied equality of $v_{3\omega}$ and $v_{3\omega 0}$; it means that it becomes increasingly difficult to accurately measure the film thermal conductivity if the two samples employed produce identical or nearly-identical 3rd-harmonic responses. The differential $3\omega$ technique is entirely based on the

[1] See `http://code.google.com/p/sympy/` and `http://python.org/`.

premise of a significant difference between measured $v_{3\omega}$ and $v_{3\omega 0}$ so that they can be subtracted to yield a non-zero result. Implied is that the film of interest must be thick enough or have a thermal conductivity small enough to produce a significant $\Delta v_{3\omega}$.

The numerical value of *FD* and $FD_0$ is crucial to understanding the actual absolute uncertainty, and central to them is the ratio of $v_{3\omega}$ and $v_{3\omega 0}$. The other parameter ratios will essentially evaluate to 1 as an aggregate due to the other requirements laid out in §D.1 of this Appendix, namely that $P = P_0$, $L = L_0$, and $W = W_0$ for proper cancellation of reference terms in the derivation of Eq. (D.1). Thus we can simplify the common fractional derivative terms to

$$FD \approx \left[1 - \frac{v_{3\omega 0}}{v_{3\omega}}\right]^{-1} \tag{D.16}$$

$$FD_0 \approx \left[\frac{v_{3\omega}}{v_{3\omega 0}} - 1\right]^{-1}. \tag{D.17}$$

The $v_{3\omega}$ and $v_{3\omega 0}$ data are presented in Fig. D.1, where it can be seen that the ratio $v_{3\omega}/v_{3\omega 0}$ varied between about 1.3 and 1.75, moving from relatively high-conductivity alumina through the lower-conductivity nanolaminate samples. These yield *FD* values ranging from 4.33 to 2.33 and $FD_0$ values ranging from 3.33 to 1.33.

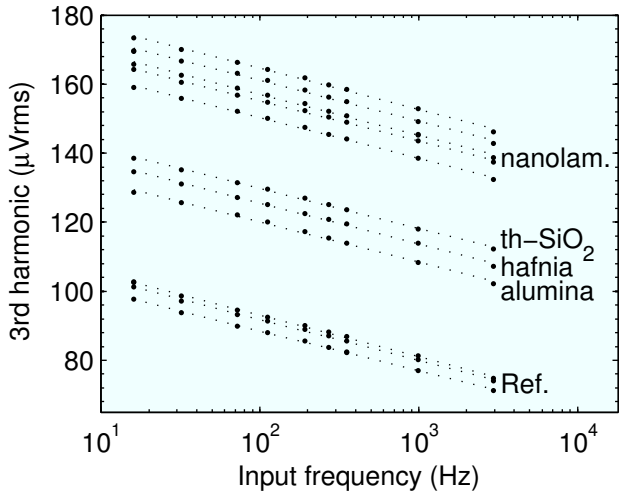


Figure D.1: Raw 3rd-harmonic data versus frequency for all of the thermal conductivity measurements presented in Ch. 7, similar to $\Delta T$ versus frequency plotted in Fig. 7.2 but more applicable to this evaluation of uncertainty.

Qualitatively we can already see that the alumina measurement has the highest

uncertainty in thermal conductivity, which intuitively makes sense because films with larger thermal conductivity will appear thermally "thinner", and thinner films are more difficult to measure accurately. But we can now quantitatively estimate overall uncertainty for each particular thermal conductivity value by estimating the individual uncertainty in each parameter and then summing them with appropriate weighting as described above. The values will be given as ± a percentage so that the resulting total uncertainty will also be ± a percentage around the measured value.

The EG&G 7265 digital lock-in amplifier (LIA) employed to measure $v_{1\omega}$ and $v_{3\omega}$ has a 0.2% typical accuracy in the input-stage gain, the only analog portion in the LIA signal processing chain. Upstream from these channels were the AD620 instrumentation amplifiers, as depicted in Fig. 7.1, which have a maximum gain error of 0.1% in the unity-gain configuration. Since the signal from two AD620s was subtracted for the $v_{3\omega}$ measurements, the total error for those is 0.2%. Thus we assume 0.3% overall accuracy for the fundamental signal and 0.4% for the 3rd harmonic.

Resistance was measured with a Keithley 2420 SourceMeter in 4-wire mode while manually sourcing current. Specified current source accuracy is 0.07% and voltage measurement accuracy is 0.1% for current near 10 mA and voltage near 400 mV (40 Ω), or under 0.2% overall.

Line width near 8.0 $\mu$m was measured with an optical microscope with estimated uncertainty of about 0.2 $\mu$m or 2.5%. Line length uncertainty is about 0.05%; it is 1.0 mm with photolithographically defined accuracy of about 0.5 $\mu$m.

Film thickness was measured and modeled via spectroscopic ellipsometry. While the measured $\Psi$ and $\Delta$ data itself is highly accurate, uncertainty in modeling parameters, particularly surface roughness, makes likely accuracy closer to about 2 nm or 2%.

The room temperature coefficient of resistance (TCR) measurement system was somewhat complex. The device resistance was measured with a Keithley 2410 SourceMeter, with accuracy similar to the 0.2% for the aforementioned 2420. Temperature was measured using a 100 kΩ thermistor[2] biased by a home-built Howland 10 $\mu$A current source. The current source itself was biased by a Keithley 6517A and its output was verified to be within 0.1% of 10 $\mu$A by the same instrument. The thermistor itself dominates the uncertainty of this measurement, having a specified $\Delta R/R$ uncertainty of

[2] Vishay NTCLE203E3104FB0

about ±1.2% over the 40 K temperature range of the measurement. The 2410, current source, and thermistor combine to yield 1.5% overall uncertainty of the TCR measurement.

Adding all of these together, accounting for the factor of 3 scaling of the $v_{1\omega}$ uncertainty, and not counting the film thickness uncertainty for the reference samples, we get 7.55% base uncertainty for film samples and 5.55% base uncertainty for reference samples, the two sets that make up one measured thermal conductivity value in this differential technique. The base uncertainties are significantly scaled up by the *FD* and $FD_0$ values that depend on the ratio of $v_{3\omega}$ to $v_{3\omega 0}$ as defined above.

The worst case is the alumina film, measured to be 2.59 W/(m K) from a $v_{3\omega}/v_{3\omega 0}$ ratio of only 1.3. The ±7.55% and ±5.55% base uncertainties get scaled by 4.33 and 3.33, respectively, for the film sample and reference sample measurements due to *FD* and $FD_0$, yielding a combined ±51% or ±1.3 W/(m K) uncertainty in alumina. This is considerably high, but it must be emphasized that this is the worst-case of all the measured films. The best-case is a $v_{3\omega}$ ratio of about 1.75 in most of the nanolaminate films, yielding ±25% uncertainty or ±0.3 W/(m K) around the 1.1 W/(m K) median values.

It should also be noted that these are absolute uncertainties not relative ones. The same instruments and techniques were used to prepare and measure all the film and reference samples, meaning that the pair of uncertainties (film - reference) likely do not strictly sum, rather there would be some "common-mode" error that subtracts out during the differential measurement. For the same reason the measurements should be much less uncertain relative to one another, important for the hafnia and nanolaminate comparison in Ch. 7.